ABSTRACT

NANOSTRUCTURED COMPOSITE MATERIALS BASED ON CARBON NANOTUBES AND 3-D PHOTONIC CRYSTALS

by
Jing Chen

Carbon nanotubes (CNT) and in particular, single-wall carbon nanotubes (SWCNT) have been extensively studied, in large part, due to their unique one-dimensional crystalline structures and related electronic and optical properties. Various polymeric composite materials, which were based on carbon nanotubes, have been also developed in an attempt to combine the properties of polymer and CNT in a single film. Such composites were mainly formed by mixing carbon nanotubes within the polymer without special emphasis on the structure and thereby, the nanoscopic properties of the resultant material.

Photonic crystals belong to a class of man-made structures aimed at manipulating the propagation of electromagnetic waves at sub-wavelength dimensions in the visible range. The objective of this research work was to fabricate optical nano-composites from the bottom up: by incorporating carbon nanotubes within nano-structured templates we attempted to achieve novel composites with unique optical properties.

Three-dimensional photonic crystals were made by self-assembly using monodisperse suspension of silicon dioxide colloids. Upon sedimentation, this highly ordered crystal, also known as opal, serves as a template for polymeric and polymer/CNT composites. For example, by infiltrating of the templates voids with a desired polymeric solution followed by etching of the silica template away, a three-dimensional inverse polymeric structure is obtained.

Single-wall carbon nanotubes (SWCNT) have been directly grown into the template voids (in the range of 20 – 70 nm) by catalytic Chemical Vapor Deposition (CVD) technique with carbon monoxide as the carbon feedstock. The resultant SWCNTs were mostly semiconductive (p-doped). Control over the growth of SWCNT has been obtained by changing the catalyst concentration and the template's void-size.

Various techniques were used to characterize the SWCNT and its composites: Scanning Electron Microscope (SEM) has been used to identify the morphology of structures; interactions between polymer and nanotubes have been characterized by Raman spectroscopy; optical properties were studied by linear and nonlinear optical transmission and optical activity measurements; electrical properties were studied using thermoelectric and photoconductivity measurements. These data suggest that self-organized nano-scale templates are a promising route for realizing novel optical composite materials.

NANOSTRUCTURED COMPOSITE MATERIALS BASED ON CARBON NANOTUBES AND 3-D PHOTONIC CRYSTALS

by
Jing Chen

A Dissertation
Submitted to the Faculty of
New Jersey Institute of Technology
in Partial Fulfillment of the Requirements for the Degree of
Doctor of Philosophy in Materials Science and Engineering

Interdisciplinary Program in Materials Science and Engineering

May 2005

APPROVAL PAGE

NANOSTRUCTURED COMPOSITE MATERIALS BASED ON CARBON NANOTUBES AND 3-D PHOTONIC CRYSTALS

Jing Chen

Dr. Haim Grebel, Dissertation Advisor Date
Professor of Electrical and Computer Engineering, NJIT

Dr. Zafar Iqbal, Committee Member Date
Professor of Chemistry, NJIT

Dr. Marek Sosnowski, Committee Member Date
Professor of Electrical and Computer Engineering, NJIT

Dr. John Federici, Committee Member Date
Professor of Physics, NJIT

Dr. Roger Dorsinville, Committee Member Date
Professor and Department Chair of Electrical Engineering,
City College of the City University of New York

BIOGRAPHICAL SKETCH

Author: Jing Chen

Degree: Doctor of Philosophy

Date: May 2005

Undergraduate and Graduate Education:

- Doctor of Philosophy in Materials Science and Engineering,
  New Jersey Institute of Technology, Newark, NJ, 2005

- Master of Science in Polymer Chemistry and Physics,
  Institute of Chemistry, Chinese Academy of Sciences, Beijing, P. R. China, 1997

- Bachelor of Engineering in Polymer Engineering,
  Tianjin University, Tianjin, P. R. China, 1994

Major: Materials Science and Engineering

Presentations and Publications:

J. Chen, S. W. Lee, H. Grebel,
"Controlled growth of single-wall carbon nanotubes within three-dimensional silica templates", submitted to Carbon, 2005.

H. Han, J. Chen, Y. Diamant, M. Etienne, R. Dorsinville, H. Grebel,
"Nonlinear properties of nano-structures with single-wall carbon nanotubes and conductive polymers", Appl. Phys. Lett. 86(5), 053113, 2005.

Y. Diamant, J. Chen, H. Han, B. Kamenev, L. Tsybeskov, H. Grebel,
"Electrochemical polymerization and characterizations of polycarbazole on Single Wall Carbon Nanotubes", accepted by Synthetic Metals, 2005.

H. Han, J. Chen, Y. Diamand, H. Grebel, M. Etienne, R. Dorsinville,
"Novel nonlinear three-dimensional distributed nano-structures with single-wall carbon nanotubes", 2004 NLO, Waikoloa, Hawaii, Aug 2-6, 2004.

J. Chen, H. Han, Y. Diamand, H. Grebel, M. Etienne, R. Dorsinville,
"Optical and optoelectronic properties of inverse photonic crystals composed of single-wall carbon nanotubes and conductive polymers", 2004 CLEO/IQEC, San Francisco, CA, May 16-21, 2004.

H. Grebel, J. Chen, H. Han, and Y. Diamant,
"Linear and nonlinear optical properties of single-wall carbon nanotubes", Proc. SPIE Int. Soc. Opt. Eng., 5352, 126-133, 2004.

To My Beloved Husband, Cong Zhang,
and My Dearest Parents, Liru and Changzhi Chen
For Their Encouragement and Unquestioning Love.

ACKNOWLEDGMENT

I would like to express my deepest appreciation to my advisor, Dr. Haim Grebel, who provide me with the opportunity to conduct research in Electronic Imaging Center and introduce me to the fascinating world of nanotechnology. He not only served as my research supervisor, providing valuable and countless resources, insight, and intuition, but also constantly gave me support, encouragement, and reassurance.

Special thanks are given to Dr. Roger Dorsinville, Dr. John Federici, Dr. Zafar Iqbal, and Dr. Marek Sosnowski for actively participating in my committee and provided me with constructive suggestions on my dissertation.

I would also like to extend my sincere gratitude to Dr. Xueyan Zhang, Microscopy Specialist working in Material Characterization Laboratory, for her training and assistance in AFM and SEM/EDX characterization.

Many of my fellow graduate students and research staff in the Electronic Imaging Center are deserving of recognition for their support. Here I would like to express my sincere appreciation to Dr. Yan Zhang, Dr. Aidong Lan, Dr. Yishay Diamant, Dr. David Katz, Dr. G. Leszek, and graduate students, Hui Han, Yubin Wang and Seon Woo Lee, for their kindly assistance and sincere friendship over the years.

TABLE OF CONTENTS

Chapter **Page**

1 INTRODUCTION 1

1.1 Photonic Crystals 1

1.1.1 The Concept of Photonic Crystals 1

1.1.2 Photonic Band Structure 1

1.1.3 Fabrication of Photonic Crystals 3

1.1.4 Application of Photonic Crystals 9

1.1.5 Polymer Inverse Opal 12

1.2 Carbon Nanotubes 15

1.2.1 Structure of Single-wall Carbon Nanotubes 15

1.2.2 Fabrication of Single-wall Carbon Nanotubes 19

1.2.3 Electronic Properties of Single-wall Carbon Nanotubes 24

1.2.4 Application of Single-wall Carbon Nanotubes 29

1.3 Carbon Nanotube–Polymer Composite Materials 33

1.3.1 Mechanical Reinforcement 33

1.3.2 Electrical Property Enhancement 35

1.3.3 Surface Modification of Carbon Nanotubes 37

1.3.4 Chemical Doping of Carbon Nanotubes 42

2 EXPERIMENTAL METHODOLOGY 45

2.1 Synthetic Silica Opal 46

2.1.1 Synthesis of Monodisperse Silica Colloid 46

2.1.2 Measuring the Size of Colloidal Silica Particles 47

TABLE OF CONTENTS
(Continued)

Chapter **Page**

2.1.3 Fabrication of Synthetic Silica Opal 49

2.2 Growth of Single-wall Carbon Nanotube by CVD 51

2.3 Fabrication of Nanostructured Polymer–SWCNT Composites 52

2.3.1 Poly(methyl methacrylate) 54

2.3.2 Poly(N-vinylcarbazole) Compound 54

2.4 Characterization of Nanostructured Composites 57

2.4.1 Scanning Electron Microscopy/Energy Dispersive Spectroscopy 57

2.4.2 UV-Vis-NIR Optical Spectroscopy 60

2.4.3 Optical Activity Measurement 64

2.4.4 Raman Scattering Spectroscopy 65

2.4.5 Current – Voltage Characterization 70

2.4.6 Thermoelectricity – Seebeck Effects 71

2.4.7 Nonlinear Optical Characterization 73

3 RESULTS AND DISCUSSION 76

3.1 Synthetic Silica Opal 76

3.1.1 Synthesis of Monodisperse Silica Spheres 76

3.1.2 Structure of Self-assembled Silica Opal 79

3.1.3 Optical Characterization of Silica Opal 81

3.2 SWCNT Embedded in Synthetic Opal Template 85

3.2.1 Controlled Growth of SWCNT by CVD 85

3.2.2 Optical Characterization 97

TABLE OF CONTENTS
(Continued)

Chapter **Page**

3.2.3 Raman Spectrum 99

3.2.4 Optical Activity 106

3.2.5 Electrical and Photoelectronic Properties 108

3.3 Polymeric Inverse Opal 110

3.3.1 Structure of PMMA Inverse Opal 110

3.3.2 Optical Spectrum of PMMA Inverse Opal 113

3.3.3 UV Absorption of PVK Inverse Opal 114

3.4 Polymer – SWCNT Composites Inverse Opal 116

3.4.1 Morphology of Polymer – SWCNT Composite 116

3.4.2 Optical Characterization 117

3.4.3 Raman Spectrum 118

3.4.4 Electrical and Photoelectronic Properties 122

3.4.5 Nonlinear Optical Transmission 125

3.5 Distributed p-n Junction with 3-D Ordered Structure 127

3.5.1 Polymer Functionalized n-type SWCNT 128

3.5.2 Raman Spectrum of PEI Coated SWCNT 131

3.5.3 Three-dimensional Distributed p-n Interface 133

4 CONCLUSIONS 138

REFERENCES 140

LIST OF TABLES

Table **Page**

1.1 Classification of Single-wall Carbon Nanotubes 18

2.1 Characteristic X-ray Emission Spectrum Line for Different Elements 60

3.1 Diameter of Colloidal Silica Spheres as a Function of Concentration of Different Reactants 78

3.2 Quantitative Result of EDX Elemental Analysis 87

3.3 Productivity of Cobalt Nitrate Distributed in Silica Template 91

3.4 Quantity Result of EDX Elemental Analysis 96

3.5 Possible Chirality and Diameter of SWCNT 100

LIST OF FIGURES

Figure		Page
1.1	Schematic diagrams of the first Brillouin Zone	3
1.2	Yablonovite-like photonic crystal	4
1.3	Woodpile photonic crystal by lithography	5
1.4	Polymeric photonic crystal by holography	6
1.5	Synthetic silica opal	8
1.6	Examples of optical waveguide design based on 2-D photonic crystal	10
1.7	Schematic drawing of the sensing operation of a creatinine deiminase – doped Ppy inverse opal exposed to a buffered creatinine solution	14
1.8	Schematic structures of single-wall carbon nanotubes as an unrolled honeycomb lattice	16
1.9	Schematic structure of single-wall carbon nanotubes from side view	18
1.10	Schematic diagram showing the carbon nanotubes (*n*, *m*) that are metallic and semiconducting	25
1.11	Atomically resolved STM images of individual SWCNT	26
1.12	$(dI/dV)/(I/V)$ versus V for single-wall carbon nanotubes	27
1.13	Calculated energy separations $E_{ii}(d_t)$ for all (*n*, *m*) values versus nanotube diameters	28
1.14	Electrical response of a semiconducting SWCNT to gas molecules of NH_3 and NO_2	31
1.15	Molecular conformation of conjugated polymers	36
1.16	Schematic polymer wrapping geometries	39
1.17	Scheme for non-covalent functionalization of the sidewalls of carbon nanotubes for protein immobilization	40
1.18	Single wall carbon nanotube device with p-n-p junction	44
2.1	Diagram of experimental workflow	45

LIST OF FIGURES
(Continued)

Figure **Page**

2.2 Schematic diagram of the N4 Plus built on Photon Correlation Spectroscopy technique ... 48

2.3 Schematic experiment setup for synthetic silica opal deposition and an enlarged view of the meniscus area ... 50

2.4 Schematic setup of atmosphere chemical vapor deposition ... 51

2.5 Schematic setup of a chemical reaction cell for polymer infiltration ... 53

2.6 Molecular structures of chemicals involved in PVK-SWCNT composite ... 57

2.7 Schematic diagram of interaction between incident electron beam and samples in Scanning Electron Microscopy ... 58

2.8 Schematic view of the fcc close packed lattice ... 61

2.9 Schematic setup of optical spectroscopy measurement ... 63

2.10 Schematic setup of optical activity measurement ... 65

2.11 Schematic principle of Raman scattering ... 66

2.12 Schematic Raman spectrum ... 68

2.13 Schematic setup for current – voltage characterization ... 71

2.14 Schematic mechanism of thermoelectricity ... 72

2.15 Schematic setup of nonlinear optical transmission measurement ... 74

3.1 SEM image of silica colloidal particles produced when ammonia is insufficient in the sol-gel reaction ... 77

3.2 Iridescent planar silica opal deposited on quartz substrate ... 79

3.3 SEM image of the top layer of silica opal ... 80

3.4 Normal incidence optical transmission spectra of silica opals with different spherical diameters ... 81

3.5 Size dependence of the optical attenuation band position of silica opals ... 82

LIST OF FIGURES
(Continued)

Figure **Page**

3.6 Transmission spectra of 503nm opal at different incident angles 83

3.7 Reflection spectra of 503nm opal at different incident angles 84

3.8 Angular dependence of reflection peak position 85

3.9 SEM and EDX element analysis results 87

3.10 EDX mapping results of cobalt distribution in silica opal template 89

3.11 SEM image of SWCNT grown in synthetic silica opal template 90

3.12 Catalyst productivity in the CVD process to grow SWCNT in silica template made of 738 nm silica spheres 92

3.13 Comparison of catalyst productivity in opal templates made of silica spheres with different diameter 94

3.14 SEM images of carbon nanotubes grown inside opal templates made of silica spheres with different diameter 95

3.15 EDX spectroscopy results of SWCNT grown in opal template 96

3.16 Transmission spectra of 503nm opal template embedded with SWCNT measured at different incident angles 97

3.17 Reflection spectra of 503nm opal template embedded with SWCNT measured at different incident angles 98

3.18 Low frequency Raman spectrum of SWCNT 100

3.19 TEM image of single-wall carbon nanotube bundles 101

3.20 Kataura plot revealing energy separations $E_{ii}(d_t)$ versus nanotube diameter d_t for all (n, m) SWCNT 102

3.21 High frequency Raman spectrum of SWCNT 104

3.22 Lorentzian lineshape analysis of Raman G-bands 106

3.23 Optical activity of SWCNT embedded in silica opal template 107

3.24 I-V curve of SWCNT embedded in silica opal template 108

LIST OF FIGURES
(Continued)

Figure **Page**

3.25 Normalized conductance of SWCNT network embedded in silica opal template vs. time during UV illumination cycles (OFF/ON) in air 109

3.26 FTIR absorbance spectrum of PMMA inverse opal film made by in situ polymerization 111

3.27 Iridescent PMMA inverse opal film 112

3.28 SEM image of PMMA inverse opal 112

3.29 Optical reflection spectra of 503nm PMMA inverse opal at different incident angles 113

3.30 UV absorption spectra of PVK 115

3.31 SEM image of Polymer–SWCNT nanocomposite before the silica opal template was etched 116

3.32 Reflection spectrum of PMMA–SWCNT inverse opal 118

3.33 Raman spectra of PMMA–SWCNT composite 119

3.34 Raman spectra of PVK–SWCNT composite 120

3.35 I–V characteristics of polymer – SWCNT composite film 123

3.36 Normalized conductance of PVK–SWCNT composite embedded in silica opal template versus time during UV illumination cycle in air 124

3.37 Nonlinear transmission of SWCNT in silica opal template 126

3.38 Nonlinear transmission of SWCNT in silica opal template coated with PVK complex 127

3.39 Molecular structure of polyethylenimine 129

3.40 SEM image of SWCNT coated with PEI 130

3.41 High frequency Raman spectra of SWCNT from CarboLex before and after functionalized by polyethylenimine 131

3.42 Schematic diagram of formation of 3-D distributed p-n interface based on polymeric carbon nanotube composite 134

LIST OF FIGURES
(Continued)

Figure **Page**

3.43 Bragg diffraction probes the composition of porous PMMA composite consists of distributed p-n carbon nanotubes 135

3.44 Raman spectra of p-n distributed periodic structure 136

CHAPTER 1

INTRODUCTION

1.1 Photonic Crystals

1.1.1 The Concept of Photonic Crystals

The concept of photonic band gap (PBG) crystal, or photonic crystal (PX) was first introduced by Yablonovitch [1] and John [2] in 1987. A photonic crystal can be defined as an electromagnetic media in which the refractive index (RI) is periodically structured on a length scale comparable to the desired operation wavelength. These materials were called photonic crystal owing to the similarities in the behavior of photons therein and electrons in solids [3]. An electronic crystal can be viewed as a periodic structure built-up with basic units such as atoms or molecules. The atomic lattice is responsible for the periodicity in the electronic potential and acts on the electron wave function. As a direct consequence, the energy levels of electron are restricted to allowed energy bands separated by energy gaps. In the same way, photonic crystals present band gaps for photon states – ranges of frequency in which light cannot propagate through the structure. This analogy has opened up a new field in materials science and technology. Attractive new optical properties with revolutionary implications in technology have been predicted. Just to name a few of the most impressive applications: lossless frequency selective mirrors, quasi zero threshold lasers, super-collimators and super-lenses and wave-guides.

1.1.2 Photonic Band Structure

The photonic band structure provides information about the propagation properties of the electromagnetic (em) radiation within the photonic crystal. When light enters a photonic crystal, it is scattered at the interfaces between different dielectric regions. Due to the periodicity, scattering can be coherent for certain directions and frequencies. As a result, some propagation directions are forbidden for photons of certain energies (photonic ban gap). A complete photonic band gap (cPBG) occurs whenever certain frequencies would not propagate in any direction within the crystal.

Obtaining a complete photonic band gap strongly depends on having a high enough refractive index contrast δ. For a two dimensional square lattice, theoretical calculations show that no cPBG is possible unless $\delta > 4.0$. From a practical point of view, this means that achieving a cPBG in the optical regime is difficult since only a few materials possess large refractive index values. Fortunately, formation of cPBG is not only depended on a large refractive index contrasts. The choice of an appropriate symmetry and topology plays an important role as well.

To obtain a cPBG, the band gap for different propagation directions must overlap. Increasing δ usually helps to widen the gaps and facilitates overlapping. However, if band gaps for different directions open at very dissimilar energies, the overlapping is less pronounced. From solid-state physics, it is known that gaps occur for wave-vectors that lay at the Brillouin Zone (BZ) boundary. Consequently, photonic crystals with circular BZ will have a continuous gap for all directions and therefore, will be better suited for a material with complete photonic band gap. For 2-D photonic crystals, hexagonal lattice would be a wiser selection than a square one. In the case of 3-D lattice, the face entered cubic structure has the most sphere-like Brillouin zone. Figure 1.1 shows schematic images of the shape of the first Brillouin Zone of simple cubic (sc), body-center cubic (bcc) and face-center cubic (fcc) crystalline.

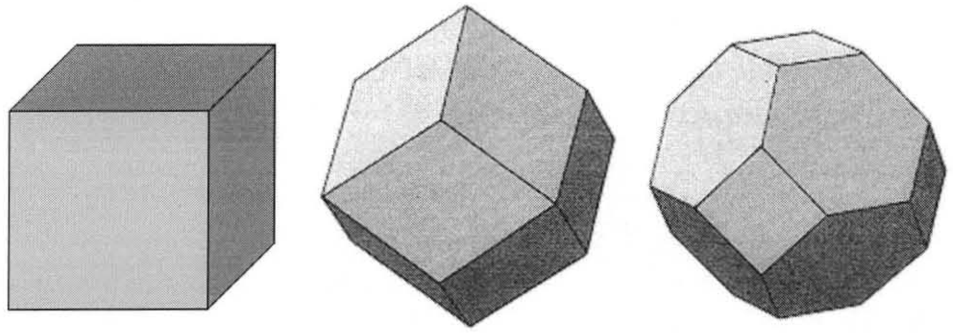

(a) (b) (c)

Figure 1.1 Schematic diagrams of the first Brillouin zone of (a) simple cubic, (b) body-center cubic, and (c) face-center cubic.

1.1.3 Fabrication of Photonic Crystals

Fabrication of photonic band gap materials at optical wavelengths requires nanometer-scaled 3-D periodic structures. In recent years, several approaches have been followed to fabricate 3D photonic crystals in the optical regime. Crystal periodicity varies from several hundred nanometers for applications in the visible (vis) range to a few microns for those applied to the near infrared (NIR). The techniques that have been most widely used include photo or electron-beam lithography, holographic lithography and self-assembly of colloidal crystal, such as artificial opal.

1.1.3.1 Three-Way Drilling. The first 3-D photonic crystal was proposed and fabricated by Yablonovitch [4] by simply drilling three sets of holes into the top surface of a solid wafer. A slab of material was covered by a mask that consists of a triangular array of holes. Three channels were drilled through each hole, at an angle 35.26° away from normal and spread 120°, as shown in left image of Figure 1.2. The resulting crisscross of channels below the surface of the slab produced a fully three-dimensionally periodic fcc void structure. The drilling can be done by a real drill bit for microwave work or by reactive ion etching for optical wavelengths. The right image of Figure 1.2

shows a 3-D Yablonovite-like photonic crystal produced by focus-ion-bean (FIB) micromachining [5], in which two more sets of cylinder holes were etched on a 2-D macroporous silicon crystal of triangular symmetry.

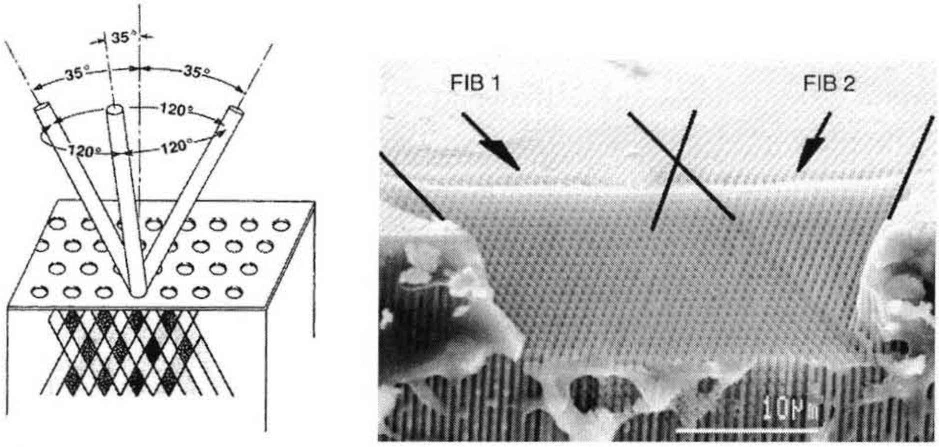

Figure 1.2 Yablonovite-like photonic crystal. Left – schematic three-way drill technique [4] of constructing an fcc lattice. Right – 3-D photonic crystal fabricated by focus-ion-beam milling of macroporous silicon [5].

1.1.3.2 Lithography. Lithographic techniques are based on the approach followed in microelectronics to fabricate electronic chips. The basic idea is to transfer a 2-D pattern onto a photosensitive surface by either photons or electron beams. Then, the pattern can be transferred to the substrate material by etching process. To build 3-D photonic crystals from this 2-D transferred pattern, two procedures have been developed by Noda *et al.* [6, 7] and Lin *et al.* [8, 9] They both ended up with a similar structure but with different names of either "woodpile" or "layer-by-layer", which depend on the different fabrication procedure. Noda and co-workers used a wafer-bonding technique. A basic 2-D structure of parallel bars was made on GaAs wafers by electron-beam lithography. Then two units were bonded face to face by wafer-fusion technique with bars in different layers situated perpendicularly to each other. Then one of the substrates was removed selectively and a 2-layer 3-D structure was obtained. After another 2-layer unit was fabricated, wafers were stacked and bonded again. This time, the third layer of bars should be parallel to the first layer but shifted by a half period (Figure 1.3). This was the most critical step that depended on a laser-beam assisted alignment. Alternatively, Lin *et al.* explored another way in which each layer was deposited one by one. SiO_2 layer was first deposited and patterned by photolithography, and then etched to a desired depth. The resulting trenches were filled with Si and resurfaced by mechanical polishing. The procedure was repeated layer by layer with proper orientation and alignment until the required structures were obtained. Finally, the remaining SiO_2 was chemically etched.

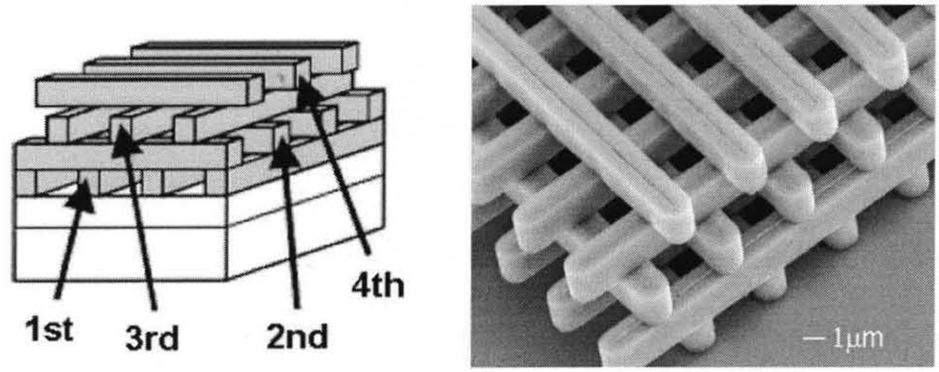

Figure 1.3 Woodpile photonic crystal by lithography. Left – schematic drawing of one unit of woodpile-structure 3-D photonic crystal; Right – woodpile structure built by photolithographic technique by wafer fusion [7].

Although lithography is a classic technique in microfabrication industry and therefore is an attractive way to build 3-D photonic crystals, it is also a complicated and expensive way requiring state-of-the-art facilities.

1.1.3.3 Holography. Holographic lithography technique is built upon light interference. Applying holography in the fabrication of 3-D photonic crystal was first proposed by Berger *et al.* in 1997. The key point of their idea was that photonic band gap materials could be viewed as a particular class of holograms with extremely high refractive index contrasts [10]. Therefore photonic crystals may be constructed with a simple holographic recording with a mall number of optical plane waves. Campbell *et al.* [11] developed this technique and reported the first photonic crystal constructed by 3-D holographic lithography. They adapted interference of four non-coplanar coherent laser beams to form the structure, as shown in Figure 1.4. The structure is periodic with controlled periodicity and symmetry. Firstly an interference pattern is formed by the lasers within a negative-type photoresist. Highly exposed areas became insoluble because of cross- linking reaction. Unexposed photoresist is then dissolved away to reveal a 3-D structure formed of cross-linked polymer with air-filled voids. The wave vector, intensity, and polarization of each laser beam determined the symmetry and lattice constant of the interference pattern, which in turn determines the photonic band structure [12].

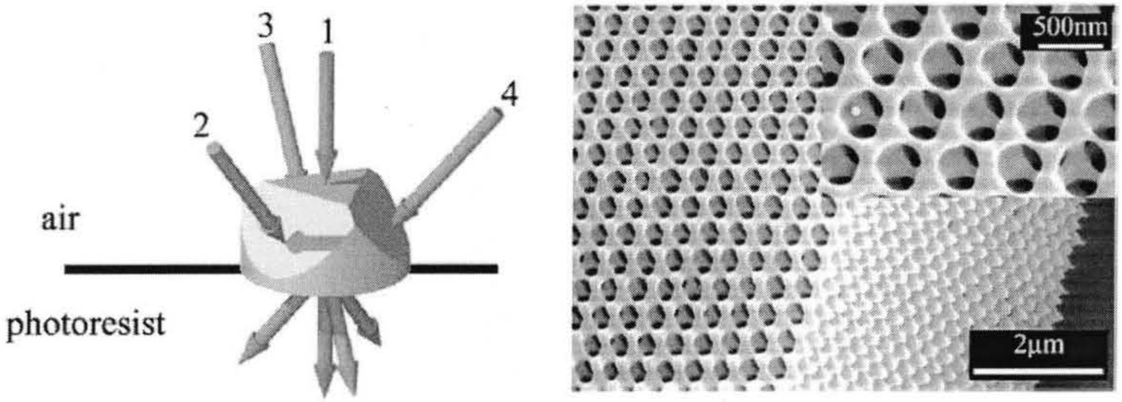

Figure 1.4 Polymeric photonic crystal by holography [11]. Left – scheme of laser holography employing four laser beams in the umbrella-like configuration; Right – resultant 3-D polymeric photonic crystal.

Holographic lithography has several advantages. First, it removes the requirement for an expensive patterned photomask. Second, the 3-D photonic crystal may be obtained in a short time of several minutes. Third, considerable freedom to design different symmetries and unit cell distribution is available by controlling the interference pattern.

1.1.3.4 Artificial Opal. Artificial opal [13] is a colloidal crystal with a naturally formed fcc symmetry. The crystalline array is made of highly monodisperse spheres of dielectrics, such as silica or polymer. The periodicity of the crystal may be in the range of sub-micrometers and is dictated by the sphere diameter. Figure 1.5 left shows a SEM image of a close-packed planar array of spherical silica colloids with an average diameter of 295 nm. The [111] crystallographic direction is normal to the substrate plane. Self-assembled colloidal crystals offer an inexpensive yet efficient way of fabricating periodic structures. Such crystal doesn't exhibit a complete photonic band gap because of its low refractive index contrast between the spherical colloids (either silica or polymers) and air, it does provide a convenient 3-D periodic template to fabricate crystals of other materials. After infiltrating the opaline structure with a high refractive index material following by selectively etching away the template, a structure of air spheres in a dielectric material matrix is obtained. The right image of Figure 1.5 shows an example of the resultant structure after etching away the template. The inset displays an enlarged view of the internal structure of these air spheres. From this (111) facet, three channels which connect each sphere with three others in the layer underneath can be clearly observed. This macroporous dielectric media with oriented and crystalline arrays of air sphere is the kind of crystal which exhibits a complete photonic band gap [14].

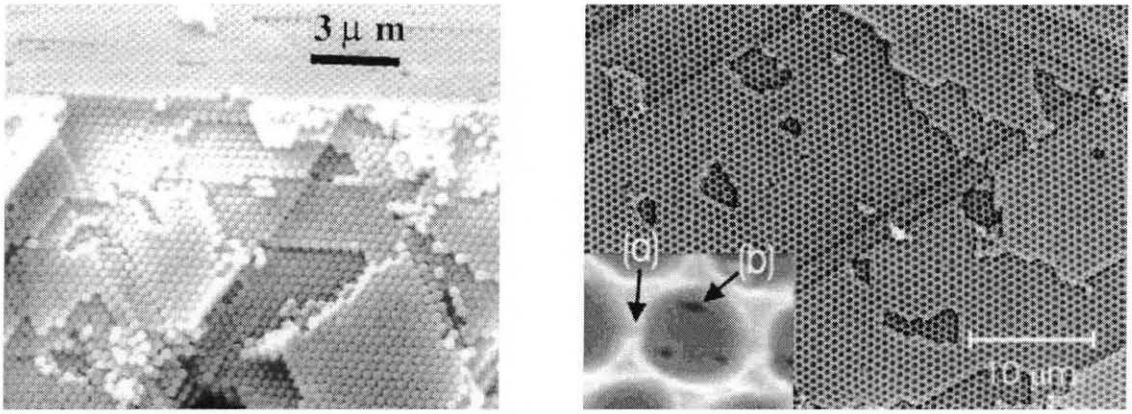

Figure 1.5 Synthetic silica opal. Left – SEM image of silica synthetic opal with a close-packed array of silica spheres [17]. Right – SEM image of a polymer inverse opal. The inset shows the three channels connecting the air sphere with three others underneath [18].

The first inverse opaline structure was made by Velve *et al.* [15] in 1997. In their work a crystalline structure was assembled from polystyrene microspheres and was used as a template for silica polymerization. Subsequently the latex was burned, leaving the desired air-sphere structure. Following this first successful attempt, many other groups demonstrated inverse structures with polymers [16,17,18] (such as polyurethane, epoxy and PMMA *et al.*) and inorganic materials (such as carbon [19], titania [20] and silicon [21,22]). The optical properties of these inverse structures have been intensively investigated.

Self-assembly of colloidal crystals offers some advantages. Firstly, there is a potential to create samples with full three-dimensional ordering, a feature important for engineering larger and more complete photonic band gaps. Secondly, self-assembly methods can create thicker materials than those made using lithography. Thirdly, self-assembly methods are not limited in their length scale and it is feasible to create materials that are active in the ultraviolet and even in the X-ray range using colloids with smaller diameters. Finally, colloidal crystals provide an ideal template for polymeric and inorganic crystals with complex porous structures.

Compared to latex spheres, silica opals are particularly useful as a host template when the synthesis of infiltrated materials require extreme conditions. Silica is thermally stable at relatively high temperatures and is chemically inert in the presence of most solvents and in particular organic solvents. Nevertheless, silica opals can be etched away at room temperature by diluted hydrofluoric acid, for which most polymers are inert, making it is possible to fabricate a wide range of polymeric inverse structures..

1.1.4 Application of Photonic Crystals

Semiconducting material based PBG crystals, such as Si, Ge, and GaAs, may open the door to applications in telecommunications and laser devices because of their light localization properties. Fabrication of integrated circuits in which information carriers are photons instead of electrons is one of the most expected applications for photonic crystals.

To guide electromagnetic waves along a line, two main designs are commonly employed. One is metallic pipe waveguides, which can be used to steer light around tight corners but provide lossless transmission only for microwaves. Dielectric waveguides are used at infrared and visible radiation. The operation of conventional dielectric guides, based on the principle of total internal reflection, is restricted by radiation losses to moderate curvature bends. In fact, when light is steered around a corner in such a guide, it is well known that the radius of curvature must be larger than the wavelength of the light to avoid large losses. Researchers at MIT [23] showed that a linear defect region in a photonic band-gap (PBG) material could support a linearly localized mode when the mode frequency fell inside the gap of the surrounding full periodic crystal. These modes could be strongly confined to the defect regions. Such a defect could act as a waveguide for electromagnetic (EM) waves, without relying on total internal reflection. Furthermore, it has been shown that PBG waveguide could efficiently guide light around sharp corners [24, 25].

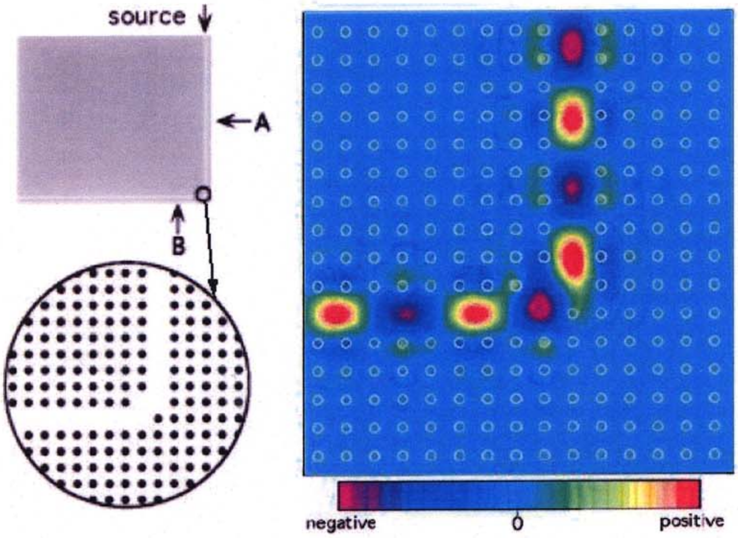

(a)

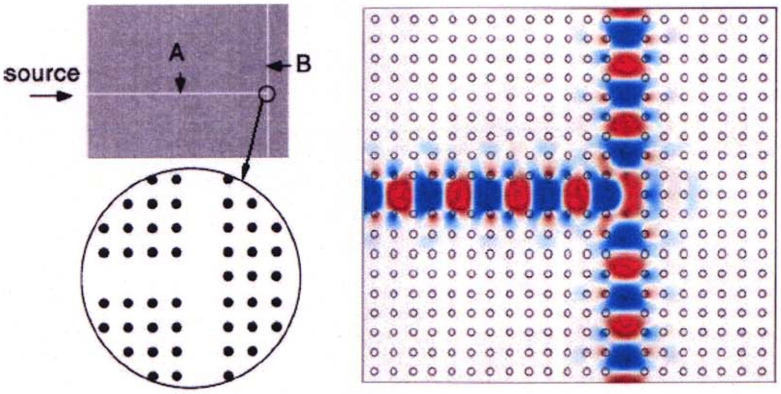

(b)

Figure 1.6 Examples of optical waveguide design based on 2-D photonic crystal [24,25]. In both (a) and (b), left image presents a schematic view of the computational cell of a 2D photonic crystal and right image shows the electric field pattern in the vicinity of the bend and branch.

Figure 1.6 (a) and (b) show a numerical simulation for two examples of optical waveguides based on 2-D photonic crystals. It demonstrated highly efficient transmission of light around sharp corners and the radiation losses were low for a wide range of frequencies and even vanished for some frequencies, although the radius of curvature of the bend was on the order of one wavelength. Actually, optical fibers based on photonic crystals have already been commercialized [26,27,28]. The principle on which it relies is the same as optical waveguides mentioned above and differs from conventional optical fibers guiding light by total internal reflection.

The other possible applications of inorganic photonic crystal are for laser devices, such as lossless frequency selective mirrors, quasi-zero threshold lasers and super-collimators and super-lenses.

Besides traditional inorganic material, especially semiconductor materials, organic nano-structured photonic crystals also find their way in optical applications. High-density 3-D optical data storage was reported by Siwick [29]. The nanocomposite was made of core-shell latex particles with dye-labeled polymer as the core material. After self-assembly of the latex particles into a 3-D close-packed crystalline structure, high temperature was applied to fuse the optical inert latex shell into a bulk media. The fluorescent core particles were periodically embedded in the bulk latex. Information was recorded by optical bleaching of individual photosensitive particles with a 5 mW average power laser and was read out with much lower laser power. The laser pulses were typically 100fs centered at 844 nm. A significant reduction in writing and reading cross talk was structure-induced because of the optical inert separation between the information carriers. The effective optical storage density was increased by a factor of 2 over conventional homogeneous storage media.

1.1.5 Polymer Inverse Opal

Theoretical calculations show that high index of refraction values (n > 2.8) [30] are required for inverse photonic structure to exhibit a complete band gap. Generally, polymers have index values in a range of 1.4-1.5, which are not as high as their inorganic counterparts. Inverse polymeric opal only exhibits an incomplete photonic band gap over a smaller range of wavelengths and incident angles. However, this partial band gap is a useful property in numerous linear optical applications, such as wavelength rejection filters.

In past ten years, inverse polymer opals have been attracting attention because of their diversity and low-cost. Infiltration of polymer into the template is relatively easy. The polymerization process results less final volume shrinkage than inorganic materials made by gaseous precursor decomposition [31]. This allows for a nearly 100 % infiltration of polymers and consequently results in an inverse opaline structure with much less crack defects.

Xia, *et al.* [16] first fabricated macroporous polymer membranes with highly ordered and 3-D interconnected spherical pores from UV-curable polyurethane. The latex spheres were self-assembled into 3-D crystalline template and then dissolved in toluene after infiltration of the polyurethane. Following this idea, other polymers [17, 18] like poly(methyl methacrylate) (PMMA), poly(styrene) (PS), poly(urethane) and epoxy were also employed into the fabrication of inverse polymer opal.

Conductive polymers or copolymers were also considered for inverse photonic structures in a hope that these functionalized polymers may enable photonic band gap tuning by either thermal or optical means. A 3-D periodic ferroelectric polymer-silica opal composites and inverse opal were reported by Xu, *et al.*, which was the first [32] pure copolymer inverse opal ever been made. A high temperature solution infiltration process was developed to infiltrate P(VDF-TrFE) copolymer into silica opal lattice. The resultant inverse copolymer preserved the 3-D lattice and remained in a ferroelectric state. The existence of interface between copolymer and air induced external stresses and changed the ferroelectric-paraelectric transition temperature. This effect was suggested to facilitate a conversion of copolymer from a normal ferroelectric state into a relaxor ferroelectric state with a large electrostrictive strain.

Some photoconductive polymers with long side chains, such as poly(3-alkylthiophene) (PAT), were used to make inverse opals. These polymers are fusible at high temperature and soluble in common solvents and may infiltrate silica opal templates. Poly(3-alkylthiophene) inverse opal was produced and studied by Ootake, *et al.*[33] They found that the reflection spectra of the material changed as the temperature increased, which was explained by thermochromism due to the conformation change of PAT. This result shows that photonic crystal based on photoconductive polymer inverse opal presents a thermally or optically tunable refractive index.

Conjugated polymer inverse opals were used as biosensor [34]. Generally, biological catalysts (enzymes) are used in biosensors to recognize and monitor a target molecule in a biological fluid. To fabricate such a sensor, enzymes may be immobilized by physical adsorption, covalent attachment or embedded within thin films. By electro-chemical deposition of enzyme and conducting polymer on a substrate, the enzyme would be trapped within the polymer film without leaching out and have accessibility to the target molecules (analyte) in a biological fluid when they permeate through the film. The prerequisite of sensitivity of such a biosensor is that the film will be highly porous and permeable to biological fluids. Conductive polymer inverse opals meet this requirement.

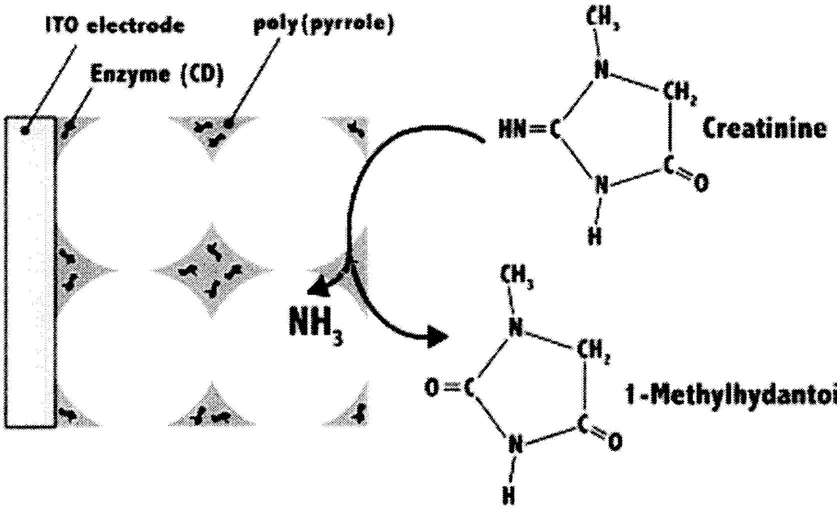

Figure 1.7 Schematic drawing of the sensing operation of a creatinine deiminase-doped Ppy inverse opal exposed to a buffered creatinine solution.

Cassagneau *et al.* designed a potentiometric biosensor made of enzyme (creatinine deiminase) doped poly(pyrrole) inverse opal, as shown in Figure 1.7. When creatinine solution penetrated into the matrix, the enzyme catalyzed its conversion into 1-Methylhydantoin and ammonia. The latter was responsible for modulating the pH within the film, which induced a sensing response as a change of the film electrical potential. In this practical design, the average thickness of the polymer wall was 70-75 nm. A seven-fold enhancement of the sensitivity and increased propensity to interact with nucleophilic molecules was reported in this research.

1.2 Carbon Nanotubes

Since the discovery of multi-wall carbon nanotubes in 1991 by Iijima [35] and subsequent synthesis of single-wall carbon nanotubes [36,37], there have been numerous experimental and theoretical studies of their electronic, chemical, and mechanical properties. Chemical stability, diverse electronic properties (ranging from 1 eV band gap semiconductors to metals), and predicted extreme strength of the nanotubes have placed them as fundamental building blocks in the rapidly growing field of nanotechnology. Diverse nanoscale device concepts have been proposed to develop nanoscale electronic devices, chemical sensors, and also high strength nanotube composite materials with sensing and actuating capacity.

1.2.1 Structure of Single-wall Carbon Nanotubes

A single-wall carbon nanotube (SWCNT) is best described as a rolled-up tubular shell of graphene sheet (Figure 1.8) [38, 39]. The body of the tubular shell is mainly made of hexagonal rings of carbon atoms, where as the ends are capped by dome-shaped half-fullerene molecules. The natural curvature in the sidewalls is due to rolling of the sheet into the tubular structure, whereas the curvature in the end caps is due to the presence of topological (pentagonal ring) defects in the otherwise hexagonal structure of the underlying lattice. The role of the pentagonal ring defect is to give a positive (convex) curvature to the surface, which helps in closing of the tube at the two ends. A multi-wall carbon nanotube (MWCNT) is a rolled-up stack of graphene sheets into concentric SWCNT, with the ends again either capped by half fullerene or kept open.

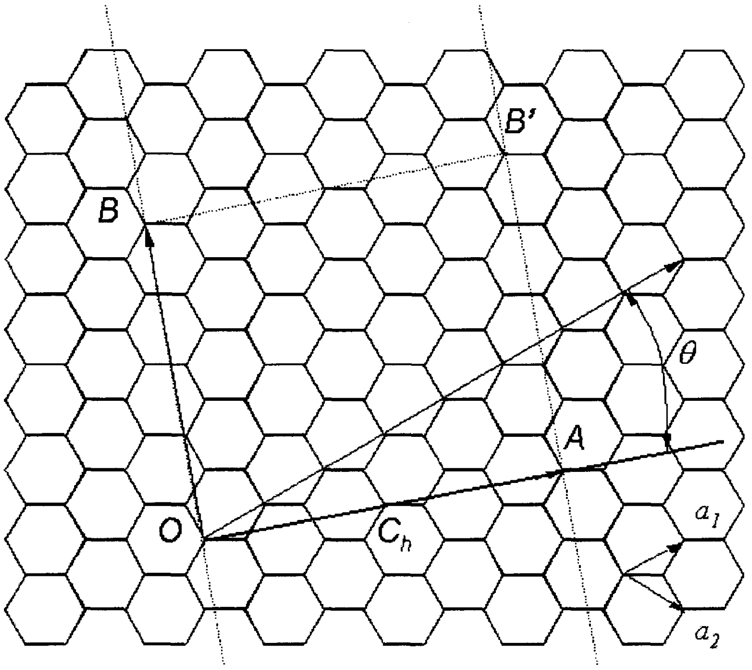

Figure 1.8 Schematic structures of single-wall carbon nanotubes as an unrolled honeycomb lattice [38]. Vector ***OA*** (***C_h***) is the chiral vector. ***OB*** is the axial direction of the tube. a_1 and a_2 are unit vectors of the hexagonal lattice. θ is the chiral angle that extended from zigzag direction to armchair direction.

The structure of a single-wall carbon nanotube is specified by a vector ***OA*** (***C_h***) that determines the direction along which the graphene sheet is rolled to form the tubular shell structure and is perpendicular to the tube axis, as shown in Figure 1.8. The chiral vector ***C_h*** is extending from the zigzag direction to the armchair direction, which forms two limiting cases. Vector ***OB*** is the direction of the nanotube axis. Now consider the crystallographic equivalent sites *O*, *A*, *B*, and *B'*, by rolling the honeycomb sheet so that points *O* and *A* coincide and *B* and *B'* coincide, a model of single-wall carbon nanotube can be constructed. The chiral vector ***C_h*** can be expressed by two real space unit vectors a_1 and a_2 of the hexagonal lattice:

$$C_h = na_1 + ma_2 = (n, m), \qquad (1.1)$$

where n and m are both integers. This nomenclature (n, m) is usually used to identify each single-wall nanotube, which refers to the integer indices of two unit lattice vectors corresponding to the chiral vector of a nanotube.

The diameter of a carbon nanotube is defined as:

$$d_t = L/\pi, \tag{1.2}$$

where L is the circumferential length of the tube and can be calculated from the chiral vector C_h.

$$L = |C_h| = \sqrt{C_h \cdot C_h} = a\sqrt{n^2 + m^2 + nm}\ . \tag{1.3}$$

Here a is the lattice constant, the length of the unit vector of the hexagon lattice. It can be calculated from the length of C – C σ bond, which is 1.44 angstrom in single-wall carbon nanotubes.

$$a = 1.44 \times \sqrt{3}\ \text{Å} \tag{1.4}$$

The chiral angle θ is defined as the angle between the chiral vector C_h and the zigzag direction. It can be easily calculated from integers n and m:

$$\cos\theta = \frac{2n + m}{2\sqrt{n^2 + m^2 + nm}}\ . \tag{1.5}$$

The symmetry classification of a carbon nanotube is either achiral or chiral. An achiral carbon nanotube is defined by a carbon nanotube whose mirror image has an identical structure to the original one. There are only two cases of achiral nanotubes – armchair and zigzag nanotubes. The names came from the shape of the cross-sectional ring, as is shown at the edge of the nanotubes (see Figure 1.9, upper and middle images). Chiral nanotubes exhibit spiral symmetry, as shown at the bottom image of Figure 1.9, whose mirror image cannot be superposed onto the original one.

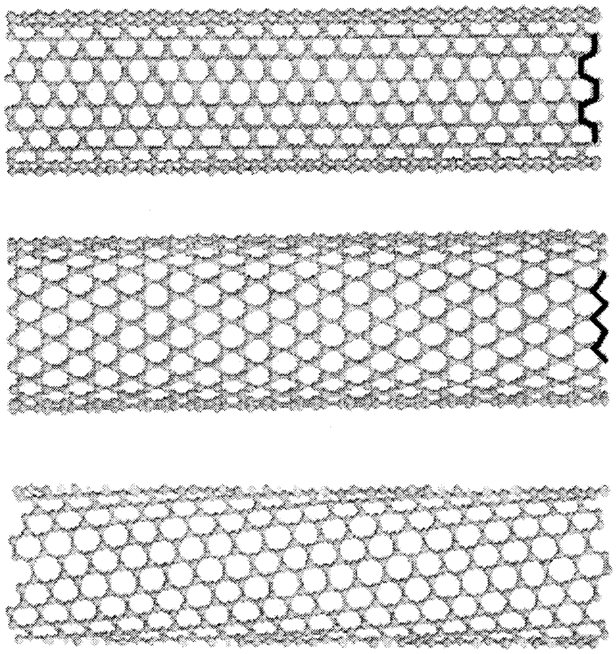

Figure 1.9 Schematic structure of single-wall carbon nanotubes from side view. Upper – armchair nanotube; Middle – zigzag nanotube; Bottom – chiral nanotube.

Table 1.1 Classification of Single-wall Carbon Nanotubes

Type	θ	C_h	**Shape of cross section**
Armchair	30°	(n, n)	*cis*-type /‾_/‾\
Zigzag	0°	(n, 0)	*trans*-type /\/\/\/\
Chiral	$0^{\circ} < \|\theta\| < 30^{\circ}$	(n, m)	mixture of *cis* and *trans*

A brief summary of the chiral structure of SWCNT is presented in Table 1.1. When the chiral angle equals 0°, the nanotube is defined by the vector (n, n) and armchair-shaped (_/‾_/) rings perpendicular to the tube axis. Armchair tubes have symmetry along the axis with a short unit cell of 0.25 nm that can be repeated to make the entire section of a long nanotube. When the chiral angle equals 30°, $m = 0$, the chiral vector (n, 0) represents zigzag nanotubes because of the /\/\/ shaped rings perpendicular to the axis. Zigzag nanotubes have a unit cell of 0.43 nm along the tube axis. All the remaining nanotubes are known as chiral or helical nanotubes and have longer unit cell sizes along the tube axis. Details of the symmetry properties of the nanotubes of different chiralities are explained in detail in References 38 and 39.

1.2.2 Fabrication of Single-wall Carbon Nanotubes

Several methods exist today to synthesize single-wall carbon nanotubes, including electric arc-discharge, laser ablation, and catalytic chemical vapor deposition. In all of these, carbon vapor is made to condense into tubular structures, with or without the presence of catalysts.

1.2.2.1 Arc Discharge. Single-wall carbon nanotubes were first discovered in the soot of an arc process used for making fullerenes [40]. The carbon arc is a traditional technique to generate high temperatures, usually higher than 3000 ^{o}C, which is required to vaporize carbon atoms and to synthesize single- or multi-wall carbon nanotubes.

The typical electric arc-discharge apparatus consists of two graphite rods as electrodes in a sealed reactor chamber. A DC voltage across the electrodes is about 30 V with a current about 100 A [41]. A constant Helium flow is usually maintained for cooling purpose. In the case of multi-wall carbon nanotube synthesis, no catalyst is needed. However, the synthesis of SWCNT requires transition metals such as Co, Ni and Fe, or bi-metallic catalyst like Co/Ni and Y/Ni to be used. Generally, catalysts fill a hole which is drilled on the graphite anode. Once the arc is in operation, all possible carbon products deposit on the region of cathode in forms of soot, webs and string-like structures [42]. The length of graphite anode decreases as the operation continues and it has to be continuously moved forward to maintain a constant distance to the cathode.

The detailed structure (such as chirality and diameter distribution) of the resultant SWCNT depends on the synthesis conditions, temperature of the arc and the catalyst used. However, the diameter of nanotubes produced by this technique is typically smaller than 1.5 nm.

1.2.2.2 Laser Ablation. Short-pulsed laser irradiation can induce a range of fast non-equilibrium processes in the irradiated target. These fast processes include strong overheating, fast melting, explosive boiling and massive material removal (ablation) [43]. Recently, pulsed laser ablation has been practically used in surface micro/nano-processing, deposition of thin films and coatings, and laser surgery and mass spectrometry of biomolecules.

An efficient way to synthesize bundles of single-wall carbon nanotubes with a narrow diameter distribution employs a short-pulsed laser-ablation process to vaporize a graphite target. The earliest reports about application of laser ablation technique on the synthesis of single-wall carbon nanotubes came from Smalley's group [44, 45]. A scanning laser beam (532 nm, 300 mJ/pulse at 0.532 ms) was used to directly vaporize a transition-metal/graphite composite rod in a heated flow tube. Different metal and metal concentration in carbon composite target were studied. The results showed that the yield always increase with temperature up to a maximum of 1200 °C. As single-metals catalyst, Ni produced the largest yield, followed by Co. Pt yielded a very small number of tubes, while no tubes were observed with Cu or Nb alone. For bi-metal catalysts, Co/Ni (0.6/0.6 in atom%) and Co/Pt (0.6/0.2) mixtures yielded SWCNT in similarly high abundance, with 10-100 times higher yield than that of using single metals alone. Ni/Pt and Co/Cu mixture produced a small quantity of nanotubes. The best catalyst Co/Ni alloy showed a ~50 % conversion of graphite to single-wall nanotubes. Two sequenced laser pulses were used to improve the productivity of nanotubes to 70 % to 90 %. The nanotubes produced by laser ablation were generally with uniform diameter and self-organized into ropelike crystallites. Compared with the nanotubes synthesized with metal-catalyzed arc-discharge method, these tubes were found with less amorphous carbon coatings.

1.2.2.3 Chemical Vapor Deposition. Chemical Vapor Deposition (CVD) is heterogeneous chemical reaction in which gaseous molecules, called precursor, are thermally or/and catalytically transformed into solid and volatile materials. The solid products are then deposited on the surface of a substrate in the form of thin film or powder. CVD method was first developed by smalley's group in 1996 to produce single-wall carbon nanotubes from catalytic decomposition of carbon monoxide [46]. Different approaches were proposed to grow SWCNT by catalytic decomposition of carbon-containing vapors. Different carbon feedstocks, different formulae of catalyst/catalyst supports, different operation temperatures have been investigated. The most popular approaches use carbon containing gaseous resources such as, methane (CH_4) [47, 48], carbon monoxide (CO) [49, 50, 51, 52, 53, 54], ethanol (C_2H_5OH) and other hydrocarbon such as, benzene (C_6H_6) [55, 56] and acetylene (C_2H_2) [57, 58].

Carbon monoxide has been the first carbon feedstock used for the growth of single-wall carbon nanotube by chemical vapor deposition (CVD) [46]. Disproportionation of CO was performed at 1200 °C with the presence of Mo or Mo/Co catalyst. The CO pressure was held at ~100 Torr above atmospheric pressure. The resulted tube diameters, ranging from 1 to 5 nm, closely correlated with the size of the catalytic particle found attached to the tube end. This result represented the first experimental evidence of SWCNT produced by pre-formed catalytic particles.

Compared to other hydrocarbon CVD growth techniques, reports on carbon monoxide as feed gas is less common because of its poison. However, this technique offers certain advantages for carbon nanotubes growth, such as relatively low temperatures (700-800 °C) in comparison to using methane (~ 1000 °C). A detailed comparison [50] between CO and CH_4 as carbon feed gas was reported by Liu's group. Analysis of Raman spectra suggest that diameter distribution of the nanotubes synthesized by CO (1.0-1.5 nm) is narrower compared with products made by methane (0.9-2.7 nm). The higher purity of SWCNT with less amorphous carbon from CO process compared to CH_4 has been reported and explained by the thermo-equilibrium properties of the reactions:

$$CH_4 \longleftrightarrow C + 2H_2 \qquad \Delta H^\circ = +74.4 \text{ kJ/mol} \tag{1.6 a}$$

$$2CO \longleftrightarrow C + CO_2 \qquad \Delta H^\circ = -172 \text{ kJ/mol} \tag{1.6 b}$$

Equation 1.6 (a) shows that higher temperature favors carbon formation from CH_4 decomposition. At higher temperature (> 800-900 °C), the pyrolysis rate of methane will overwhelm the growth rate of carbon nanotubes, resulting in an undesirable amorphous carbon coating on nanotubes. On the other hand, higher temperatures are desirable in order to anneal away defects that form in the growth stage of carbon nanotubes. Carbon monoxide as a carbon source does not suffer from this dilemma. While improve the quality of growing tubes, increased temperature doesn't favor CO disproportionation, which prevents excessive yield of carbon in amorphous formation.

Resasco's group developed Co-MoCat process [51] which adopted bimetallic catalyst Co-Mo on SiO_2 platform. By temperature programmed oxidation (TPO) experiments, they could conduct systematic screening of catalyst formulations and operating conditions. The resulted best catalyst composition contains 6 wt % total metals and Co:Mo molar ratio 1:2, which exhibited the highest selectivity towards SWCNT.

A serial of experiments aimed at studying Co/Mo bimetallic catalyst were conducted by Lan *et al.*, which demonstrated an extensive growth of SWCNT with only cobalt as catalyst [54]. This process resulted in a near-100 % yield of essentially defect-free chiral tubes. The nano-scaled cobalt particles were deposited by laser ablation, sputtering and electrochemical means.

Besides differences in metallic catalysts components used, methods differ by the way catalysts are administered. One way is by using pre-formed nanometer-sized metal particles. An alternative technique is gas-phased continuous-flow catalytic method [34, 37-40]. The continuous flow synthesis in especially convenient because metal can be introduced in the form of volatile organometallic molecules. This method typically involves passing a mixture of carbon feedstock gas and organometallic catalyst precursor through a heated furnace. The organometallics decompose and react, forming very fine metal clusters on which carbon nanotubes can nucleate and grow.

Chemical vapor deposition has shown several clear advantages compared with arc and laser methods for SWCNT growth. First, CVD has been used in microelectronic industry for tens of years to deposit thin films. Laboratory successes in producing nanotubes can be more easily scaled-up to industrial level production; secondly, both arc and laser methods involve extremely high temperature to evaporate the solid carbon. The strict equipment requirements and large energy-consumption make these methods practical in only research laboratories. In contrast, CVD can be running under 1000 degrees, using carbon-rich gases as carbon feedstock. Energy efficiency makes CVD an attractive way of SWCNT mass-producing. Finally, and most importantly, by controlling proper experimental conditions, such as temperature, feeding gas and catalysts, more control over the morphology and structures of the nanotubes is achieved. Evaporation methods generally produce nanotubes in highly tangled forms, mixed with metallic catalyst particles. The resultant nanotubes are difficult to purify, manipulate and assemble for device architectures. On the other hand the CVD method enables purer and well-separated SWCNT. All of the reports on patterned growth of SWCNT [59, 60, 61, 62, 63, 64] were based on this technique.

1.2.3 Electronic Properties of Single-wall Carbon Nanotubes

The electronic structure of SWCNT can be derived by a simple tight-binding calculation [65] for the π-electrons of carbon atoms. The energy band structure of the 2-D graphite sheet is given by:

$$E_{2D} = \pm\gamma_0 \left[1 + 4\cos(\frac{\sqrt{3}k_x a}{2})\cos(\frac{k_y a}{2}) + 4\cos^2(\frac{k_y a}{2}) \right]^{\frac{1}{2}}, \qquad (1.7)$$

where γ_0 is the nearest-neighbor overlap integral, a is the lattice constant and k_x and k_y are components of the two-dimensional wave vector $\boldsymbol{k}$ in the hexagonal Brillouin zone [66].

In the case of single layer graphene tubule, which is single-wall carbon nanotube, with the exception of very small diameter tubes, the energy band structure resembles that of graphite. The main difference between graphite and the tubule lies in the imposed periodic boundary conditions. For a tubule, the boundary condition along the tubule axis is the same as for graphite. In the circumferential direction (along the chiral vector $\boldsymbol{C_h}$), periodic boundary condition

$$\boldsymbol{C_h} \cdot \boldsymbol{k} = 2\pi q \qquad (1.8)$$

is imposed due to the finite period along the circumference. Here $\boldsymbol{k}$ is the wave vector and q is an integer. This condition leads to a set of allowed $\boldsymbol{k}$-values which are substituted into the energy dispersion relation (Equation 1.7) for a graphene sheet to yield a one-dimensional energy band structure for the single-wall carbon nanotube.

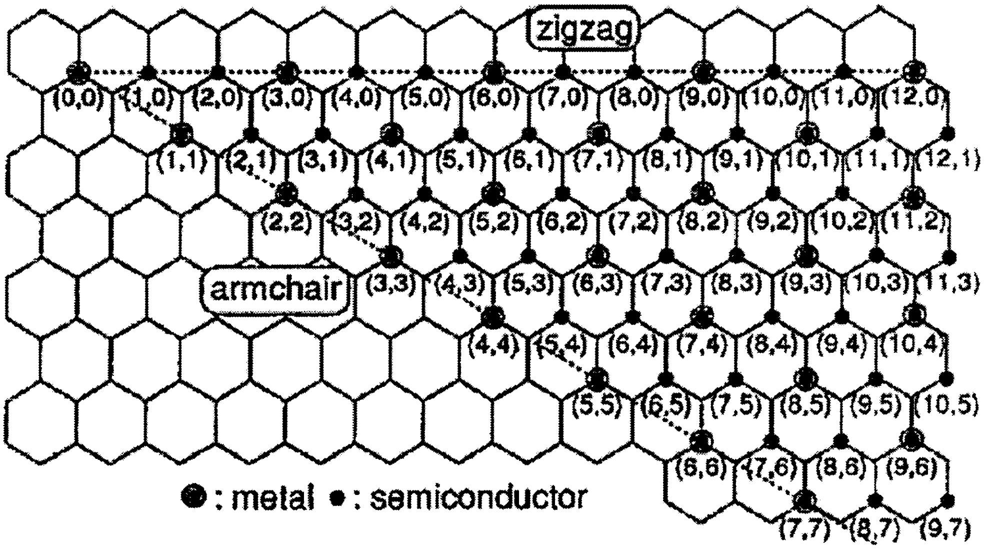

Figure 1.10 Schematic diagram showing the carbon nanotubes (n, m) that are metallic and semiconducting [66].

It is surprising that the calculated electronic structure of a carbon nanotube can be either metallic or semiconducting, depending on the tubule diameter and chirality, though there is no difference in the local chemical bonding between the carbon atoms and no other doping atoms were present. The calculation [66] shows that the condition for a metallic nanotube is ($2n + m$), or equivalently, that ($n - m$), is a multiple of three, as denoted in Figure 1.10. All the other (n, m) tubes are predicted to be semiconductor with an energy gap on the order of ~ 0.5 eV. This gap should depend on the diameter, as [67]

$$E_{\text{gap}} = 2\,\gamma_0\, a_{\text{c-c}}/d. \tag{1.9}$$

Here, γ_0 is the C-C tight-binding overlap energy, $a_{\text{c-c}}$ is the nearest carbon-carbon distance and d is the diameter of the tube. Obviously, Zigzag (n, 0) SWCNT should have two distinct types of behavior: the tube will be a metal when $n/3$ is an integer; otherwise it is semiconductor. The (n, n), or armchair, tubes are expected to be truly metallic.

The theoretical predications have been eventually verified by experiments [68, 69]. The results of Scanning Tunneling Microscopy and Spectroscopy (STMS) measurements on individual SWCNT were reported in 1998, in which atomically resolved images (Figure 1.11) provided a clear view. By examining the electronic properties as function of tube diameter and chiral angle, both semiconducting and metallic carbon nanotubes were observed. It was found that the electronic properties indeed depend sensitively on minor variations of wrapping angle or the diameter.

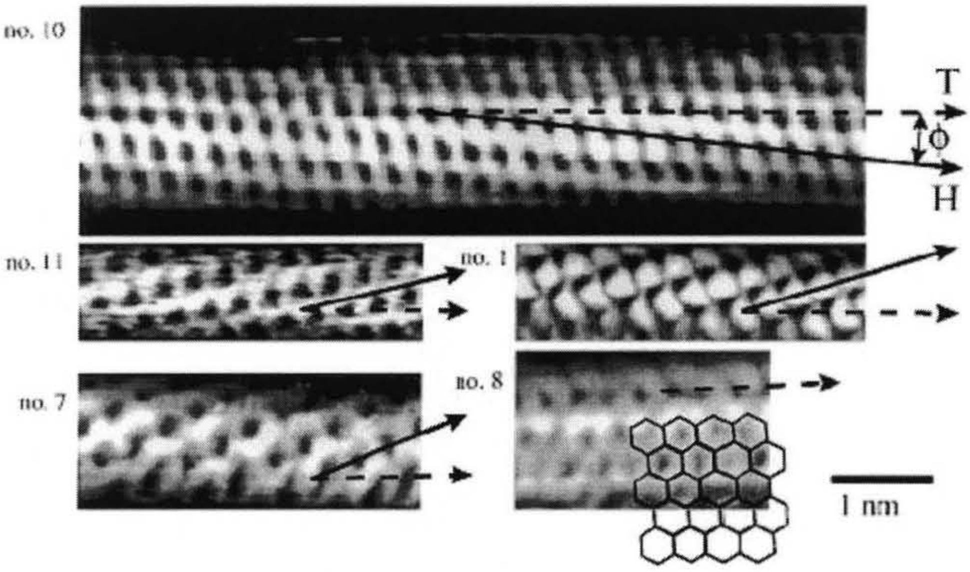

Figure 1.11 Atomically resolved STM images [68] of individual SWCNT. The lattice on the surface of the cylinders allows a clear identification of the tube chirality. Dashed arrow T represents the tube axis and solid arrow H represents zigzag direction. Tubes no. 10, 11 and 1 are chiral, no. 7 and 8 are zigzag and armchair respectively. A hexagonal lattice is plotted on top of image no. 8 to clarify the non-chiral armchair structure.

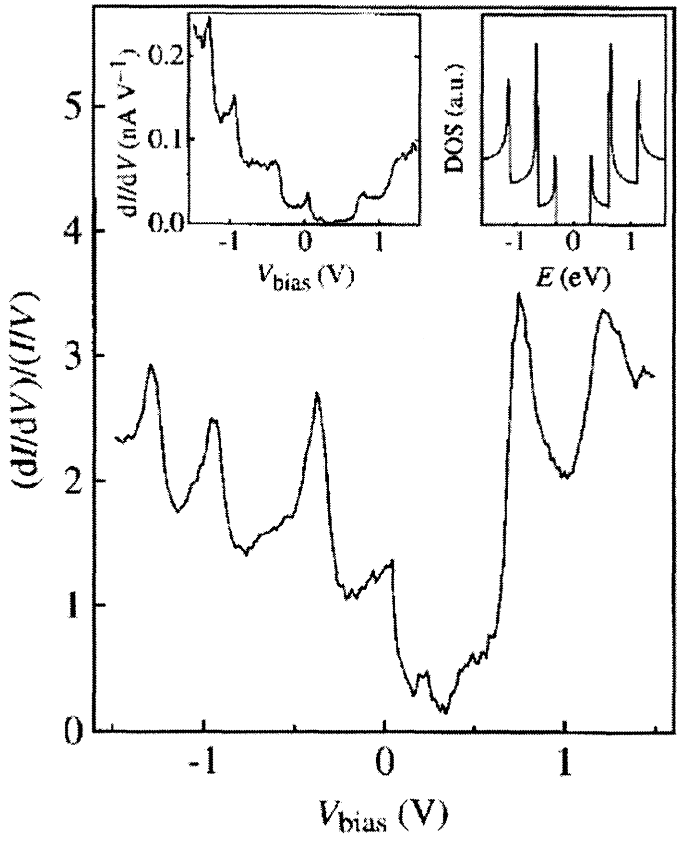

Figure 1.12 (d*I*/d*V*)/(*I*/*V*), which is a measure of the DOS, versus V for single-wall carbon nanotubes [68]. The asymmetric peaks correspond to singularities at the onsets of 1-D energy bands of carbon nanotubes. The left inset displays the d*I*/d*V* data. The right inset displays a typical example of the spike-like DOS for a semiconducting tube.

Besides the diverse electronic properties (semiconducting or metallic) predicated by the theoretical works, the calculated band structure of SWCNT also indicated spike-like density of states (DOS) because of its 1-D structure [66]. The $1/\sqrt{E}$ singularities characteristic of 1-D energy bands appear at the band edges of each energy band. This prediction was also observed and verified by Scanning Tunneling Spectroscopy (STS) technique that was used to record the current – voltage characteristics of individual carbon nanotubes [68]. The derivative d*I*/d*V* or (d*I*/d*V*)/(*I*/*V*) curves verified that the energy gap for a semiconductor nanotube is inversely proportional to its diameters. Sharp peaks were observed on (d*I*/d*V*)/(*I*/*V*) plot (Figure 1.12) indicating the singularities of the density of state (right inset of Figure 1.12). The direct experimental observation showed a good agreement with the tight-binding zone-folding calculation.

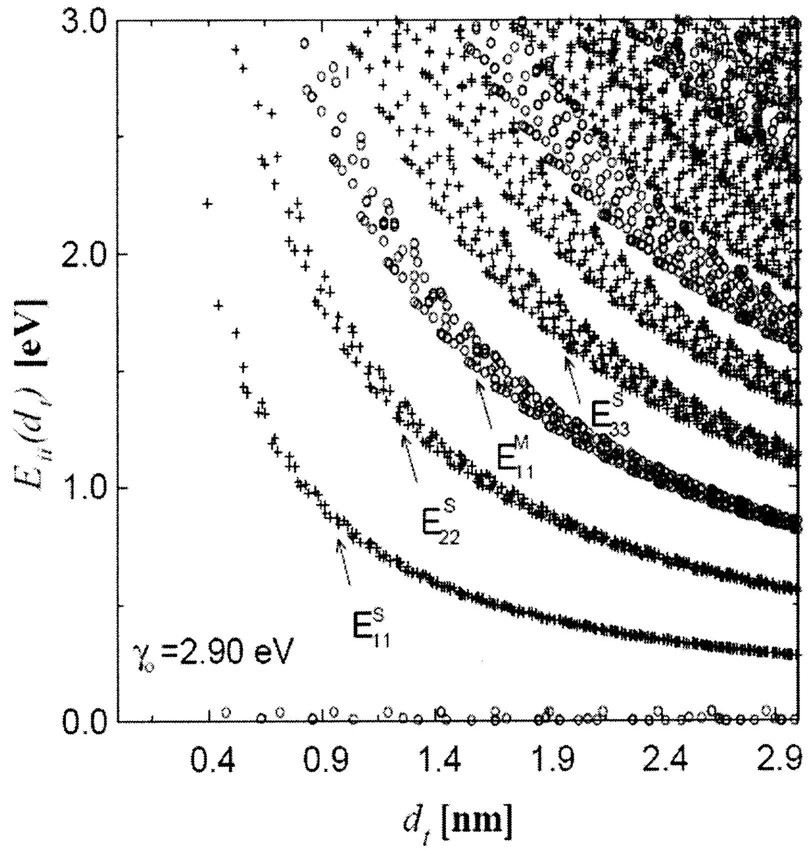

Figure 1.13 Calculated [70, 71] energy separations $E_{ii}(d_t)$ for all (n, m) values versus nanotube diameters. The results are based on the tight binding model of Equation 1.7, with γ_0 = 2.9 eV and nearest neighbor C-C distance a = 1.42Å. Semiconducting tubes are indicated by crosses and metallic tubes are indicated by open circles. The index i denotes the transition between the van Hove singularities, with i = 1 being closest to the Fermi level.

Kataura *et al.* [71] first introduced a plot of band gaps E_{ii} as a function of diameters d_t for all values of (n, m) carbon nanotubes, which is well known as the Kataura plot (Figure 1.13). E_{ii} is the energy separation between the mirror image spikes of singularities i in the 1-D electronic DOS. Each (n, m) nanotube has a unique set of E_{ii} transition energies. This plot is especially appreciated when used with diameter-dependent Resonant Raman Spectroscopy to determine the electronic properties and diameter of SWCNT. When the excitation laser energy matches with one of the electronic transitions $E_{ii}(d_t)$ between singularities in valence and conduction bands, it is resonantly absorbed by the nanotube. Nonlinear effect, such as Raman scattering is thereby, enhanced.

1.2.4 Applications of Single-wall Carbon Nanotubes

There are numerous possible applications for SWCNT because of their diverse electronic properties, chemical stability and predicted extreme mechanical strength. The most promising applications are described in this section.

First, a single-wall nanotube can be conducting or semiconducting, depending on its chiralities, as described in Section 1.2.3. It is possible to connect nanotubes with different chiralities thus creating nanotube hetero-junctions, which can form a variety of nanoscale molecular electronic device operations. Dekker and coworkers [72] reported on first field-effect transistor (FET) fabricated from an individual semiconducting single-wall carbon nanotube. The SWCNT positioned as a bridge between two platinum electrodes. The electrodes were deposited on top of a SiO_2 film grown on silicon wafer. In this configuration, the two Pt electrodes acted as the source and drain of the FET and the silicon wafer itself was used as the back gate. This nanoscale three-terminal switching device operated at room temperature. By applying a gate voltage, the nanotube could be switched from a conducting state to an insulating state. The problem with this nano-device was its large contact resistance [73] between the SWCNT and metal electrodes. In 2002, a research group in IBM [74] reported fabrication of "CNTFET" with improved interface contact, which is competitive to silicon MOSFET. More over, with complementary p- and n-type carbon nanotube FETs, they built the first integrated circuits with inter-molecular NOT gates (voltage inverters). However, a carbon nanotube based transistor may or may not work, depending on whether the selected nanotube is semiconducting or metallic. The electrical property of nanotube primarily depends on the dimensions (lengths, diameters and chiralities) of the tubes, over which the operator generally has no control. Besides, the quality of nanotubes that potentially can be used in nano-electronics should be defect-free or have controllable preferred defects, which currently has no accepted standard to evaluate. A reliable nano-transistor made of SWCNT has a long way to go.

Secondly, the thermoelectric power (TEP) of single-wall carbon nanotubes (SWCNT) is extremely sensitive to gas exposure history. Exposure to air or oxygen dramatically influences the nanotubes' electrical resistance, thermoelectric power, and local density of states [75]. Carbon nanotubes exposed to air or oxygen always has a positive TEP, suggestive of hole like carriers. However, at fixed temperature the TEP crosses zero and becomes progressively more negative as the SWCNT are stripped of oxygen. These results demonstrate that nanotubes could find use as sensitive chemical gas sensors. Kong *et al.* reported the first chemical sensor made of molecular wires of SWCNT [76] in 2000. With several seconds of exposure to gaseous molecules such as NO_2 or NH_3 at room temperature, the electrical resistance of an individual semiconducting SWCNT was found to dramatically increase or decrease by up to three orders of magnitude. Figure 1.14 shows the dramatic change of conductance upon exposure to different gases. The extreme oxygen sensitivity of carbon nanotubes was also demonstrated by Collins *et al.* [77] with SWCNT bundles and thin films consisting of random networks of SWCNT. As the surrounding medium was changed between vacuum and air, a rapid and reversible change of the nanotube resistance in a range of 10 % to 15

% was observed in step with the changing of environment. This reversible change of electrical conductivity is highly favorable because that it suggests a fabrication of miniature chemical sensor.

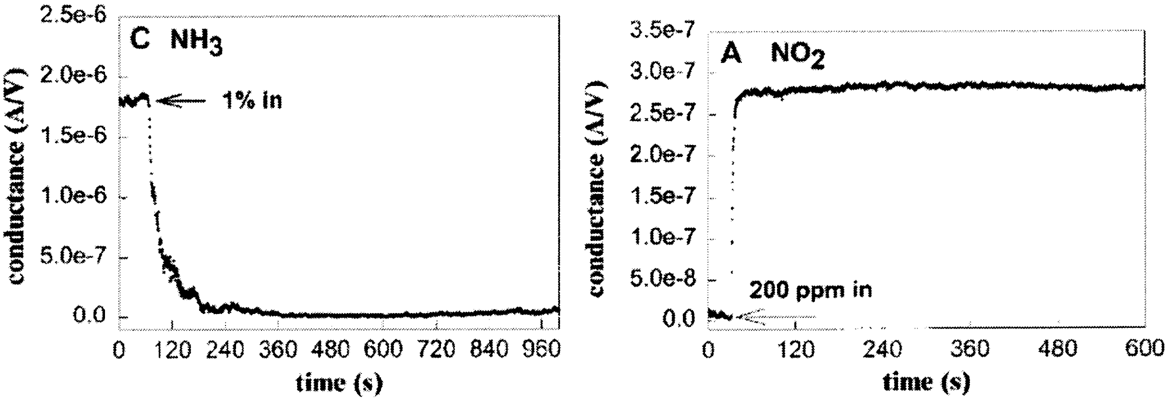

Figure 1.14 Electrical response of a semiconducting SWCNT to gas molecules of NH_3 (left) and NO_2 (right) [76].

Thirdly, the structure of carbon nanotubes features high aspect ratio and small radii of curvature at their tips, which are advantageous characteristics for electron field emission. With good electronic and mechanical properties, carbon nanotube is a promising candidate for developing a new generation of field emission displays or tips for scanning probe microscopic (SPM). In 1995, Rinzler *et al.* [78] demonstrated that laser heat induced electron field emission on individual multi-wall carbon nanotube and a far more intense emission (0.1-1 μA with bias voltage < 80 volts) at room temperature when the tip of the tube was open. Soon later, De Heer *et al.* [79] reported field emission from arrays of carefully aligned MWCNT obtained by drawing tube suspension through a ceramic filter. Their studies showed that an electric current could be drawn from a surface covered with nanotubes and points to the potential application of carbon nanotubes in flat panel display. Field emission is a robust characteristic of carbon nanotubes. It does not appear to be sensitive to the distribution of tube geometric or electronic properties [80]. Films of both multi-wall carbon nanotubes [79, 80, 81, 82] and single-wall nanotubes [83] were found to be excellent field-emitters. Carbon nanotubes used as emitters in field-emission displays (FEDs) can be either self-oriented arrays [76, 79] or randomly ranged networks [80, 81]. The latter property makes it possible to realize nanotube FEDs using printing method, which is particularly appreciated in fabrication of a large area and low cost panels.

Fourthly, since nanotubes are hollow, tubular, caged molecules, there have been proposals to use them as lightweight and large-surface-area packing material for gas-storage and hydrocarbon fuel storage devices. Hydrogen storage in carbon nanotubes was first reported by Dillon *et al.* [84] in 1997. They found that hydrogen tend to condense to high density in SWCNT. The authors claimed that carbon nanotubes could store 5-10 wt% of hydrogen at room temperature. In the following year's reports on the capability of SWCNT to adsorb hydrogen, a significant discrepancy was revealed. It was reported that lithium or potassium doped carbon nanotubes can absorb 14 or 20 wt % of hydrogen [85] at room to moderate-high temperatures (200-400 $^{\circ}$C) under ambient pressure. Another result published by Liu *et al.* [86] showed that a H_2 storage capacity of 4.2 wt % was achieved at room temperature and under a modestly high pressure (~ 10 MPa). About 78.3 % of adsorbed H_2 could be released at room temperature and ambient pressure. Recently, a much lower storage capacity of 0.43 wt % obtained from purified HiPco SWCNT at room temperature and up to 8 MPa was reported by a research group from Japan [87]. The discrepancy in these values may arise from a low bulk density of carbon nanotubes, the change in pressure caused by temperature fluctuations during measurement, and/or from differences in the mass, purity, and quality of the measured

SWCNT samples. Besides hydrogen storage, other possible usage of hollow tubular structures including gas or liquid filtration devices, nanoscale containers for molecular drug-delivery, as well as casting structures for making nano-wires and nano-capsulate were suggested.

Finally, carbon nanotubes exhibit very good elastic-mechanical properties because the two-dimensional arrangement of carbon atoms in the graphene sheet allows large out-of-plane distortions, while the strength of carbon-carbon in-plane bonds keeps the graphene sheet exceptionally strong against any in-plane distortion or fracture. These structural and material characteristics of nanotubes point towards their possible use in next generation of lightweight, yet highly elastic and strong composite materials. The following section will be dedicated to a discussion on carbon nanotube composites, especially composites involving polymers.

1.3 Carbon Nanotube–Polymer Composite Materials

Near-term practical applications of carbon nanotubes are expected to emerge from composite materials, as they do not require an accurate control of nanotube positioning and dimensions for device applications. Carbon nanotubes can be incorporated into structural materials, not only for mechanical reinforcement, but for altering electrical and thermal properties as well.

1.3.1 Mechanical Reinforcement

Single-wall carbon nanotubes are mechanically strong and resist fracture under extension, similarly to carbon fibers commonly used in aerospace applications. The strong in-plane graphitic C–C bonds make defect free SWCNT and MWCNT exceptionally strong and stiff against axial strains yet keep it flexible against non-axial strains. A single tube can be elongated by several percent before it fractures. In contrast to carbon fibers, however, carbon nanotubes are remarkably flexible. It can be twisted, flattened and bent into small circles or around sharp bends without breaking. Furthermore, severe distortions to the cross-section of SWCNT do not cause them to break. Another advantage of carbon nanotubes is their behavior under compression. Unlike carbon fibers, which fracture easily under compression, carbon nanotubes form kink-like ridges that can relax elastically when the stress is released.

In order to understand the fundamental strength and stiffness behavior of SWCNT, simulations employing tight-binding molecular dynamics methods and *ab-initio* density functional total energy calculations have been made. Promising values of 1TPa as Young's modulus and 5-10 % elastic limit of the strain before failure have been predicted. These values also predicted 50 GPa as the nanotube strength and intrigued extensive efforts to apply nanotubes as super strong reinforcing fibers. Macroscopic fibers and ribbons of oriented carbon nanotubes were reported by Vigolo *et al.*, which produced by assembly of SWCNT in the flow of a 5 % poly(vinyl alcohol) (PVA) solution [88]. Flow-induced alignment led to a preferential orientation of the nanotubes and formation of a ribbon. The Young's modulus varied between 9-15 GPa. By this coagulation-based carbon-nanotube spinning method, an improved composite structure [89] was fabricated one year later by the same group and the Young's modulus increased dramatically to 40 GPa and with a tensile strength of 230 MPa. Recently, a super-tough carbon nanotube fiber [90] was developed by Dalton *et al.*, which is reported to be tougher than any known natural and synthetic organic fibers. An improved coagulation-spin technique was involved. The resultant composite fibers were about 50 μm in diameter and contain around 60% SWCNT by weight. They had a tensile strength of 1.8 GPa.

1.3.2 Electrical Property Enhancement

Structures based on CNTs offer exciting possibilities for nanometer-scale electronic applications. Not only the carbon nanotubes may be used in composites to strengthen a structure, but also can enhance the electrical conductivity of the materials. Carbon nanotubes can be combined with a host polymer to tailor their electronic properties to specific applications. Since nanotubes are so small, they can be used in polymer composites and formed into specific shapes. In addition, they can be incorporated into a low-viscosity composite that can be sprayed onto a surface as a conducting paint or coating. For example, a major commercial product of carbon nanotube – polymer composite from Hyperion is used in the automotive industry to produce plastic parts that are sufficiently conductive to allow painting of these parts without first using a primer.

Composite materials based on single-wall carbon nanotubes and conductive (or conjugated) polymers have been an intensively investigated area. Conjugated polymers are polyunsaturated compounds that have a framework of alternating single and double carbon – carbon (sometimes carbon – nitrogen) bonds (Figure 1.15). Generally, all atoms in the backbone are *sp*- or sp^2-hybridized. Conjugated polymers naturally are either insulators or wide-gap semiconductors, and some of them turn into metallic type conductors only after a process called doping, in which the charge carriers are induced. Polymers such as polypyrrole (PPy) can be partially oxidized to produce p-doped materials by controlled addition of an acceptor or *p*-doping agent such as AsF_5, Br_2, I_2, or $HClO_4$. But dopants such as iodine make the material extremely reactive with oxygen so the polymer becomes very unstable.

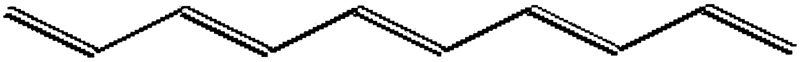

Figure 1.15 Molecular conformation of conjugated polymers.

Single-wall carbon nanotube represents another form of conjugated carbon system [91], which consists of one sheet of graphene wrapped around in concentric cylinders. An individual nanotube may be metallic or semiconducting. But in bulk, they form a pseudo-metal with conductivity [92] of approximately 10^5 S/m. By controlled doping of SWCNT into the polymers, the conductivity of this composite can be modified over many orders of magnitude. Because the nanotubes interact with the polymer by van der Waals interactions so there is no decrease in stability in the composite. As a hard, conductive plastic this composite shows great potential as an antistatic coating or as electromagnetic shielding for electronic devices.

Theoretically, the chemical structures of conjugated polymers are represented by alternating single and double bonds. But the key feature is that the extended π-bond electron system is delocalized over the entire molecule. For this reason, polyaniline (PAn) and poly(*N*-vinylcarbazole) (PVK) are also considered to be conjugated polymers [93]. The lone pair electrons on the nitrogen atom can be ionized relatively easily, and with the nitrogen p_z orbital assisting the delocalization of the π-electrons, the PVK possesses the minimum molecular structure required for stabilizing a charged species [94]. On the other hand, the steric repulsion requires that the large planar carbazole units be arranged normal to the backbone axis. So the materials may take up a helical conformation in which successive aromatic side chains are overlapped to each other in a stack. Along this $\pi - \pi$ stack, charge carriers can transport with relatively low activation energy.

The conjugated polymer-SWCNT composite represents an alternative class of organic semiconducting material that is promising for organic photovoltaic cells with improved performance. High open-circuit voltage photovoltaic device [95] from carbon-nanotube – polymer composites was fabricated by Kymakis *et al.* The composite layer was formed by solution casting or spin coating of a chloroform solution of 1 wt % of nanotubes in polythiophenes. They found that the open circuit voltage of the device was larger than theoretically calculated limit. This photovoltaic response was explained based on the introduction of internal polymer – nanotube junctions within the polymer matrix. A photoinduced electron transfer from the polymer to nanotube contributed to the enhancement of charge separation and collection.

1.3.3 Surface Modification of Carbon Nanotubes

Successful applications of such composite systems, no matter for mechanical or electrical purposes, require well-dispersed nanotubes with good adhesion with the host matrix. In the past, composites films were made by drop casting or spin coating [96, 97] of a mixture of carbon nanotubes with polymer in an organic solution. However, intrinsic van der Walls attraction among tubes, in combination with their high surface area and high aspect ratio, often leads to significant agglomeration. Besides, smooth carbon nanotube sidewalls are incompatible with most organic solvents and polymers, which result in poor dispersion of nanotubes in the polymer matrix. This inherently weak nanotube-polymer interaction results in poor interfacial adhesion, which may lead to further nanotubes aggregation within the matrix. Generally, dispersing the SWCNT in a polymer solution involves a lengthy sonication (up to 48 hours). However, this lengthy sonication may damage or even cut the SWCNT, which is undesirable for many applications. Following is a brief introduction to several technique developed recent years to improve the dispersibility of single-wall carbon nanotubes in organic solvents and versatile polymers.

1.3.3.1 Covalent Functionalization. By covalently attaching alkanes to their sidewalls, single-wall carbon nanotubes have been made soluble [98] in various organic solvents, such as chloroform, methylene chloride and tetrahydrofuran. To achieve this point, the sidewall of nanotubes has to be fluorinated by the technique developed in the fluorination of graphite [99]. Although the IR spectrum of the resultant materials identified the existence of C – F stretching, TEM showed that the fluorination process did change the structure of the nanotube sidewalls and higher reaction temperature tends to destroy the tubular structure eventually. Carboxylic acid group [100] is also widely used to covalently bond molecules to nanotubes. This carboxyl functionality (SWCNT–COOH) can be easily formed at the opening ends and sidewall defects of nanotubes by oxidizing treatments, such as sonication in sulfuric and nitric acid or refluxing in nitric acid.

But extensive studies demonstrate that covalent functionalization of the sidewall of carbon nanotubes disturbs the extended π-electron systems, convert sp^2 orbital on the nanotube surface to sp^3 structure. This modification is at the cost of losing conjugation that is responsible for many attractive attributes of carbon nanotubes.

1.3.3.2 Non-covalently Functionalized Soluble SWCNT. By non-covalently wrapping single-wall carbon nanotubes with linear polymers [101], Smalley's group first obtained individually water soluble SWCNT. They reported that carbon nanotubes had been solubilized in water by non-covalently associating them with linear polymers, most successfully with polyvinyl pyrrolidone (PVP) and polystyrene sulfonate (PSS). The tight uniform association of the polymers with the sidewalls of the nanotubes disrupts both the hydrophobic interface with water and the smooth inter-tube interactions leading to aggregates. Figure 1.16 schematically shows the possible wrapping situations of polymeric molecules on SWCNT. In their experiments, purified SWCNT were dispersed in 1% water solution of sodium dodecyl sulfate (SDS) that was a surfactant. The concentration of SWCNT was 50 mg/l. After sufficient sonication to ensure a good initial disperse, 1 wt % polyvinyl pyrrolidone (PVP) was added. After incubation 12 hours at 50 °C and consequent procedure to remove extra surfactant and polymer, a stable solution of PVP wrapped SWCNT in water was obtained with a uniform disperse up to 1.4 g/l.

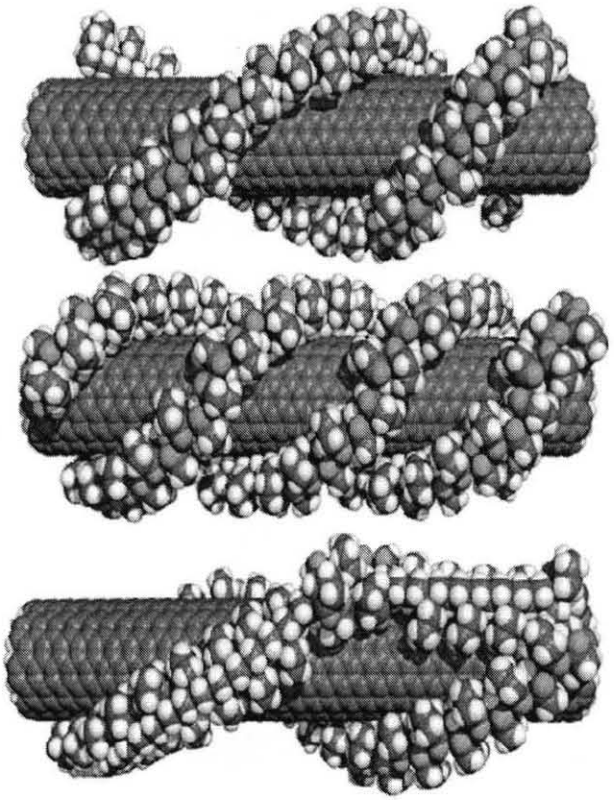

Figure 1.16 Schematic polymer wrapping geometries [101]: (top) double helical wrapping, (middle) triple helical wrapping allowing higher surface-area coverage with the same polymer backbone curvature, and (bottom) possible internal-rotation induced switchback allowing multiple strands to come from the same polymer chain.

At the almost the same time, Dai *et al.* [102] developed another technique to non-covalently functionalize and subsequent immobilize various biological molecules onto the nanotubes. The strategy involves attachment of small molecules featured by a pyrene group at one end and a biocompatible reactive group on the other end. By π-stacking effect between the conjugation structures of nanotube sidewalls and pyrene moieties, the functional molecules could be anchored on SWCNT with a high stability. A schematic diagram for the non-covalent functionalization effects is shown in Figure 1.17. With customized functional molecular groups on the other end and dangling on the sidewall of nanotubes, a wide range of biomolecules could be trapped on the tubes efficiently.

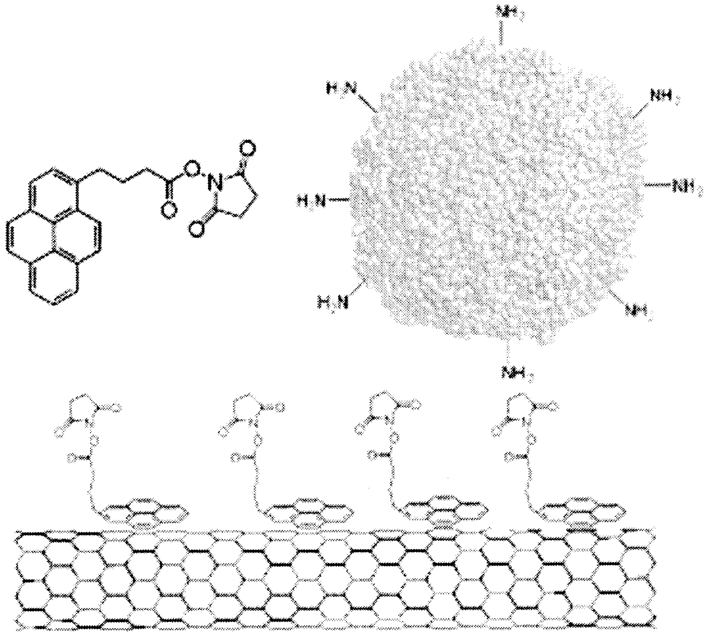

Figure 1.17 Scheme for non-covalent functionalization of the sidewalls of carbon nanotubes for protein immobilization [102].

Another group from Zyvex Corporation reported a new non-wrapping approach [103] to non-covalently modify of carbon nanotube surfaces by short, rigid functional conjugated polymers, poly(aryleneethynylene)s, instead of small molecules. Their technique not only enables the dissolution of various types of carbon nanotubes in organic solvents, which represents the first example of solubilization of carbon nanotubes via π-stacking without polymer wrapping, but could also introduce numerous neutral and ionic functional groups onto the carbon nanotube surfaces.

1.3.3.3 *in situ* Polymerization with Presence of SWCNT. Instead of modification of the sidewall of SWCNT, Park, *et al.* [104] reported a process to effectively disperse SWCNT bundles in an aromatic polymer by *in situ* polymerization of the monomers in the presence of sonication during the polymerization process. In this study, aromatic polyimide was used as a continuous medium to prepare SWCNT reinforced polyimide nanocomposites. The SWCNT were first dispersed into solvent DMF in an ultrasonic bath. Then selected diamine (APB) and dianhydride (6FDA) were added into the solution with continuous stir. The solution polymerizing reaction was carried out with SWCNT presence in the flask immersed in an ultrasonic bath (40 kHz). Optical microscope and transmission electron microscopy were used to examine the polymerized sample and identified that thin SWCNT bundles were dispersed uniformly throughout the whole polymer matrix. The bundle thickness was reduced compared with pristine SWCNT. It was suggested that the degree of dispersion of the SWCNT in polymer matrix was largely influenced by their state of dispersion in the solvent. The highly aromatic monomers in the solvent can favorably interact with the graphene surface of the nanotube via p – p overlapping interaction and consequently stabilize the solution. But Maser *et al.* showed conflicted results when they tried to fabricate PANI–NT composites [105] with "*in situ*" polymerization process. Although the genuine PANI–MWCNT composite materials was synthesized by the electronic interactions between nanotubes and the quinoid rings of the polymer, they found that it's more difficult to form a true PANI–

SWCNT composite. They attribute the difficulty to the complex structure of SWCNT itself, i.e. to the presence of entangled bundles of tubes, amorphous carbon and even catalytic metal particles, which prevent a homogeneous dispersion of the nanotubes in the polymer matrix. This report concluded that in order to obtain a true SWCNT composite, the dispersion of the SWCNT has to be drastically improved.

Besides the thermally initiated and photoinitiated polymerization, electrochemical synthesis of polymer films over carbon nanotubes represents another promising technique to fabricate polymer–SWCNT composites. Typical conducting polymers like polypyrrole (PPy), polyaniline (PANI) and polythiophene (PTH) can be prepared either chemically or electrochemically. Ren *et al.* reported that Ppy films were uniformly electro-polymerized over individual carbon nanotubes in a well-aligned nanotube array [106]. The polymer films were synthesized potentiodynamically using a standard three-electrode cell. Because of the high electrical conductivity of the carbon nanotubes, each tube acts as an electrode and the polymerization will evenly performed on all nanotubes.

1.3.4 Chemical Doping of Carbon Nanotubes

To the modern microelectronics, it is widely known that obtaining both p- and n-type materials and controlling their charge carrier densities are crucial. Energy band engineering by doping has played a critical role. Carbon nanotubes are a new class of material potentially useful as key elements for future miniaturized electronics. Similar to ideas in conventional materials, designed doping of nanotubes is expected to yield nanoscale devices with interesting properties and functions. Single-wall carbon nanotubes are typically chemically inert. Covalent attachment of molecular species to fully sp^2-bonded carbon atoms on the nanotube sidewalls proves to be difficult. Adsorbing molecules to nanotubes via non-covalent forces, however, turns out to be easy because of their size, large surface area, and hollow geometry. Chemical adsorption has important consequences to their physical properties and potential applications.

When fabricate and characterize single-molecule field-effect transistor from an individual semiconducting carbon nanotube, it was found that the SWCNT with two metal contacts exhibits p-type transistor characteristics [107, 108, 109]. With holes as majority carriers, the conductance of the SWCNT was observed to decrease by three orders of magnitude under positive gate voltages. But after Dai's innovative realization [76] of chemical sensors based on individual single-wall carbon nanotubes (SWCNT) which was capable of detecting small concentrations of toxic gas molecules, like NO_2 and NH_3, Collins *et al.* first questioned the interdependence of ambient gas adsorption and electrical quantum conductance in carbon nanotubes [75, 77]. They argued that many supposedly intrinsic electronic properties measured on as-prepared nanotubes might be severely compromised by extrinsic air exposure effects. Now it was established that molecular oxygen adsorbed on the nanotubes was responsible for the p-type hole-doped as-grown SWCNT. Adsorption of molecules known as strong oxidizer, like O_2 and NO_2, will cause electrons transfer from nanotubes to the extrinsic molecules. On the other hand, adsorbed molecules known as electron-donors, like NH_3 and amines, can donate negative charges to the nanotubes and convert carbon nanotubes from p-type to n-type.

Based on above discovery, Dai *et al.* introduced a new concept [110] of n-doping of carbon nanotubes by functionalization of SWCNT sidewalls with amine-rich polymers PEI (polyethylenimine). The resulted n-type FETs based on individual nanotube wires were stable in air.

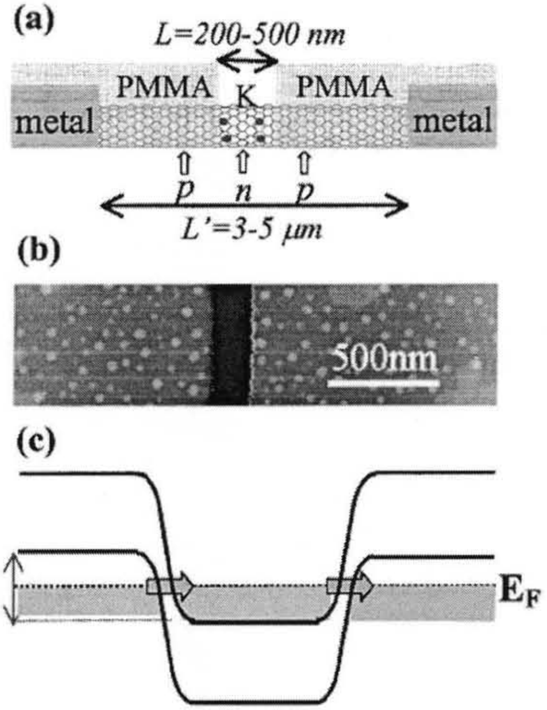

Figure 1.18 Single-wall carbon nanotube device with p-n-p junction. (a) Schematic design of p-n-p nanotube device. (b) AFM image showing a 200 nm wide window (dark trench in the middle) opened in the PMMA layer over a nanotube (not visible). (c) Band diagram. Electrons can tunnel through the double p-n junctions when the Fermi level (*EF*) is between the arrowed regions [112].

Another classic approach to n-type electron-rich carbon nanotubes is via chemical doping with alkali metals. Indeed, potassium (K) doping has led to n-type SWCNT FETs and enabled more complex devices such as intra-tube p-n junction [111] and p-n-p junction (Figure 1.18) [112]. However, alkali dopants suffered from immediate degradation upon exposure to air, making them undesirable for n-doping of SWCNT in practical device applications. Nondegenerate intra-tube p-n junctions have been formed by organic amine doping, leading to excellent intra-tube electrical rectifiers [113].

CHAPTER 2

EXPERIMENTAL METHODOLOGY

This chapter introduces experimental techniques for material synthesis, sample preparation and characterization involved in this project. The workflow of entire experimental procedure is shown in Figure 2.1.

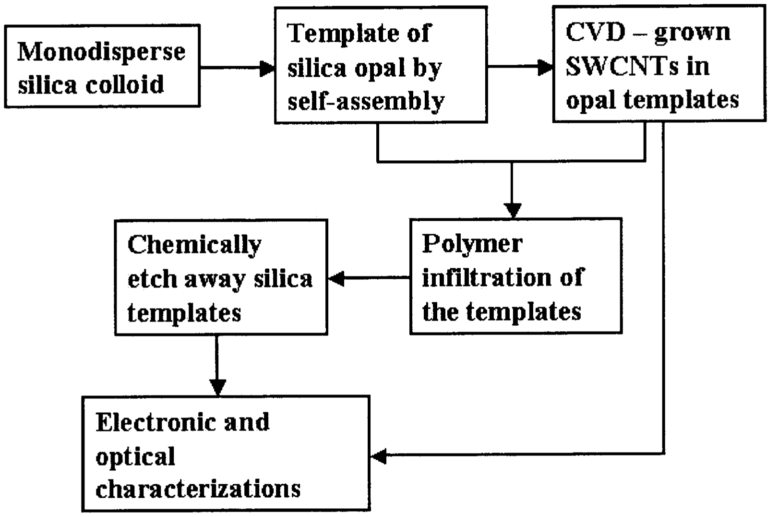

Figure 2.1 Diagram of experimental workflow.

The basis for nanostructured composite was a 3-D template made of silica opaline structure. This structure was made in several steps. First, highly monodisperse silica submicron spheres were synthesized in a alcosol by sol-gel process. Then, silica opal template was produced by colloid self-assembly. Chemical vapor deposition was used to grow single-wall carbon nanotubes (SWCNT) in the voids of silica templates. The templates of bare silica opal or opal–SWCNT were then infiltrated with various polymers. The silica template was then removed by selective etching and left 3-D ordered and interconnected air channels, which were later embedded in polymer or polymer–

SWCNT composite. Finally, electric and optical properties of these photonic crystal structures were characterized by various experimental techniques.

2.1 Synthetic Silica Opal

2.1.1 Synthesis of Monodisperse Silica Colloid

The synthesis of submicron silica particles has been extensively studied. Monodisperse SiO_2 nanospheres have been synthesized following a well-known Stöber-Fink-Bohn [114] method. It consists of a sol-gel process in which a Si metallo-organic compound (sol) hydrolyses in water and condenses into a solid network (gel).

The silicon compound usually used is tetramethoxysilane (TMOS) or tetraethoxysilane (TEOS). In the first stage of reaction, silicon compound hydrolyses in water, when alkoxy groups (-OR) are replaced by hydroxyl groups (-OH).

$$(RO)_n\text{Si-}(OR)_m + mH_2O \longrightarrow (RO)_n\text{Si-}(OH)_m + mROH \qquad (2.1\text{ a})$$

where $0 \le n \le 4$ and $0 \le m \le 4$ and $n + m = 4$. R represents the alkyl group $-CH_3$ or $-C_2H_5$. In the following stage of reaction, condensation occurs between remaining alkoxy group and newly produced hydroxyl group, or two hydroxyl groups, leading to the formation of Si–O–Si chains and growth of solid amorphous silica particles.

$$\equiv\text{Si-OR} + \text{HO-Si}\equiv \longrightarrow \equiv\text{Si-O-Si}\equiv + \text{ROH} \qquad (2.1\text{ b})$$

$$\equiv\text{Si-OH} + \text{HO-Si}\equiv \longrightarrow \equiv\text{Si-O-Si}\equiv + H_2O \qquad (2.1\text{ c})$$

In the condensation procedure, ammonium hydroxide ($NH_3{\cdot}H_2O$) usually used as catalyst. With appropriate reaction conditions, such as temperature and concentration of different reactants, well-shaped spherical microparticles with narrow size distribution can be synthesized [115, 116].

In this research work, tetraethoxysilane (TEOS) has been used because of its harmless by-product, ethanol, from the hydrolysis reaction. The reaction was conducted at controlled room temperature of 25 °C for 24 hours with a constant magnetic stir. By strictly control of the reaction parameters, such as concentration of different reactants, monodisperse silica spheres with different diameter were produced. The resultant silica alcosols were then purified by repeated cycles (typically four cycles) of centrifugation, separation and ultrasonic re-dispersion in pure ethanol, in order to remove the impurities, such as unreacted ammonia and water.

2.1.2 Measuring the Size of Colloidal Silica Particles

The quality of the self-assembled opaline structure crucially depends on the monodispersity of the starting colloidal silica particles. A Coulter N4 Plus instrument has been used to characterize the monodispersity of silica spheres in the suspension. This measurement is based on Photon Correlation Spectroscopy (PCS) technique, which is also referred to as laser Dynamic Light Scattering (DLS) or Quasi-elastic Light Scattering. This method can be used to estimate the size and size distribution of sub-micron particles in a liquid suspension, which are in a state of random Brownian motion. The speed of a particle moving through a fluid depends on temperature and viscosity of the fluid and particle size. The particle size can be determined once the temperature and viscosity is specified, for example, by measuring the diffusion rate of particles. The smaller the particles are, the faster they move. The rate of the motion can be detected by analyzing the time-dependent light intensity scattered from the particles when they are illuminated by a laser beam. Figure 2.2 shows a functional block diagram of the equipment using the PCS technique. Fiber-optic receptors, stepper motor and Photo Multiplier Tube (PMT) define the angle of scattered-light detection.

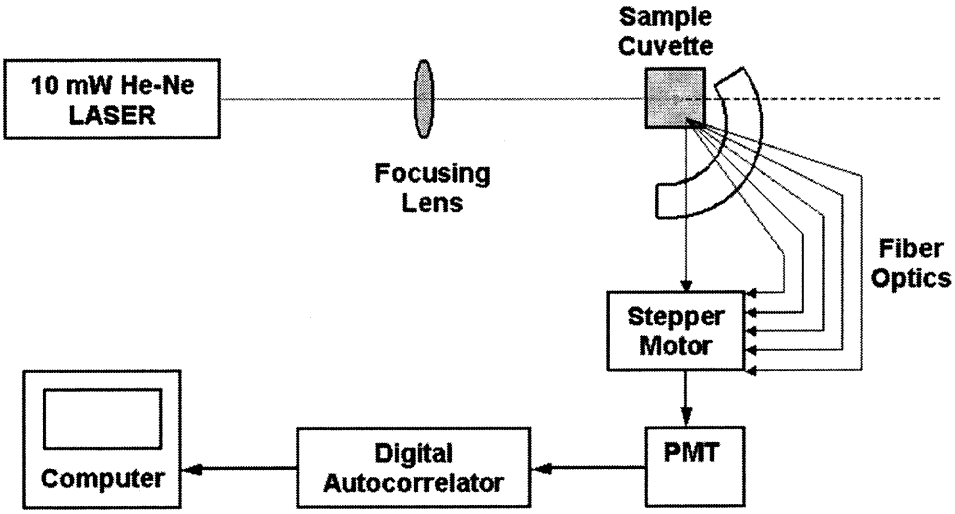

Figure 2.2 Schematic diagram of the N4 Plus built on Photon Correlation Spectroscopy technique.

By Unimodal Data Analysis provided by N4 Plus, mean size (D), polydispersity index (PI) of the silica spheres dispersed in ethanol solution can be automatically calculated. The Unimodal analysis is an accurate method for size distributions that are not extremely polydisperse. It is perfect for measuring the size for monodisperse colloidal particles. To calculate the standard deviation (SD) and relative standard deviation (RSD) of the particle size, following functional relationships based on the Unimodal data analysis can be used:

$$RSD = \frac{SD}{D} = \frac{1}{\sqrt{\frac{1}{2 \times PI} + 4}}. \tag{2.2}$$

Here D is the average diameter of the sample and PI is the polydispersity index of the suspension.

2.1.3 Fabrication of Synthetic Silica Opal

A popular method to fabricate colloidal crystals is gravitational sedimentation. It is simple and straightforward: a colloidal suspension is left to settle under natural gravitational forces for several weeks. The sedimentation time depends on particle size [117]. There are difficulties though when dealing with small or large silica spheres. If the silica spheres are small (less than 200 nm of diameter), thermal fluctuations may compete with gravitational forces and prevent sedimentation. If the silica spheres are too large (larger than 500 nm of diameter), their sedimentation velocity is too fast to obtain an ordered array. When gravitational energy is larger than the thermal energy, the sedimentation process occurs at conditions far from equilibrium and results in non-crystalline sediment [118]. An improved sedimentation technique was introduced by Lopez's group [119] as Electrophoretic Aided Sedimentation. The effective weight of silica spheres suspended in a liquid can be reduced (or increased) by applying an electric field in a counter (or along) direction of the gravitational field. By means of this method, they were able to fabricate the first opals made of silica spheres with diameters as large as 870 nm.

Another intensively studied and most currently used technique is capillary forces driven self-assembly. This method, which is similar to the Langmuir-Blodgett methods for film deposition, was first reported by Nagayama [120] *et al.* for deposition of a 2-D (monolayer) fine particles array on flat surfaces. The sample is immersed vertically in the suspension. Solvent evaporation results in colloidal suspension slowly sweeping across the flat surface, leaving a layer of self-assembled particles on that surface. For a successful deposition, the solvent evaporation must compete with gravitational sedimentation of particles. For silica sphere with larger diameters (> 400 nm), Norris [22] *et al.* suggested to add a convective flow to the suspension to minimize sedimentation and provide a continuous flow of particles toward the meniscus region.

In this research project, a convective self-assembly was used with experimental configuration shown as in Figure 2.3. A thoroughly cleaned glass or quartz slide was immersed vertically or slightly inclined into purified silica alcosol contained in a glass scintillation vial. Strong capillary forces at the meniscus line between the substrate surface and suspension induced crystallization of silica spheres into an ordered array. The thickness of crystalline film could be tuned by changing the concentration of the silica alcosol [121]. Typically, 1 wt % suspension was used during this project. A temperature gradient of 75 °C to 60 °C across the vial was used to provide a convective flow for deposition of silica spheres larger than 400 nm.

In order to improve the mechanical stability of the artificial silica opal, 800 °C temperature sintering [122] was introduced after the opal film deposition.

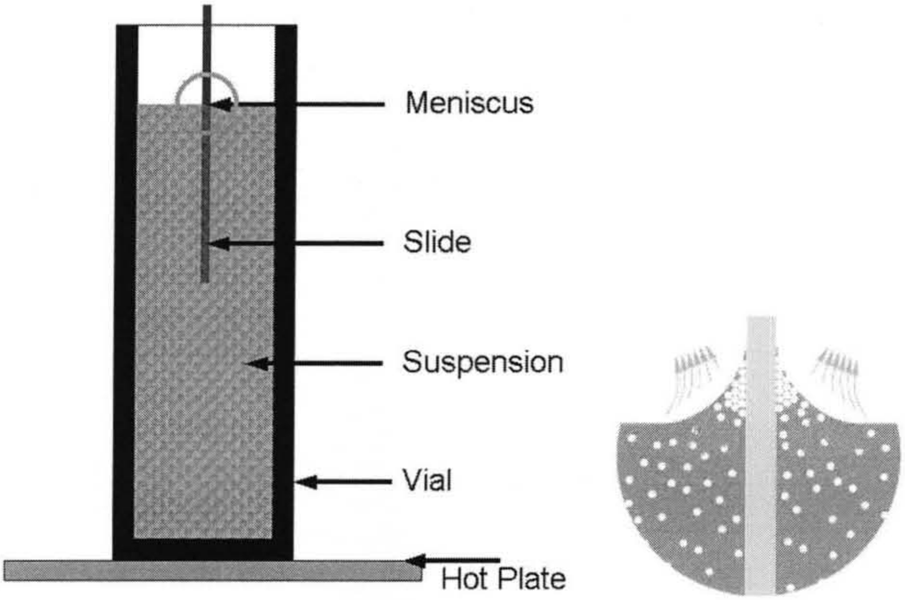

Figure 2.3 Schematic experiment setup for synthetic silica opal deposition (left) and an enlarged view of the meniscus area (right).

2.2 Growth of Single-wall Carbon Nanotube by CVD

In this research project, single-wall carbon nanotubes have been grown by chemical vapor deposition with carbon monoxide as feeding stock, and single transition metal cobalt (Co) as catalyst. Silica opal template, deposited on silicon or quartz substrate, were immersed into $Co(NO_3)_2 \cdot 6H_2O$ ethanol solution of various concentration overnight. The templates soaked with the catalyst solution were then dried at 70 °C in air for 30 minutes. The cobalt nitrate adsorbed in the opaline template could be accurately measured.

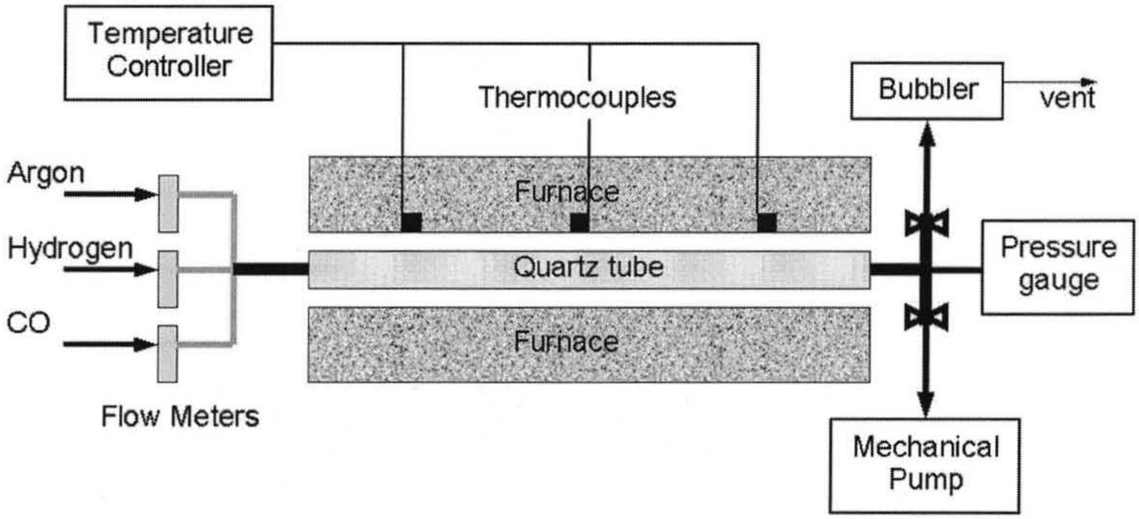

Figure 2.4 Schematic setup of atmosphere Chemical Vapor Deposition.

Chemical Vapor Deposition process was conducted in a quartz tube reactor placed in a horizontal tubular furnace that is shown in Figure 2.4. First the sample has undergone through 30 minutes calcinations in air at 500 °C in order to break down the cobalt nitrate into the corresponding cobalt oxide. Pure hydrogen flushed into the vacuumed tube for another 30 minutes at 760 torr (1 atm) and 500 °C to reduce the cobalt oxide to sub-oxides and metal particles. The temperature at the reaction zone was then raised to 750 °C, following with introduction of pure carbon monoxide at a flow rate of 200 cm^3/min

into the tube. The reaction pressure of CO was maintained at 1 atm when the reactor tube was open to the atmosphere through an exhaust system. The exhaust was administered through a fume hood and monitored by CO detector. Generally, the reaction lasted 30-60 minutes. After completion of the reaction, the reactor was allowed to cool down at argon flow (80 cm^3/min) to reach room temperature.

2.3 Fabrication of Nanostructured Polymer–SWCNT Composites

Polymeric inverse opal has been made by infiltrating the silica opal template by polymers and selective etch away the template by HF acid. When single-wall carbon nanotubes present in the template, the resultant inverse opaline structure is made of polymer-carbon nanotube composites.

To infiltrate the silica opal template, polymer can be introduced directly as a polymeric solution. However, there are several disadvantages to this method: First, the evaporation of solvent may lead to volume shrinkage and incomplete filling inside the template; Second, high molecular weight molecules may block the voids in opaline template; Moreover, when carbon nanotubes present in the template, there may not be a good interface formed between the polymer and nanotube. An alternative way is to infiltrate the template with liquid monomer, then conduct *in situ* polymerization. The advantage is not only obtaining a higher filling percentage, the *in situ* polymerization may also improve the interface between polymer and nanotubes (refer to Section 1.3.3.3).

A wide variety of polymers can be obtained by either photoinitiated or thermally initiated bulk polymerization from proper monomers. A typical procedure involved in this research project to fabricate polymer or polymer-SWCNT composites inverse opal by *in situ* polymerization is briefly described here. Template of synthetic silica opal, with or without embedded carbon nanotubes, was binding with cover glass and hung in a glass scintillation vial containing the desired monomer and if necessary, catalyst. The cover glass can prevent excessive polymer formation on the top surface of template. With the lower end of the sample merged in the chemicals, the capillary force drove the solution up and through the entire sample. Voids between silica spheres would be filled by the liquid precursor. After completion of the polymerization, the sample was removed from the vial. 10 % HF was used to etch away all of the glass, including silica opal, leaving CNT imbedded in free standing polymer inverse opaline structure. A schematic setup of the polymerization reaction cell is shown in Figure 2.5. Both of polymer-SWCNT composites and blank polymer films were produced in this way.

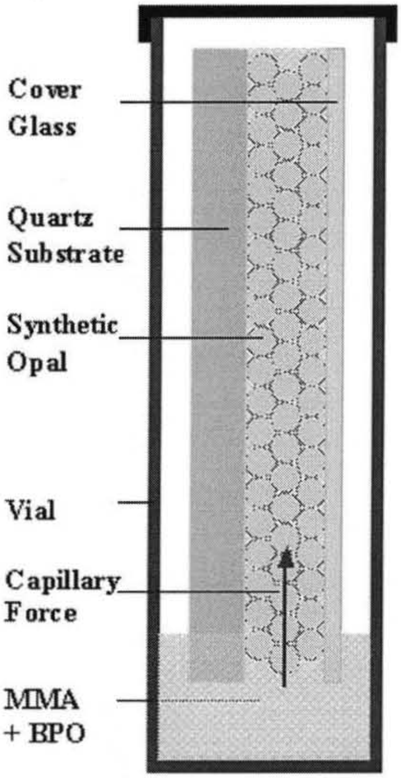

Figure 2.5 Schematic setup of a chemical reaction cell for polymer infiltration.

2.3.1 Poly(methyl methacrylate)

Poly(methyl methacrylate) (PMMA) was selected to make inverse opaline structure because of its chemical stability to acid and its optical transparency. The precursor for PMMA was methyl methacrylate (MMA) with 5 wt % catalyst benzoyl peroxide (BPO). Methyl methacrylate and benzoyl peroxide were both provide by Polysciences and used as is. The catalyst is soluble in MMA. The polymerization process was initiated thermally. Desired reaction condition was 70 °C for 3 hours. The inhibitor in MMA monomer was not removed before the *in situ* polymerization. Each experiment required only a small amount of MMA and large amount of the monomer is not suitable for storage without the inhibitor. On the other hand, effects of inhibitor can be eliminated by higher temperature and large amounts of initiator. The molecular structure of the *in situ* polymerized PMMA was identified with a Galaxy Series FT-IR spectrometer and compared to standard PMMA spectrum.

2.3.2 Poly(N-vinylcarbazole) Compound

Photoconductive polymer Poly(N-vinylcarbazole (PVK) was used in this project as well. PVK and SWCNT composite is an intriguing structure because of its electronic aspects. The addition of "inactive" molecules of *N*-ethylcarbazole (ECz) and 4-(Diethylamino)benzaldehyde diphenylhydrazone (DEH), which improves the photoconductance of the polymer complicates the polymerization of PVK.

Poly(*N*-vinylcarbazole) has high photoconductive efficiencies although it does not have the conventional conjugated backbone structure featured with alternating single and double bonds. Because of the electron rich pyrrole moieties in PVK molecules, it can be doped with electron acceptors, such as C_{60} and carbon nanotubes, to prompt its photoconductivity. In this way, D – A junctions are created between the polymer (D) and the electron acceptor (A), allowing preferential transfer of the electrons into electron acceptor while leaving the holes to be transported through the polymer. This is a process known as photoinduced charge transfer. Consequently, high-performance photovoltaic response can be achieved.

PVK has a high glass transition temperature (Tg) of 210 °C. One of the advantages of lowering its glass transition temperature is to make the otherwise brittle polymer easy to handle at room temperature, especially when fabricating a free-standing film with inverse opaline structure. The optic-electronic effect of PVK-based photoconductive polymer composites can also be enhanced by lowering its glass transition temperature. This enhancement is due to an improvement in the orientation mobility of the nonlinear optical molecules of PVK [123]. Lower glass transition temperature can be achieved effectively by incorporating proper amounts of plasticizer, N-ethylcarbazole (ECz) [124]. Phase separation, which has been observed in the compound, sets an upper limit on the ECz concentration. ECz has similar molecular structure with PVK and its monomer N-vinylcarbazole (VCz). It can be dissolved in tetrahydrofuran (THF) solution of PVK as a dopant. It can also be mixed with a monomer of VCz and take effects in the afterwards polymerized PVK. VCz and ECz are both crystal powers at room temperature and have a very close melting temperature, 65-70 °C for VCz and 68-70 °C for ECz.

The dopant DEH works as a photosensitizer, which enhance the absorption of the mixture in UV to visible region if added into photoconducting polymer complex of PVK. Also as a hole-transport agent, DEH can form connected pathways for the hopping motion of holes in photoconducting polymers [125]. Holes generated by illumination of the PVK-DEH charge transfer complex will be transported by hopping among neighboring carbazole units.

To incorporate PVK-ECz compound into a nanostructured composite, a VCz and ECz mixture with 5:1 weight ratio were infiltrated into opal template at 70 °C. UV-induced *in situ* polymerization was conducted at the same temperature. A Sylvania 100W mercury spot lamp provided 320-400 nm ultra-violet radiations to initiate the polymerization process. The UV intensity is around 12.5 mW/cm^2. No photo initiator, such as 2,2-dimethoxy-2-phenylacetophenone (DMPA), was used because it was reported that monomer VCz can be excited by 355 nm UV light and form free radicals [126] at room temperature. On the other hand, it was found that the presence of plasticizer molecules significantly slows down the polymerization compared to the reaction without ECz. This retardation can be explained by the diluted concentration of radicals in the reaction system by addition of inactive molecules of ECz. Moreover, the polymerization of vinylcarbazole was retarded even further in the presence of carbon nanotubes. This can be explained by a decreased mobility of the aromatic carbazole resulting from $\pi-\pi$ overlap interactions with the SWCNT surfaces. The quality of *in situ* polymerized PVK was evaluated with UV absorption spectrum.

Tetrahydrofuran solution of a PVK-ECz-DEH compound with weight ratio of (5:1:1) was used to infiltrate the opal template in order to incorporate the polymeric compound. Although DEH powder has a good solubility in melted VCz, the addition of DEH, in small amount as 1 wt% of VCz, has been found totally preventing the polymerization. The reason is that the large molecule of DEH, which consists of three aromatic rings of aniline derivatives [Figure 2.6 (d)], exerted significant mobility restriction to the activated radical and finally terminates the chemical reaction.

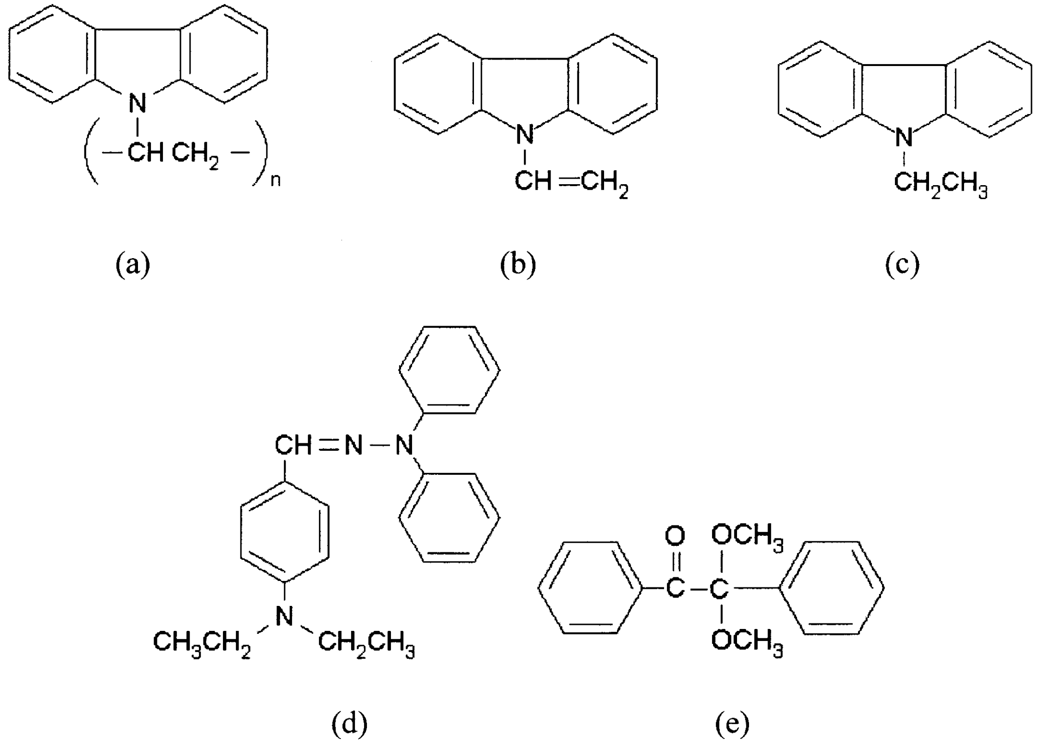

Figure 2.6 molecular structures of chemicals involved in PVK–SWCNT composite. (a) Poly(N-vinylcarbazole) (PVK), (b) N-vinylcarbazole (VCZ), (c) N-ethylcarbazole (ECZ), (d) 4-(Diethylamino)benzaldehyde diphenylhydrazone (DEH), (e) 2,2-Dimethoxy-2-phenyl-acetophenone (DMPA).

The N-vinylcarbazole, N-ethylcarbazole and Poly(N-vinylcarbazole) were provided by Polysciences Inc. 4-(Diethylamino)benzaldehyde diphenylhydrazone was from Mackenzie Co. Figure 2.6 shows the chemical structure of components involved in the process.

2.4 Characterization of Nanostructured Composites

2.4.1 Scanning Electron Microscopy/Energy Dispersive X-ray Spectroscopy

A commercial LEO 1530 VP FE-SEM was used to identify the topological structure of the materials. In a typical setup of SEM, a beam of high-energy electrons is generated in an electron gun and attracted by an anode. This beam travels downward through a series of condenser lens and is focused to a very fine spot by an objective lens. Near the bottom, a set of coils scans the focused beam across the specimen. As the energetic electron beam strikes the sample, various reactions can occur, as shown in Figure 2.7. The signals most commonly used to characterize the sample are the secondary electrons, the backscattered electrons and X-rays.

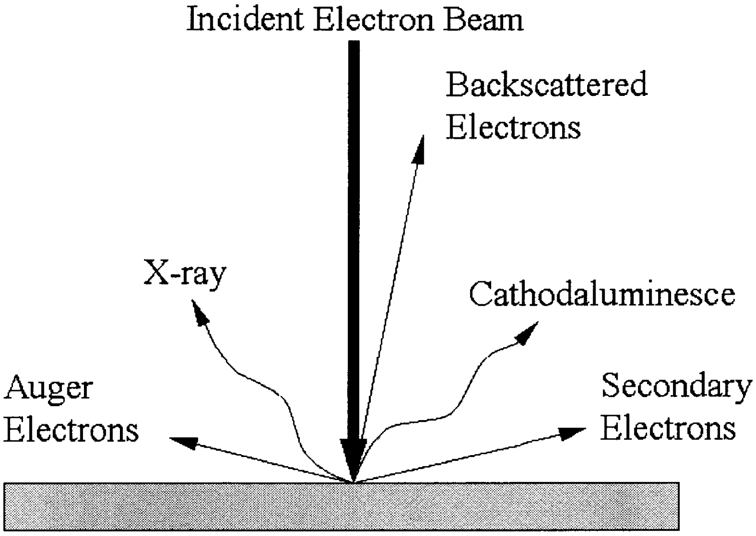

Figure 2.7 Schematic diagram of interaction between incident electron beam and samples in Scanning Electron Microscopy [127].

Electrons in the tightly focused beam may be scattered directly off the sample, which is backscattered electrons, or cause secondary electrons to be emitted from the surface of the sample. Secondary electrons are specimen electrons that obtain energy by inelastic collisions with incident beam electrons. They are defined as electrons emitted from the specimen with energy less than 50 eV. Each incident electron can produce several secondary electrons. Production of secondary electrons is related with topography of the samples. Due to their low energy, only those electrons that are very near the surface (<10 nm) can escape from the sample and be examined. Any change in topography of the sample that is larger than this sampling depth will change the yield of secondary electrons. Detectors will collect and count these scattered or secondary electrons and send the signals to an amplifier. The final image is built up from the number of electrons emitted from each spot on the sample.

X-ray is a subsequent result from a secondary electron produced by the specimen. If an electron with lower energy (usually from K-shell) has been emitted from the atom during the secondary electron process, a vacancy is left in an inner shell. This vacancy can be filled by an electron from one of the higher energy shells, such as L or M. The excess energy of this electron, i.e. the difference between the energy states in the two shells, is radiated during the transition as a photon of x-rays. X-rays emitted from the atom have a characteristic energy which is unique to the element from which they originate. These signals are collected and sorted according to energy to identify atomic elements.

Specifically in this research work, Oxford Instruments INCA Energy Dispersive X-ray (EDX) analyzer, as a built-in functional feature on the SEM, has been used to identify and quantitatively analyze the metallic catalyst particles distributed within the silica opal templates and provide a direct impression of catalyst distribution by a mapping image. 5 KeV electron beam has been used to scan the sample.

The characteristic X-ray emission energy of different element that possibly involved is list in Table 2.1. Kα radiation happens when an L shell electron fell-in to refill a K shell vacancy. For an element with higher atomic number, like cobalt, Lα emission can happen when M shell electron fills a vacancy in L shell.

Table 2.1 Characteristic X-ray Emission Spectrum Line for Different Elements

	Carbon	**Oxygen**	**Cobalt**	**Silicon**
Kα(KeV)	0.277	0.525	6.924	1.739
Lα(KeV)	-	-	0.776	-

Because the SEM illuminates samples with electrons, usually it is required that the sample surface be conductive. Some of the manufacturer claim that need for placing conducting coatings on insulating materials is virtually eliminated by the field-emission technique. The reason is based on the fact that field-emission (FE) cathode provides a narrower and brighter electron beam than traditional tungsten or LaB_6 cathode [127], which leads to a higher ultimate resolution. FE cathode provides at least 2 order of magnitude higher brightness than tungsten cathode does, and 1-2 order higher than LaB_6 cathodes. High quality, low voltage images can be obtained with negligible electrical charging on insulating sample. However, it is not suitable to take this advantage of FE-SEM in this project because the low accelerating voltage does not compatible with EDX spectroscopy. Meanwhile, to avoid surface charging by lowering voltage indeed sacrifices the imaging resolution. Therefore, the insulating SEM samples have to be coated with a thin layer of carbon by a CAL-TEC MED 020 coating system.

2.4.2 UV-Vis-NIR Optical Spectroscopy

Study of the optical transmission and reflection properties of a photonic crystal in the UV-visible-NIR regime is the most straightforward way to reveal its photonic band structure [128]. Photonic band structure leads to a frequency dependent transmission spectrum. The crystalline structure such as, lattice constant and effective index of refraction can be evaluated from analysis of Bragg reflection.

In this research project the transmission and reflection spectrum of self-assembled silica colloid crystal (opal) and its derivatives have been measured, including opal with embedded carbon nanotubes, polymeric inverse opals and polymer–SWCNT composite films. The common structural feature of these different materials is a close packed fcc lattice made of monodisperse spheres, as shown in Figure 2.8. In different materials, the spheres can be silica or air; the surrounding space can be filled with air, polymer or polymer–SWCNT composites.

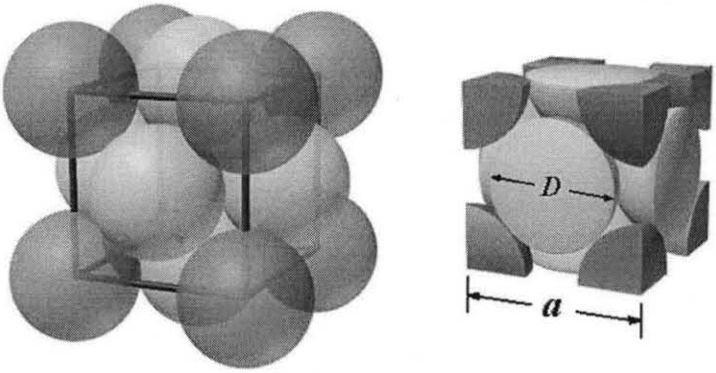

Figure 2.8 Schematic view of the fcc close packed lattice. *a* is the lattice constant and *D* is the diameter of the sphere.

In a fcc crystal, the lattice constant *a* can be expressed as

$$a = \frac{D}{\cos(45^\circ)} = \sqrt{2}D \tag{2.3}$$

where D is the diameter of the spheres.

When the (111) planes exposed on the top surface, which is usually the case of the samples involved in this research project, the interplane spacing *d* between the (111) planes can be presented as:

$$d = \frac{a}{\sqrt{h^2 + k^2 + l^2}} = \frac{a}{\sqrt{3}} = \frac{\sqrt{2}D}{\sqrt{3}} = 0.816D \tag{2.4}$$

for (hkl) = (111) crystallographic plane.

In a unit cell of fcc crystal, as shown in Figure 2.8, the volume filling factor is 74 % for those spheres and 26 % for the surrounding materials. The effective index of refraction of a material made of two different dielectrics can be calculated with equation

$$n^2_{eff} = n^2_1 f_2 + n^2_2 f_2 , \tag{2.5}$$

where n_1 and n_2 are the indices of refraction of those two materials and f_1 and f_2 are their filling factors.

Now it is ready to write down the Bragg Diffraction law in term of the lattice parameters and index of refraction. At normal incidence is

$$\lambda(D) = 2n_{eff}d = 2n_{eff}(0.816D) \tag{2.6}$$

where d is the distance between (111) planes and D is the sphere diameter. When incident angle is other than 90°, the expression of Bragg law is different [128, 129] from the traditional equation, in which diffraction peak wavelength λ is a linear function of $\cos\theta$. This correlation of $\lambda(\theta)$ is due to the presence of opals as follows:

$$\sin\theta_{air} = n_{eff} \sin\theta_{opal} \tag{2.7}$$

$$\sin^2\theta_{opal} = \frac{\sin^2\theta_{air}}{n^2_{eff}} \tag{2.8}$$

$$\cos\theta_{opal} = \sqrt{1-\sin^2\theta_{opal}} = \sqrt{1-\frac{\sin^2\theta_{air}}{n^2_{eff}}} \tag{2.9}$$

so Bragg Diffraction law in opal will be

$$\begin{aligned} \lambda = 2n_{eff} d\cos\theta_{opal} &= 2(0.816D)n_{eff}\sqrt{1-\frac{\sin^2\theta_{air}}{n^2_{eff}}} \\ &= 2(0.816D)\sqrt{n^2_{eff} - \sin^2\theta_{air}} \end{aligned} \tag{2.10}$$

where θ_{air} is the incidence angle, d is the interplane spacing between these (111) planes and D is the diameter of the sphere.

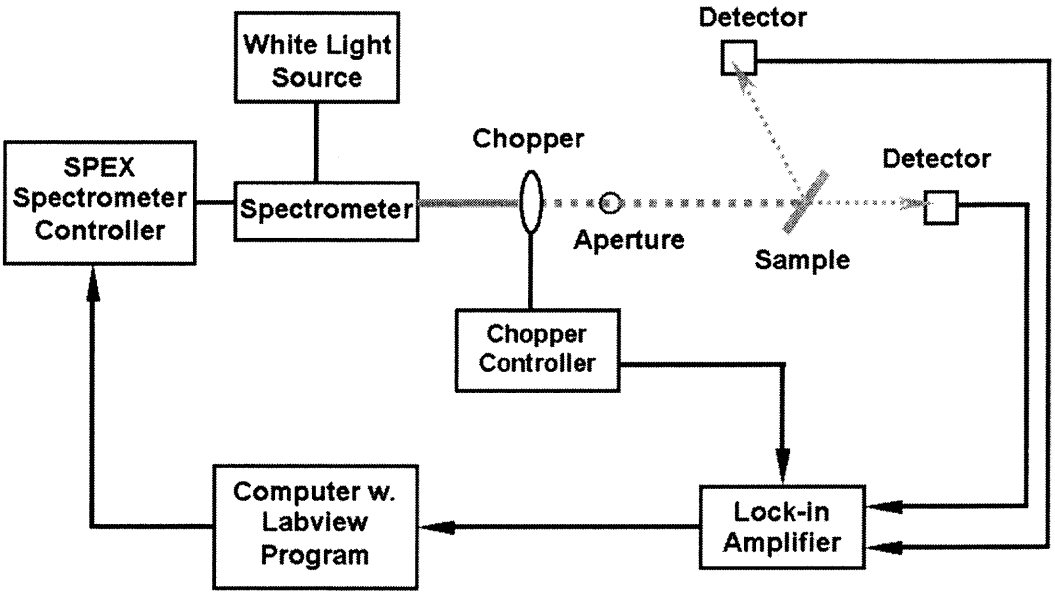

Figure 2.9 Schematic setup of optical spectroscopy measurement.

A schematic configuration of the optical measurements is shown in Figure 2.9. It can be configured to measure transmittance or reflectance separately or, simultaneously. A SPEX 1682A Broad Band Radiation Source with USHIO 100W Halogen Projector Lamp bulb installed provides the continuous light source. 10 W Deuterium lamp bulb provides UV light. With a proper diffraction grating installed, the SPEX 1681 0.22m Spectrometer has been used as monochromator. The grating spatial frequency determines the order of operation, as well as the blazing of grating determines the efficiency. In the white light experiments, a SPEX diffraction grating with 600 lines/mm frequency and 1000 nm blaze provides a spectrum rang from 400 to 1600 nm effectively. 1200 lines/500 nm grating can be used for specific UV range measurement and 300 lines/2000 nm grating can serve the purpose of a near-infrared wavelength experiment. The output spectra of monochromic light then pass through a narrow slit of 0.25 mm or 0.5 mm. Scanning for a particular wavelength was controlled by a spectrometer controller of

SPEX CD2B Compudrive that was connect to a PC via GPIB card and run by a customized Labview program. A chopper was placed between the monochromator and sample to modulate the incident light beam and provide a reference frequency to a lock-in amplifier. The sample was held on a rotatable stand to facilitate the measurement of reflection at different incidence angles. As signal detectors, silicon photodetector for 300 to 900 nm spectral range, germanium photodetector for the 800 to 1600 nm range, and InGaAs photodetector for the 1300 to 2400 nm rang has been used.

2.4.3 Optical Activity Measurement

Optical activity is a phenomenon which is observed in chiral molecules. Polarized light is rotated as it propagates through the material. This measurement may reveal the chirality of single-wall carbon nanotubes.

The experimental configuration is schematically shown in Figure 2.10. The light source is a 632.8 nm, 10 mW HUGHES helium-neon laser. A linear polarizing filter whose alignment is parallel to y direction is used to provide a polarized incident light beam. As the experiment coordinate show, x-direction is defined as the direction of the laser beam propagation and y-direction is defined as the vibrating direction of the polarized light. A chopper is used to modulate the laser beam and provide a reference frequency to a lock-in amplifier. Another linear polarizing filter mounted on a rotatable stand is used as analyzer. The alignment of the analyzer is initialized in the y direction, which is set as 0^{o}. When there is no sample between the two filters, the photodetector behind the analyzer will pickup a maximum transmission signal. At 90^{o} rotation of the analyzer, it will monitor a minimum transmission value. If an optically active sample is mounted between two filters, the filter would have to be rotated in order to compensate for any induced polarization rotation produced by the sample.

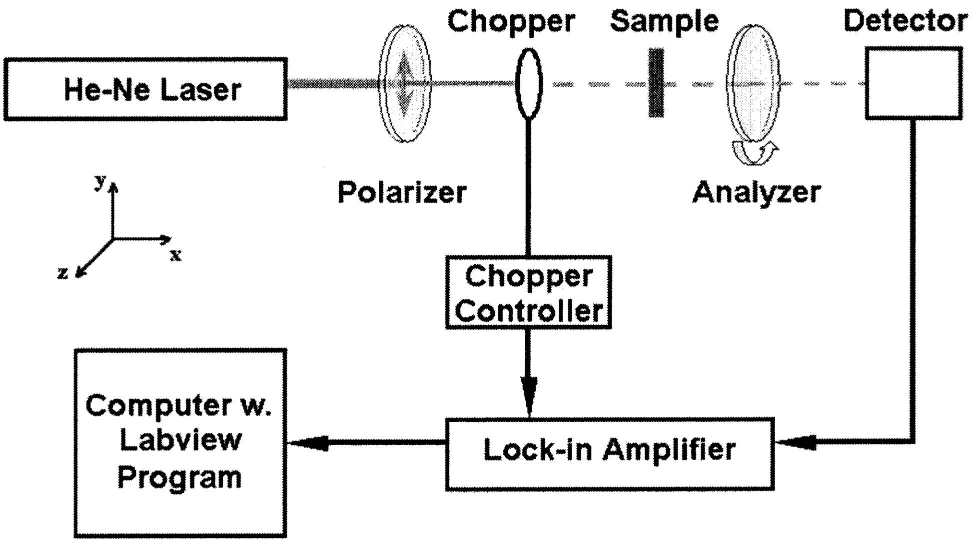

Figure 2.10 Schematic setup of optical activity measurement.

The procedure of this measurement is as follows. As the analyzer is rotated in steps of 2° counterclockwise from 0° to 180°, a computer records the optical signal through the analyzer. The resultant data is fitted by a function of

$$I = Acos^2(\varphi + \varphi_0) + A_1 \tag{2.11}$$

to evaluate the angle shift φ_0 from 90° when minimum light intensity I is achieved.

2.4.4 Raman Scattering Spectroscopy

When light is scattered from a molecule, most photons are elastically scattered at the same frequency as the incident photons. However, a small fraction of light is scattered inelastically, leaving the molecule in an excited vibrational state. The scattered radiation will be at a lower frequency (Stocks process). When the incident beam withdraws a phonon, it is scattered at a higher frequency and is named anti-Stoke process [130]. A plot of intensity of scattered light versus frequency difference is a Raman spectrum. The principle of Raman scattering is shown in Figure 2.11.

At room temperature, the thermal population of the vibrational excited states is low. The majority of molecules initially is in the ground state and may be excited to a higher energy state by the incident photons of energy $h\nu_0$. The Stokes shifted scatter light is what is usually observed in Raman spectroscopy. The anti-Stokes-shifted Raman spectrum is weaker than the Stokes-shifted spectrum.

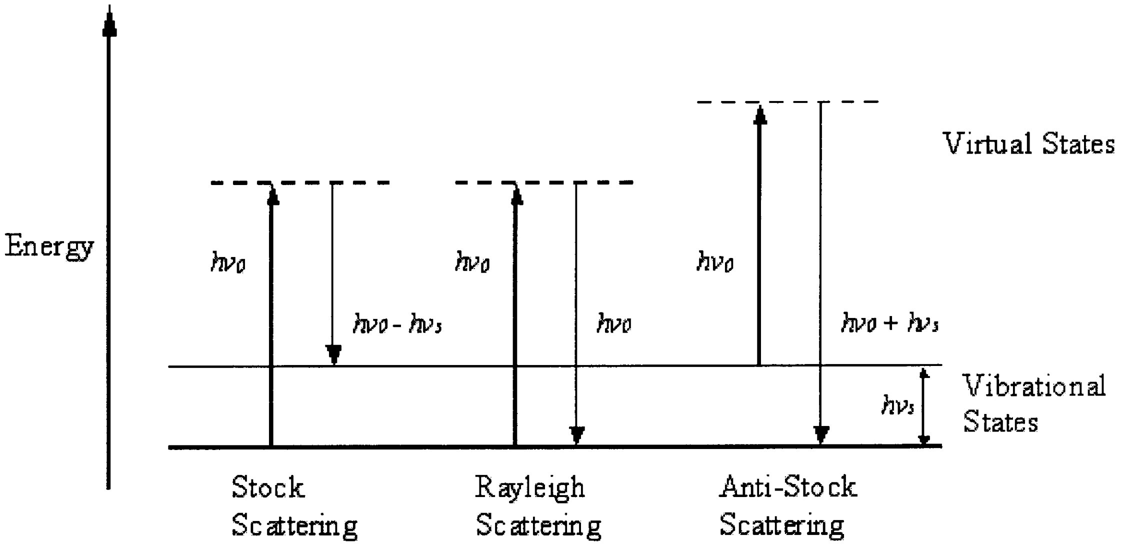

Figure 2.11 Schematic principle of Raman scattering.

The energy difference between the incident and scattered photons is represented by the arrows of different lengths in Figure 2.11. Numerically, the energy difference between the initial and final vibrational level, $\Delta\nu$, or Raman shift in wavenumbers (cm^{-1}), is calculated by Equation 2.12.

$$\Delta\nu = \frac{1}{\lambda_{incident}} - \frac{1}{\lambda_{scattered}} \qquad (2.12)$$

in which $\lambda_{\text{incident}}$ and $\lambda_{\text{scattered}}$ are the wavelengths, in centimeter, of the incidence and Raman scattered photons, respectively.

Raman spectroscopy is non-destructive and readily available characterization method to most research groups. The measurements can be done over a wide range of temperatures and pressures. It can provide unique information about vibrational and electronic properties of various materials. Although not as a direct method, it has been used to determine the structure of the material and allows the identification of materials through the characteristic vibrations of certain structures. The unique one-dimensional molecular nature of single-wall carbon nanotubes makes the resonant Raman technique an extremely useful and accurate method for the identification of chiral structure and diameter distribution of individual nanotubes or in a nanotube bundles.

A typical Raman spectrum of SWCNT presents three sets of peaks, as shown in Figure 2.12: radial breathing mode (RBM) band, defect-induced D-band, and high frequency G mode. Each part of the Raman spectrum can be used to evaluate different properties of single-wall carbon nanotubes.

Between 1550 and 1600 cm^{-1}, two strong peaks, so called as G-band, are generally observed. They correspond to the graphite E_{2g} optic mode which typically appears in highly oriented pyrolytic graphite. Generally, the intensity of the G mode of graphitic materials is sharp and strong when the sample is highly crystalline and defect free. The Raman shifts in this high frequency region do not vary much with carbon nanotube diameter. This part of peaks is usually used to distinguish between metallic and semiconducting nanotubes. In metallic carbon nanotubes, the peak at lower frequency is strongly broadened and shifted to smaller energies (1540 cm^{-1}).

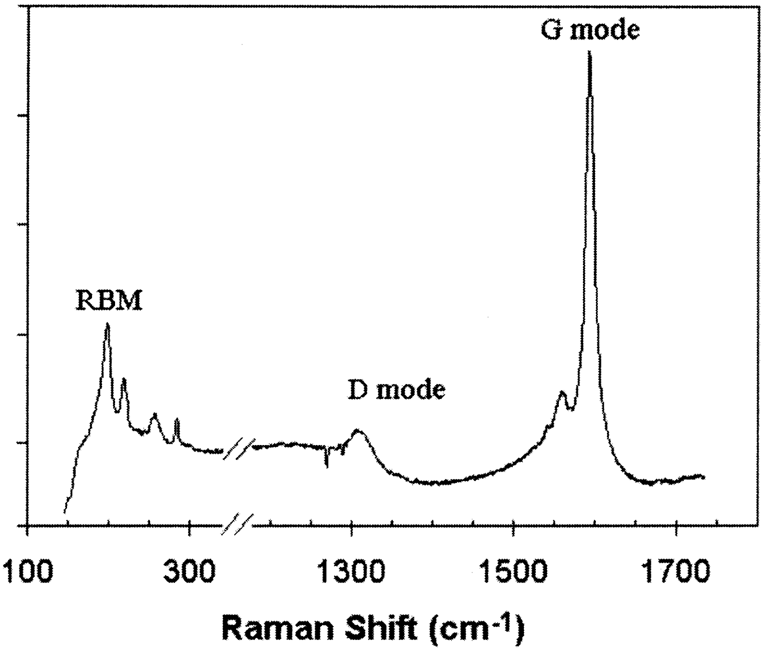

Figure 2.12 Schematic Raman spectrum.

The D band appeared around 1350 cm^{-1} is sensitive to sample quality. Disordered graphite and carbons show a broad feature in this region. For samples of SWCNT, it may come from a symmetry-lowering effect, due to defects or nanotube caps, bending of the tubes, presence of carbon nanoparticles and amorphous carbon.

The RBM band in lower frequencies is a unique feature to carbon nanotubes relative to other sp^2 carbons, where all the atoms in the nanotube are vibrating in phase in the radial direction as if the tube is breathing. In this energy region, the Raman spectroscopy of SWCNT shows a new phenomenon that is called diameter-selective resonance Raman scattering [71]. Only those (n, m) nanotubes with an energy band separation E_{ii} between van Hove singularities (vHs) [131] close to the excitation laser energy E_l present sufficient intensity for a Raman signal due to resonance excitation condition. Both theoretical and experimental work has shown that the RBM frequency ω_{RBM} is inversely proportional to the diameter of individual nanotubes (Equation 2.13):

$$\varpi_{RBM} = \frac{C}{d_t} \tag{2.13 a}$$

or

$$\varpi_{RBM} = \frac{C_1}{d_t} + C_2 \tag{2.13 b}$$

where C, C_1 and C_2 are constants. Equation 2.13 (a) usually represents the functional relationship of $\omega_{\mathrm{RBM}}(d_t)$ of individual nanotubes, as well as Equation 2.13 (b) for nanotube bundles. In nanotube aggregates, it has been postulated that there is a weak inter-tubule coupling effect via van der Waals interactions [132], which leads to a 6-20 cm^{-1} shift to higher frequencies due to the space restrictions imposed by neighboring tubes.

Molecular vibrational features of carbon nanotubes are sensitive to both the intercalation and charge transfer. So the Raman spectroscopy allows the investigation of the evolution of structural modification, including changes in the intertube interactions due to the intercalation process, and varies in electronic properties of SWCNT under doping due to charge transfer.

Application of resonant Raman spectroscopy in the investigation of doped SWCNT was first performed by Rao, *et al.* [133]. It has been found that the Raman spectrum in the radial breathing modes (RBM) range provides information about the size distribution and indicates the changes of RBM intensity upon doping, as well as the tangential modes (G-band) reveals information about the metallic or semiconducting character of nanotubes and indicates the changes of these features induced by charge transfer between the dopant-nanotube interface.

Two lasers have been used in this research work. The first one is a Spectra-Physics 166 water cool Argon laser at 488 nm wavelength, or 2.54 eV. The other was a semiconductor diode laser at 830 nm wavelength, or 1.50 eV.

2.4.5 Current-Voltage Characterization

Current-voltage measurements were used to study the conductance of the samples. A Keithley 2400 SourceMeter has been used to perform the current-voltage measurements. It is an integrated source-measure instrument that not only cuts equipment cost, but also save researchers from significant efforts to program different instruments separately, like power supplies and voltmeters or ammeters. Keithley 2400 SourceMeter can act as either a voltage source or current source with sweep, pulse, and compliance limit capabilities, and simultaneously measure current and voltage parameters with high resolution. It can source a series of voltages, measure corresponding currents, and store data into built-in memory until the I-V sweep is completed. Data are then downloaded to the PC controller for processing.

The schematic setup for the electric testing of current-voltage characteristics is shown in Figure 2.13. With the Keithley connected to a PC via GPIB card and cable, a LabView application, dedicated to I-V testing, has been programmed to control the source voltage sweep and download stored data from the buffer. The sweep step was 0.2 volt, started from –5 volts to 5 volts. The measurements were performed at room temperature. For photoconductivity measurements, a white light Hg arc lamp at an overall intensity value of 0.25 W/cm^2 was used to illuminate the sample when I-V curve was recorded. Besides doing forward, reverse bias voltage sweeps and current measurements, the current (or resistance) at a fixed voltage that might change with time was also recorded. After properly programmed the measurement delay, the current/resistance can be recorded every 0.5 seconds and plot a curve of electric response versus time. This is very helpful to study the conductance change of single-wall carbon nanotubes due to molecular photodesorption.

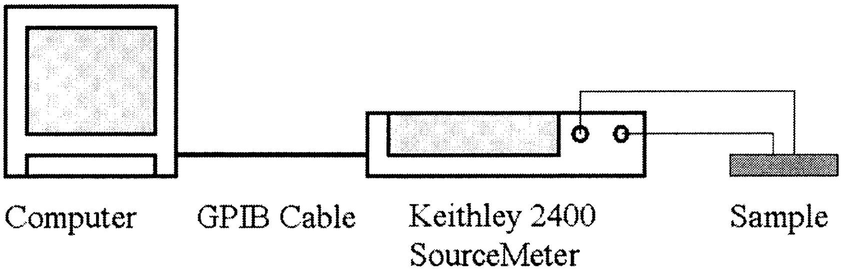

Figure 2.13 Schematic setup for current – voltage characterization.

2.4.6 Thermoelectricity – Seebeck Effects

In most of the cases, the particles that carry electric charge in a material also carry heat. Imagine a conductor with an applied temperature gradient, as shown in Figure 2.14. The electrons (in n-type materials) or holes (in p-type materials) at the hot end will move faster than those at the cold end, and will thermally diffuse from the hot end to the cold end. These charges build up at the cold end and create an electric field inside the sample. When the current generated by this electric field counteracts the thermal flow, equilibrium is reached. The electric potential produced by a temperature difference is known as the Seebeck effect. The Seebeck coefficient (also called the thermoelectric power or thermopower) is the ratio between the electric field ($\vec{E}$) and the temperature gradient ($\vec{\nabla}T$), as shown in Equation 2.14:

$$S = \frac{\vec{E}}{\vec{\nabla}T} \tag{2.14}$$

Roughly speaking, the Seebeck coefficient can be thought of as a measure of the coupling between the thermal and electrical currents in a material. Note that the sign of the Seebeck coefficient depends on the sign of the charge carriers (whether positive or negative charge builds up on the cold end). If the free charges are positive (the material is p-type), positive charge will build up at the cold end that will have a positive potential. Similarly, negative free charges (n-type material) will produce a negative potential at the cold end. The Seebeck coefficient is a way to characterize a particular material as hole or electron doped.

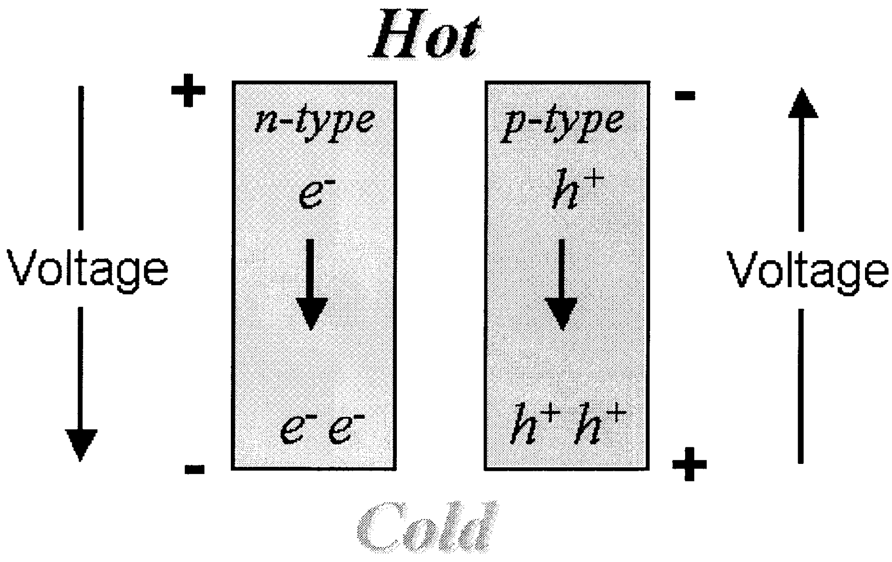

Figure 2.14 Schematic mechanism of thermoelectricity.

Based on the principle of Seebeck effect, a simple setup has been designed to determine the doping nature of as-grown SWCNT and those embedded in polymer composites. A Keithley 2400 multimeter was used as the voltmeter to measure the thermal induced voltage between two ends of the samples. The positive end of the voltmeter was connected to one end of the sample and was kept at room temperature. The negative end was connected to an iron gun with temperature control. If the voltmeter shows a positive number, it means that positive charge are building at the cold end and the sample is p-type.

2.4.7 Nonlinear Optical Characterization

The optical nonlinearity of materials strongly depends on their molecular structures. The loosely bounded electron cloud can redistribute itself in response to the external field. The magnitude of the induced polarization depends on the magnitude of the applied electric field and can be expressed as:

$$P = \chi E + \chi_2 E^2 + \chi_3 E^3 + \ldots \tag{2.15}$$

where P is polarization and E is the electrical field. χ is the electric susceptibility of the material. χ_2, χ_3 and so on are higher-order nonlinear susceptibility. When the incoming field is much weaker than the atom's internal electric field, the linear expression of $P = \chi E$ of the first order term in Equation 2.15 is used. Under irradiation of a strong laser, the higher-order terms cannot be ignored. The basic requirement for second order NLO behavior is that molecules cannot be centrosymmetrical because otherwise the charge polarization on opposite direction of the molecule will be compensated by on another [134].

The molecule of a single-wall carbon nanotube shaped as a rolled-up graphene sheet with hemisphere caps on each end. All carbon atoms in the molecule are sp^2 hybridized, which has a π electron and 3 sharing σ orbital electrons. Those π electrons are highly delocalized over the whole tubular molecule. The hexagonal lattice of the carbon atoms, just like benzene rings, is centrosymmetrical. This may results in the zero χ_2. On the other hand, the very efficient π electron delocalization system is highly deformable, which may lead to a significant χ_3 [135]. It was reported that χ_3 increases when the electric field is applied along the tube axis [136]. This further indicates the contribution of the π delocalization to the third order nonlinear coefficient.

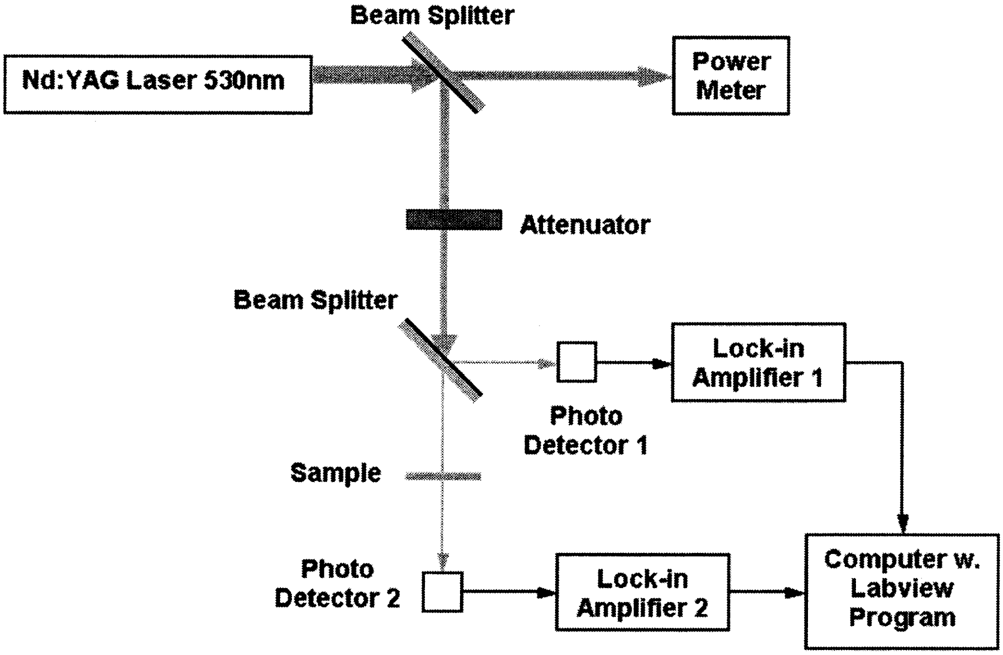

Figure 2.15 Schematic setup of nonlinear optical transmission measurement.

Nonlinear optical transmission measurements have been conducted on pristine single-wall carbon nanotubes grown by CVD and embedded in regular opaline structure. A Q:switched Nd:YAG pulsed laser operated at λ = 532 nm, 10 nanosecond pulses at 10 Hz, has been used as the excitation laser. Different intensities of the laser were employed to measure the corresponding transmitted signal. A schematic setup for nonlinear optical experiments is shown in Figure 2.15.

Nonlinear optical characterization was also carried out on photoconductive polymer–SWCNT composites. The interaction between conjugated polymer and carbon nanotube sidewall may change the conjugated system and affect the ability of delocalization of π electrons. A consequential change in the optical nonlinearity may be observed in these composite materials. In this research work, PVK-DEH photoconductive polymer complex has been introduced into the opal template, incorporated with single-wall carbon nanotubes grown in the template by CVD technique to form uniform composite material.

CHAPTER 3

RESULTS AND DISCUSSION

3.1 Synthetic Silica Opal

Monodisperse silica sphere is the basic building block of the opal template – the basis for the nanostructured composite. The parameters of sol-gel chemical process that affect the morphology and dimension of the silica colloidal spheres will be discussed in this section. The sizing results of particles by different characterization technique are listed and compared. The colorful appearance and the crystalline structure of self-assembled silica colloid crystal, or silica opal, is shown in this section. Its optical properties have been discussed.

3.1.1 Synthesis of Monodisperse Silica Spheres

A sol-gel process, also know as Stöber-Fink-Bohn technique has been used to synthesize highly monodisperse silica colloidal spheres, as described in Section 2.1.1. With understanding of the detailed mechanism of this chemical reaction, desirable parameters can be controlled in order to produce a high quality silica colloidal suspension.

The initial hydrolytic reaction is invisible and its rate strongly depends upon water content in the reacting system. The condensation of the supersaturated silicon hydroxyl groups can be observed by an increasing opalescence of the mixture because of the formation of solid ≡Si-O-Si≡ networking. Larger content of water increases the rate of reaction for a given TEOS and ammonia concentration levels.

The effects of ammonia are more complicated. First, it directly catalyzes the formation of siloxane (≡Si-O-Si≡) cross-linkages in the condensation procedure. On the other hand, it influences the morphology of the resultant silica particles. It has been used as a triggering component to create spherical shaped particles during the reaction. When sufficient ammonia is present in the initial reaction mixture at room temperature, spherical silica particles can be obtained. In the absence of ammonia, the silica flocculates in irregularly shaped particles and no spheres can be observed. Figure 3.1 shows an SEM image of silica particles when ammonia present in the reaction is not sufficient. Finally, a presence of ammonia can lead to reactions with surface silanol (≡Si-OH) groups on the consolidated Si-O-Si clusters to create negative surface charges (≡Si-O^-). Negative surface charge causes electrostatic repulsion between spherical clusters. This effect inhibits undesired aggregation after monodisperse silica spheres were obtained.

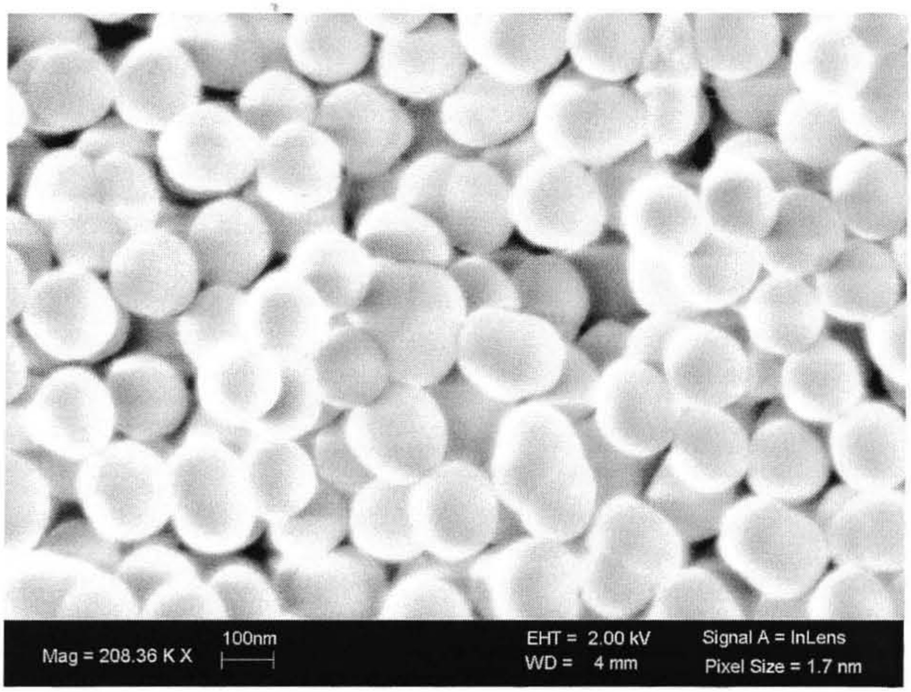

Figure 3.1 SEM image of silica colloidal particles produced when ammonia is insufficient in the sol-gel reaction.

The final silica sphere's diameter depends on the initial water and ammonia concentration. Table 3.1 shows the resultant diameters of silica spheres obtained at various components concentrations.

Table 3.1 Diameter of Colloidal Silica Spheres as a Function of Concentration of Different Reactants

TEOS (mol/l)	NH_3 (mol/l)	H_2O (mol/l)	Diameter* (nm)	Relative S.D. (%)
0.314	0.766	3.51	432	5.21
		5.51	524	3.89
		7.01	568	6.71
		8.51	644	4.80
		10.01	655	3.97
		11.51	766	5.01
0.225	0.766	3.51	467	5.62
		5.51	576	6.01
		7.01	677	4.23
		8.51	646	3.56
0.255	0.383	2.76	198	4.21
		2.87	203	3.54
		3.04	240	4.06
		3.26	276	6.09
		3.76	288	4.95
		4.26	301	4.71

*Note: The data were obtained with N4 Plus (PCS technique).

Beckman Coulter N4 Plus has been used to determine the particle average size by measuring their rate of diffusion through a fluid, as described in Section 2.1.2. In the last column of Table 3.1, the calculated relative standard deviation (RSD) of silica particles (Equation 2.2) with different diameters is presented. This parameter provides a good quantitative indication of monodispersity of the silica colloid.

To verify the accuracy of PCS technique, scanning electron microscopy has been used. It is found that the two techniques provided similar data. For example, a sample with a mean size of 276 nm measured with PCS is measured as 274.1 nm with SEM. The diameters of 50 particles have been averaged in the process.

3.1.2 Structure of Self-assembled Silica Opal

Gravitational sedimentation was used to deposit planar opal films when the corresponding spherical diameter was smaller than 400 nanometers. As described in Section 2.1.3, the opal films consist of silica spheres larger than 400 nm have been deposited vertically by capillary forces driven self-assembly.

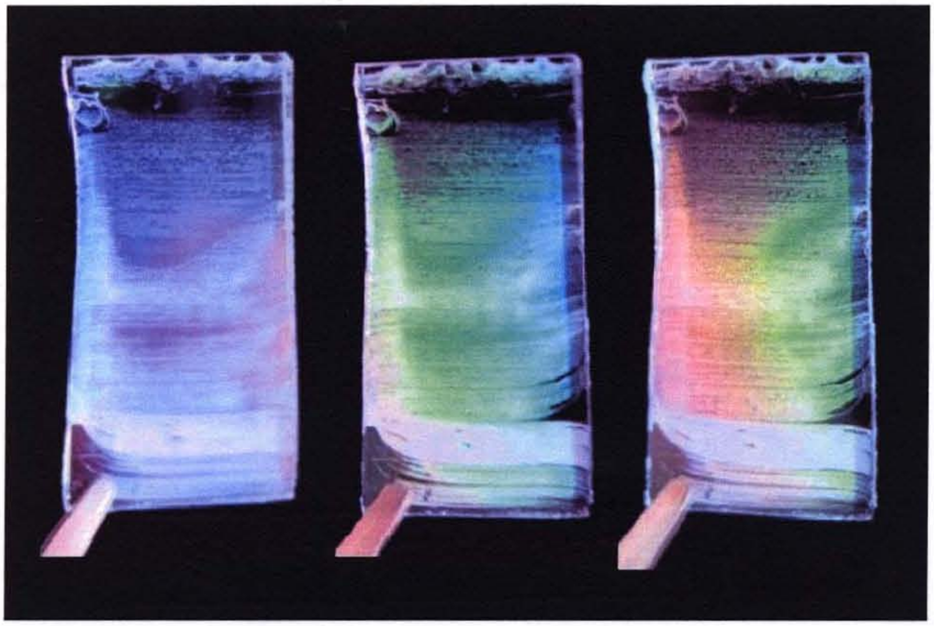

Figure 3.2 Iridescent planar silica opal deposited on quartz substrate.

Figure 3.2 shows a colourful picture of a thin opal film deposited on quartz with 503 nm monodisperse silica spheres. Vivid colours can be observed at different reflection angles due to second order Bragg diffraction from the (111) planes. The SEM image shown in Figure 3.3 reveals that the silica spheres was indeed arranged in an fcc close packed crystalline structure with (111) crystallographic plane on the top surface.

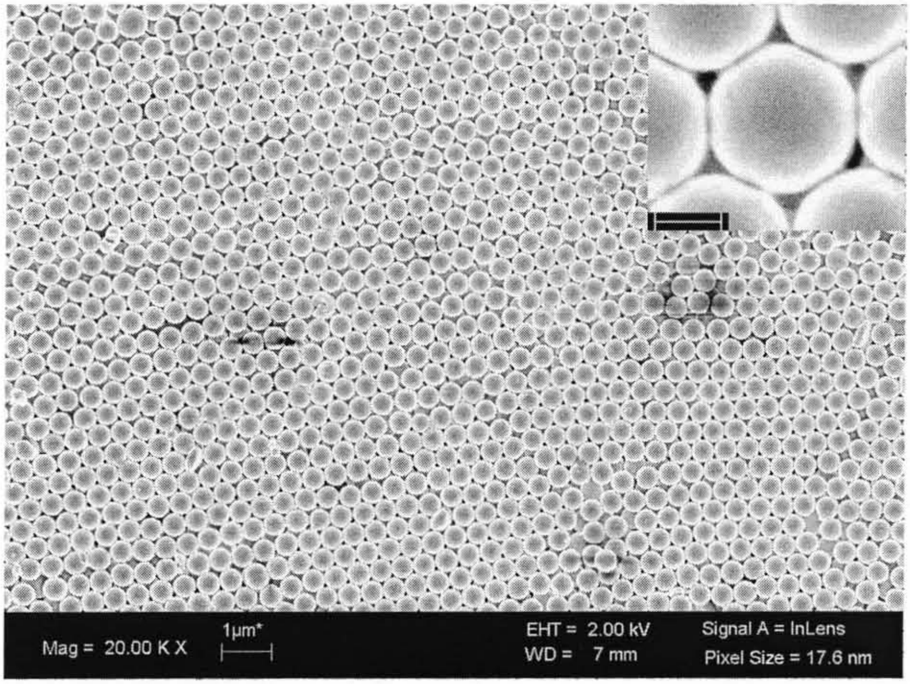

Figure 3.3 SEM image of the top layer of silica opal. The inset image reveals detail of the connection-necks between neighboring silica spheres with 200 nm scale bar.

In order to improve the mechanical stability of the artificial silica opal, a high temperature sintering at 800 °C was carried after the deposition. This process improves the interconnections between neighboring silica spheres. This is crucial to the later stages when the original silica matrix is removed. It ensures connectivity throughout the structure so that the etchant can reach every silica spheres and totally remove the template. The inset image in Figure 3.3 shows the connection-necks between neighboring silica spheres after sintering at 800 °C for 3 hours.

3.1.3 Optical Characterization of Silica Opal

To optically characterize the 3-D highly ordered opaline crystal structure, UV-vis-IR (wavelength from 400 to 1600nm) light transmission and reflection measurement have been performed.

In silica opal, the index of refractions of its two components are $n_{air} = 1$ and $n_{SiO_2} = 1.45$ respectively. The effective index of refraction of opal can be calculated with equation 2.5, $n^2_{eff} = n^2_{air} f_{air} + n^2_{SiO_2} f_{SiO_2}$. The calculated effective index of refraction is $n_{eff} = 1.348$.

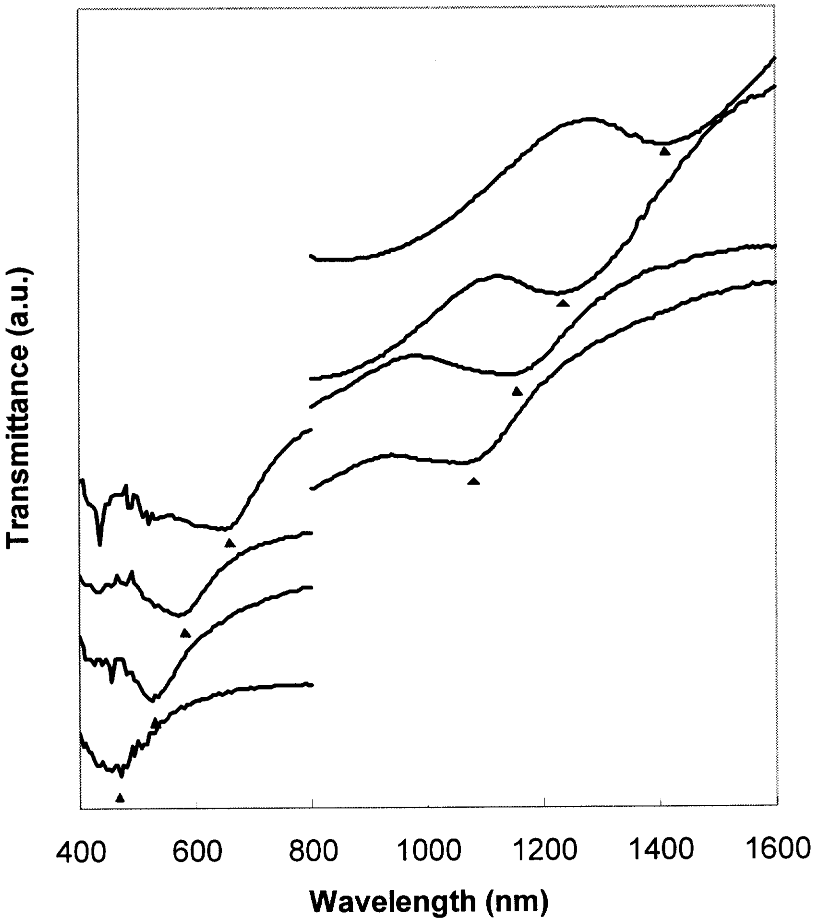

Figure 3.4 Normal incidence optical transmission spectra of silica opals with different spherical diameters. These curves have been vertically offset for clarity. From left to right, the band position corresponding to the following spherical size of the silica opal: 203nm, 240nm, 276nm, 301nm, 503nm, 524nm, 568nm, and 655nm.

Optical transmission spectra for samples made of silica spheres with various diameters were taken at normal incidence ($\theta = 0°$). In Figure 3.4, a clear attenuation band can be observed due to Bragg refraction in the [111] direction. As the sphere size increases, the dip occurs at longer wavelengths, or red shifted.

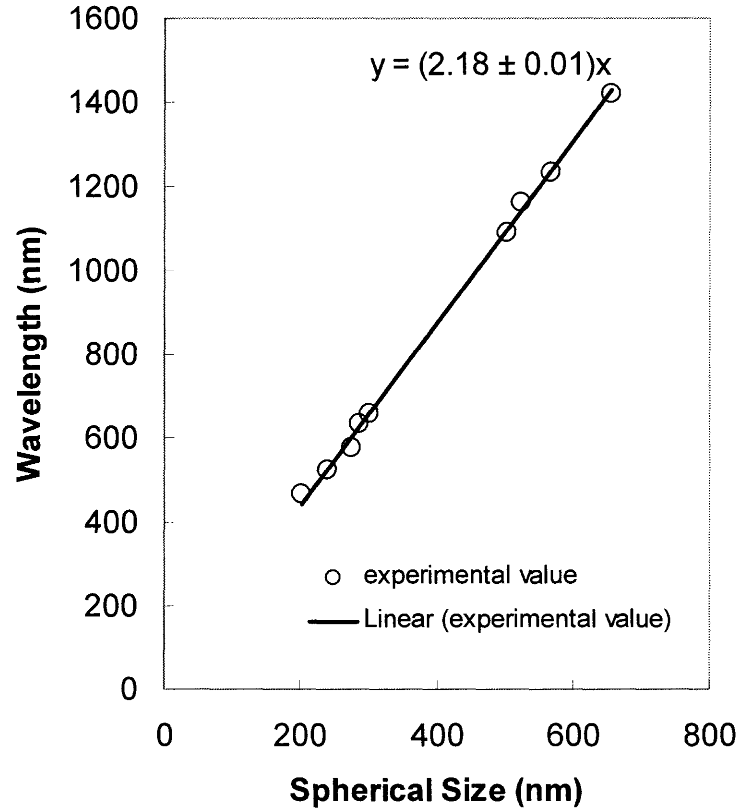

Figure 3.5 Size dependence of the optical attenuation band position of silica opals. The circle marks represent the experimental band position, the solid line represents the best linear fit of the function $\lambda(D)$. The diameters of the silica spheres used for the measurements were: 203nm, 240nm, 276nm, 288nm, 301nm, 503nm, 524nm, 568nm, and 655nm, respectively.

Figure 3.5 shows the functional relationship between the peak wavelength (λ) of the transmission band and corresponding sphere size (D). The circles mark the experimental band position, while the solid line represents the best linear fit of the function $\lambda\,(D)$ based on Bragg Diffraction law at normal incidence (Equation 2.6). It is deduced from the equation that the slop of function $\lambda(D)$ equals to $1.632n_{\mathrm{eff}}$. The best fit line in Figure 3.5 exhibits a slop of 2.179 and leads to experimental $n_{\mathrm{eff}} = 1.34$, which is very close to the theoretical value, $n_{\mathrm{eff}} = 1.348$.

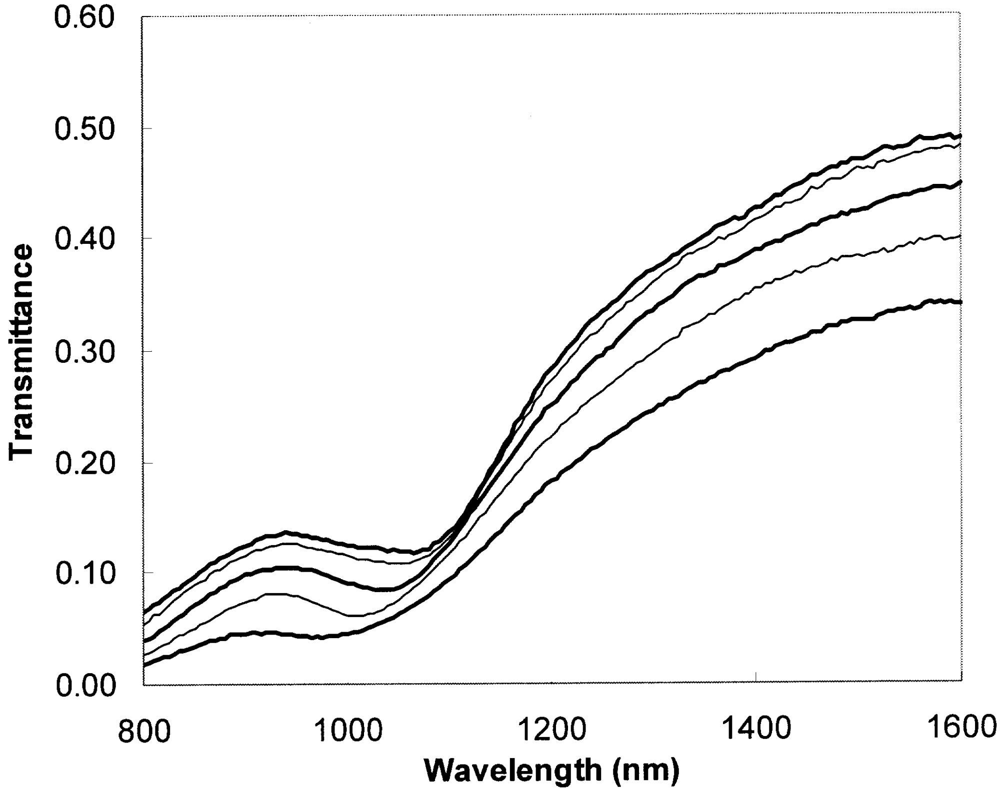

Figure 3.6 Optical transmission spectra recorded at different incident angles from opal with spherical diameter 503nm. From top to bottom, each curve corresponding to incident angle of 0°, 10°, 20°, 30°, and 40°.

Optical transmission and reflection measurements have also been performed at different incident angles θ with respect to the surface normal. Figure 3.6 shows the transmission spectra and 3.7 the reflection spectra, measured on a sample crystallized from silica spheres of 503 nm. In the transmission spectra, a clear attenuation band can be observed which is function of the incident angle. Strong peaks of reflection corresponding to the (111) Bragg reflections can be observed as well. As the incident angle increases, a blue shift of optical band position is also noted in both spectra. The plot of reflection peak wavelength (λ) versus incident angle (θ) of measurement, as shown in Figure 3.8 reveals the dependency of band position on incident angle. The experimental data (hollow circles) can be closely fitted with the theoretical function of Bragg diffraction law $\lambda(\theta) = 2(0.816D)\sqrt{n_{eff}^2 - \sin^2\theta}$ with the n_{eff} = 1.348 (solid line). This version of Bragg law represented in opal has been explained in Section 2.4.2, Equation 2.7 to 2.10.

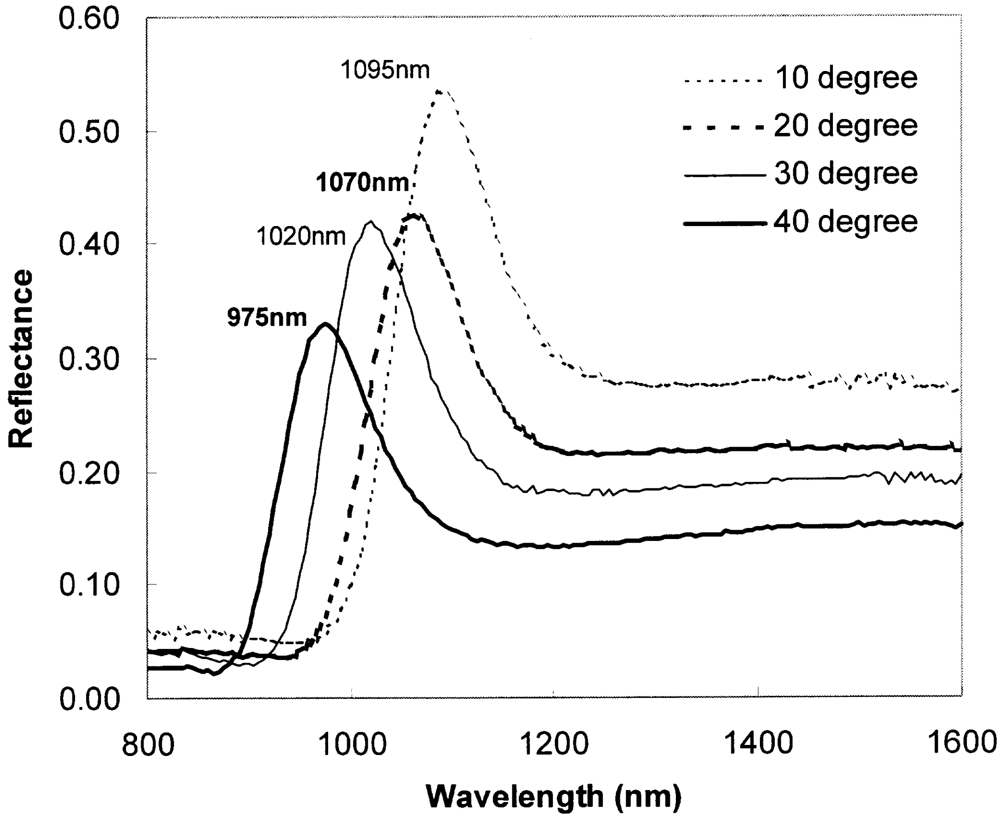

Figure 3.7 Optical reflection spectra at different incident angles from opal with spherical diameter 503nm.

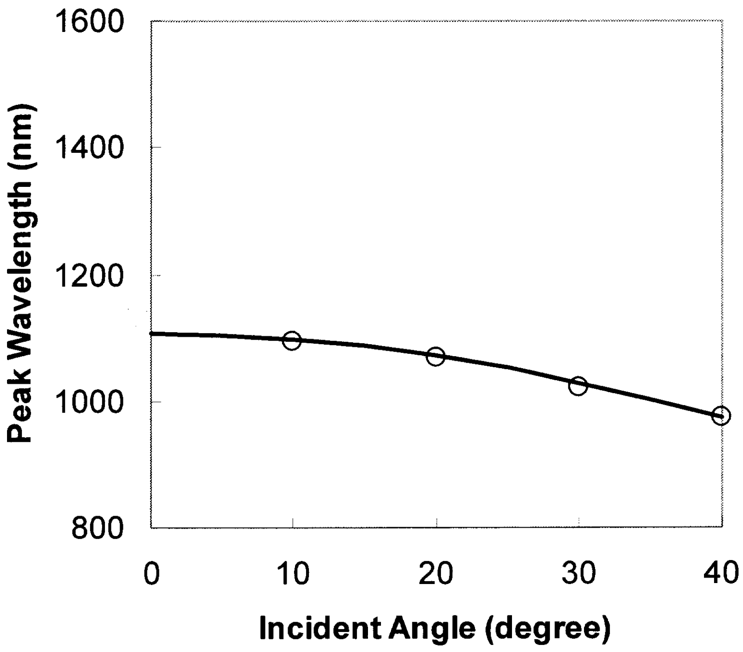

Figure 3.8 Angular dependence of reflection peak position. Hollow circular marks represent experimental peak wavelength measured at different incident angle; the solid line represents the theoretical function of Bragg law (Equation 2.10).

3.2 SWCNT Embedded in Synthetic Opal Template

More technical details about catalytic disproportionation CO by thermal chemical vapor deposition will be discussed in the following sections. These include distribution of catalyst in the template, the role of catalyst concentration and efficiency in the nanotube growth and the effect of carbon nanotube on the morphology of silica template. Also will be discussed is the quality of these in-house single-wall carbon nanotubes as characterized by Raman spectroscopy.

3.2.1 Controlled Growth of SWCNT by CVD

The catalyst $Co(NO_3)_2$ originally in form of crystalline particles and has been dispersed into the silica template from its ethanol solution. There are two possible ways to infiltrate catalyst into the silica opal template. First technique is directly mixing the ethanol solution of cobalt nitrate with the silica alcosol directly, and then grows opal film from the mixture, as described by Lan *et al.* [54, 137]. Another way is to deposit silica opal film from the pure ethanol suspension first, then immerse the sample into the cobalt solution overnight [138].

After a series of experiments, it has been found that the first method did not produce high quality opal films. With the cobalt nitrate addition in the silica-ethanol colloidal system, the silica spheres aggregated severely and precipitated much faster than in the pure silica alcosol. This occurred with very small silica spheres and may be explained by the salt induced aggregation phenomenon. Initially, the colloid system was stabilized by electrostatic repulsive barrier due to the negatively charged surface by $\equiv$Si-O$^-$ of each individual sphere. In a salt free colloid, the positive counter ions balancing the negative surface charge are diffusely oriented around the particle. Thus, the repelling forces between particles extend for some distance out from the particle surface. By introducing salts charges into the dispersion, the counter ions move much closer to the particle surface, which reduces the distance through which the repelling forces act. This causes a reduction in sol stability by increasing the probability of inter-particle collision.

To avoid such undesired aggregation of silica spheres at fast precipitating rates, another method has been developed. Pure silica opal film was deposited first, then infiltrated by ethanol solution of $Co(NO_3)_2$. Different concentration of the solution can be used to control the quantity of catalyst adsorbed on the opal templates. Figure 3.9 shows a SEM image of the opal template coated with $Co(NO_3)_2$ and its corresponding EDX elemental analysis results. It is evident that soaking of silica template with catalyst solution will not disturb the quality of the 3-D ordered crystalline structure.

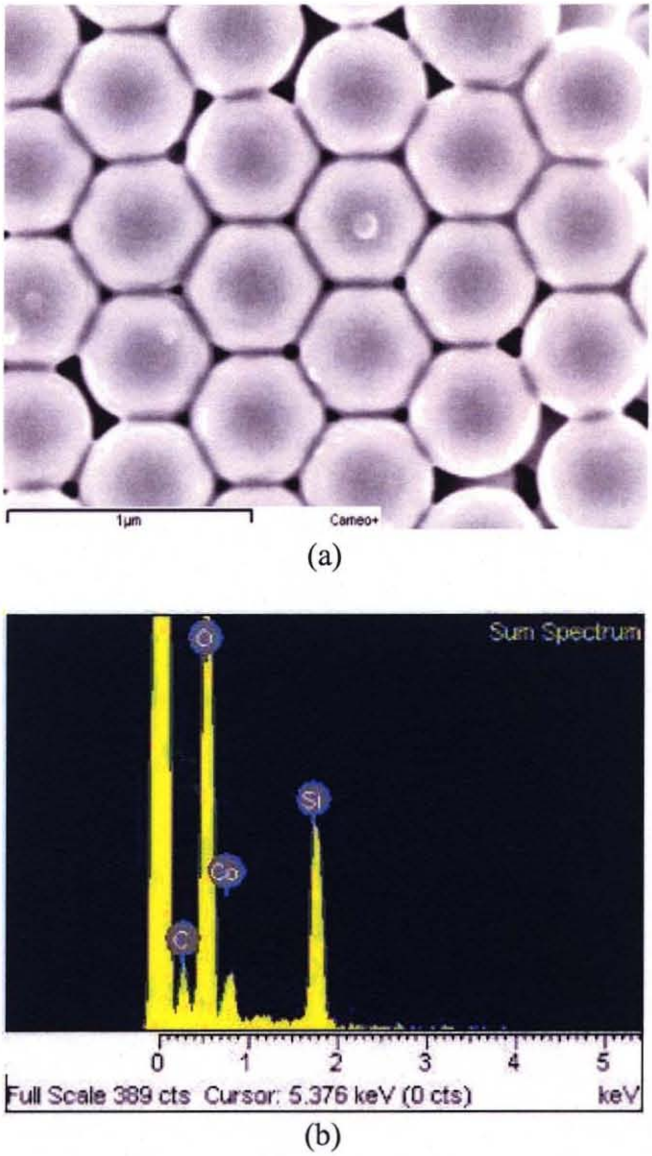

Figure 3.9 SEM and EDX elemental analysis results. (a) SEM image of silica opal template coated with $Co(NO_3)_2$; (b) EDX full spectrum with different elements labeled.

Table 3.2 Quantitative Result of EDX Elemental Analysis

Element	C	O	Si	Co	Total
Weight %	6.33	49.88	29.40	14.39	100
Atomic %	10.68	63.16	21.21	4.95	100

Figure 3.9 (b) shows the full elemental spectrum taken from the surface of the opal template soaked with cobalt nitrate. The carbon line appearing in the data is due to amorphous carbon coating the sample surface in order to make the insulating sample suitable for SEM measurement. The intensity of each peak is proportional to the atomic percentage of each component present. That is the reason for EDX being used to provide quantitative analysis to the detected elements, as shown in Table 3.2. The absence of Kα line of cobalt is because that the incident electron beam energy has been used is not high enough to knock off an innermost K electron of cobalt and excite Kα radiation. The reason for applying a rather low energy beam is the low conductivity nature of silica opal surface and insulating substrate. High-energy electron beam would lead to a severely charged surface. Except for that, K lines of C, O and Si and Lα line of Co have been detected.

In this project, the quantitative analysis provided by EDX has a limited value because of the small detectable depth of the SEM/EDX technique. An accurate quantitative investigation of cobalt – silica opal system still relies on traditional weight scale. An Ohaus AP-250D laboratory balance with readability of 0.01mg has been used to measure the weight of samples.

EDX can also provide elemental mapping which presents a direct visual image showing the distribution of different elements on the sample surface. Figure 3.10 shows the evenly distribution of cobalt on silica template surface. It is evident that the new soaking technique of catalyst not only kept the quality of synthetic opal template intact, but also was effective to evenly distribute the catalyst seeds inside the template.

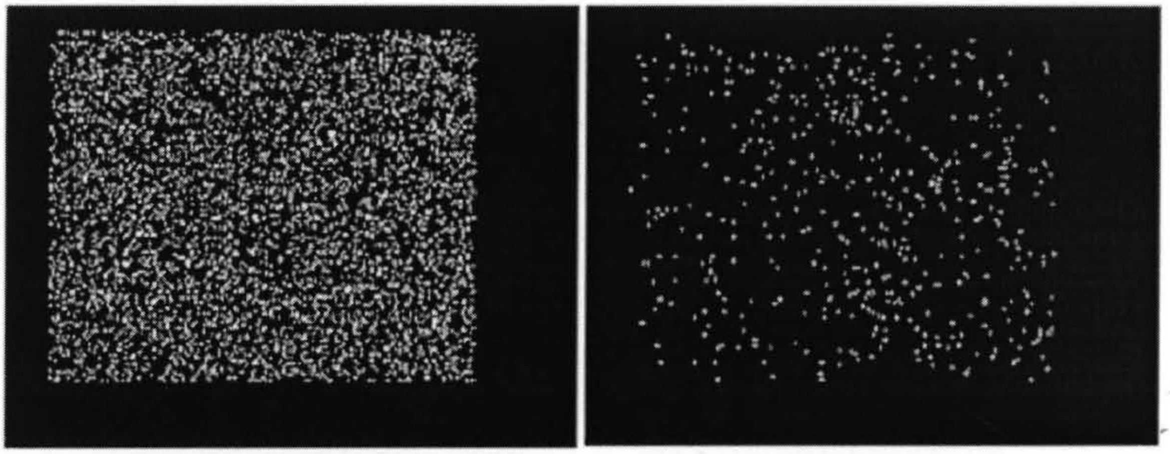

Si Ka1 Co La1

Figure 3.10 EDX mapping results of cobalt distribution in silica opal template.

In the following catalytic thermal CVD process, the cobalt nitrate adsorbed in the silica template will break down into cobalt oxide nanoparticles in air first, then consequently reduced to cobalt by hydrogen flow. The resulting cobalt particles act as catalyst to induce the disproportionation of carbon monoxide into carbon and carbon dioxide.

Figure 3.11 shows a SEM image of the top surface of a silica opal template with carbon nanotubes grown by CO-CVD process. The tubes in the image appear to aggregate into bundles which in turn, occupy the voids of the template. The average size of these bundles is less than 10 nanometers, which can be estimated from the high resolution SEM image (Figure 3.11 b). The bundles disperse evenly through the entire template and form an open but interconnected network of single-wall carbon nanotubes. The quality of the tubes has been evaluated by Raman spectroscopy and the results are shown in Section 3.2.3.

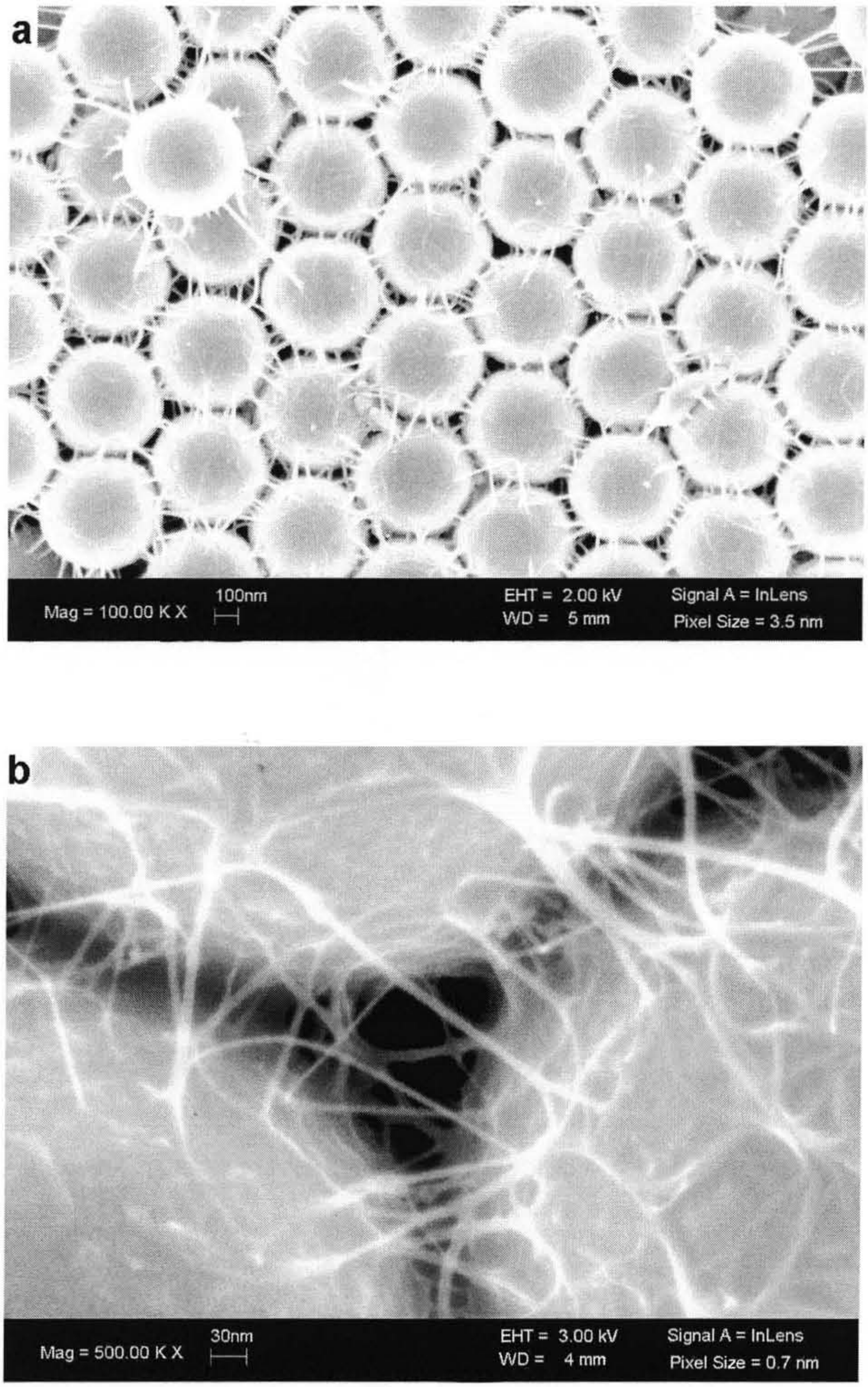

Figure 3.11 SEM image of SWCNT grown in synthetic silica opal template made of 503 nm silica spheres.

Proficiency of the single transition metal catalyst, cobalt, in disproportionation of carbon monoxide and growth of carbon nanotubes has been systematically studied first in a opal template made of 738 nm silica spheres. With the help of a high precision weight scale, the quantity results of catalyst productivity have been calculated and are shown in Table 3.3. The mass of silica template was carefully weighted before and after the growth of nanotubes. The weight loss of bare silica template and catalyst during the CVD process was considered as well. It has been found that after 2 hours of pre-annealing at 800 °C, the bare silica opal template lost weight as a result of water evaporation, yet improved its mechanical stability. There is no further weight loss by the structure during post CVD stage involving temperatures of about 800 °C. Weight loss as a result of catalyst decomposition, when $Co(NO_3)_2{\cdot}6H_2O$ salt is reduced to cobalt, has been found to be 79.7%. That is, the final weight of cobalt nanoparticles is approximately 20% of the initial salt weight.

Table 3.3 Productivity of Cobalt Nitrate Distributed in Silica Opal Template

Silica Template (mg)	**Catalyst (mg)**	**SWCNT (mg)**	**Cat. : Silica (wt. %)**	**SWCNT : Co* (wt. %)**
1.3	1.3	0.13	100	242.3
4.5	1.8	0.085	40.00	91.8
3.5	1.5	0.64	42.86	79.0
4.6	1.5	0.24	32.61	69.5
3.3	0.9	0.21	27.27	71.7
5.2	1.1	0.33	21.15	38.5

*Note: the SWCNT : Co is the percentage weight ratio between carbon nanotubes and the element cobalt.

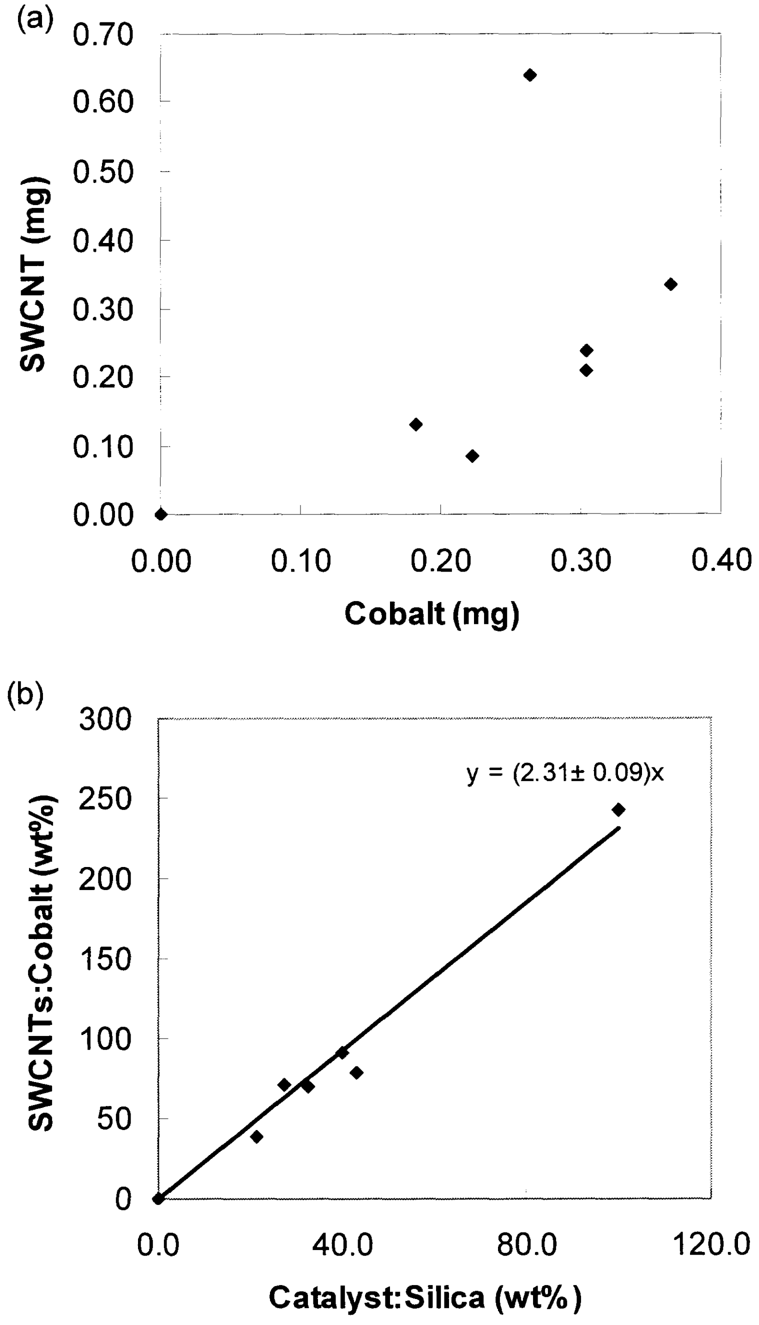

Figure 3.12 Catalyst productivity in the CVD process to grow SWCNT in silica template made of 738 nm silica spheres. (a) Experimental data of the amount of SWCNT versus cobalt. (b) Functional relationship between the yield of SWCNT from cobalt and catalyst concentration in silica template.

Although it has been found that there is no functional relationship between the amount of SWCNT produced by CVD to the absolute weight of catalyst used in the process [Figure 3.12 (a)], situation is different when data are analyzed in another way.

The weight ratio of catalyst-to-silica template (catalyst : silica wt %) is identified as the "effective catalyst concentration" in the support matrix, and the weight ratio of carbon nanotubes-to-cobalt (SWCNT : cobalt wt %) as the "cobalt productivity". Such approach results in an assessment of cobalt productivity.

Figure 3.12 (b) shows the linear relationship between cobalt productivity and catalyst concentration resulted from quantitative analysis.

$$\frac{[SWCNT]}{[Co]} = A\frac{[Co]}{[Catalyst\_Support]} \tag{3.1}$$

Equation 3.1 indicates that the absolute amount of carbon nanotubes produced from catalytic CVD is inversely proportional to the weight of catalyst support (opal template), and directly proportional to square of the absolute amount of cobalt, namely, $[SWCNT] = A \cdot [Co]^2 / [catalyst\ support]$. Here A is a constant identified as the "catalyst productivity coefficient".

The above experiment and quantitative analysis have been repeated for other two sets of silica opal templates, which were made of smaller silica spheres with diameter of 503nm and 276 nm respectively. Figure 3.13 shows that the catalyst productivity coefficient, A, decreases upon decreasing the diameter of silica spheres consisting the template.

Based on the functional relationship of Equation 3.1, this phenomenon may be explained as follows: The silica templates are close packed fcc crystalline structures with a constant filling factor of f = 0.74. The catalyst seeds have been evenly distributed within these templates as monitored by SEM and EDX. In a template made of smaller spheres, voids become smaller. The interaction between the reactive CO gas and catalyst nanoparticles becomes less efficient. Thus, the growth of nanotube may be constrained by space limitation and by the in- and out-diffusion rate of reactant (CO) and by-product (CO_2).

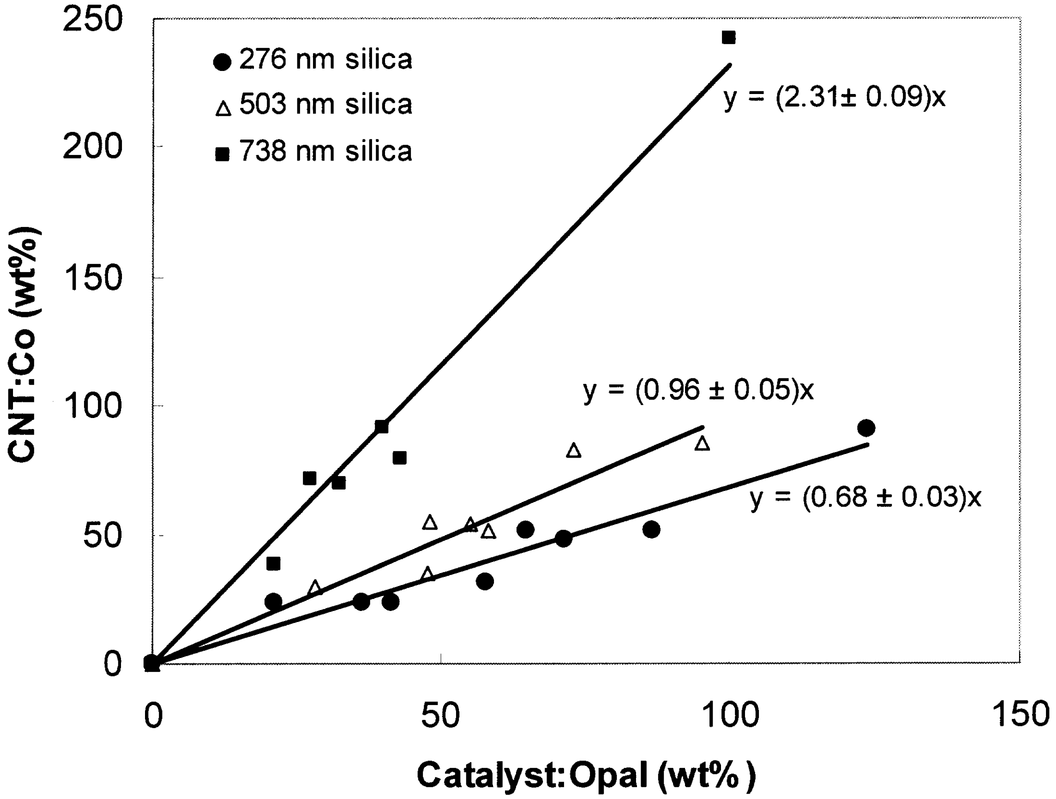

Figure 3.13 Comparison of catalyst productivity in silica templates made of silica spheres with different diameter. The square marks represent result from 738 nm spheres, triangular marks for 503 nm spheres and circle marks fro 276 nm spheres. The solid lines are the best linear fits and k is the slope.

Figure 3.14 shows SEM images of small bundles of single-wall carbon nanotube grown in opal templates consisting of (a) 738 nm and (b) 276 nm silica spheres. The catalyst concentration (catalyst : silica wt%) for these two samples are similar, approximately 40%. In both images, nanoparticles of cobalt can be observed inside the template. Aggressive growth pattern is shown in templates with larger spherical size. A network of nanotubes has formed and covered the surface of all silica spheres. The template with smaller spherical size results in smaller number of nanotubes, while most of them are simply dwelling on the substrate surface.

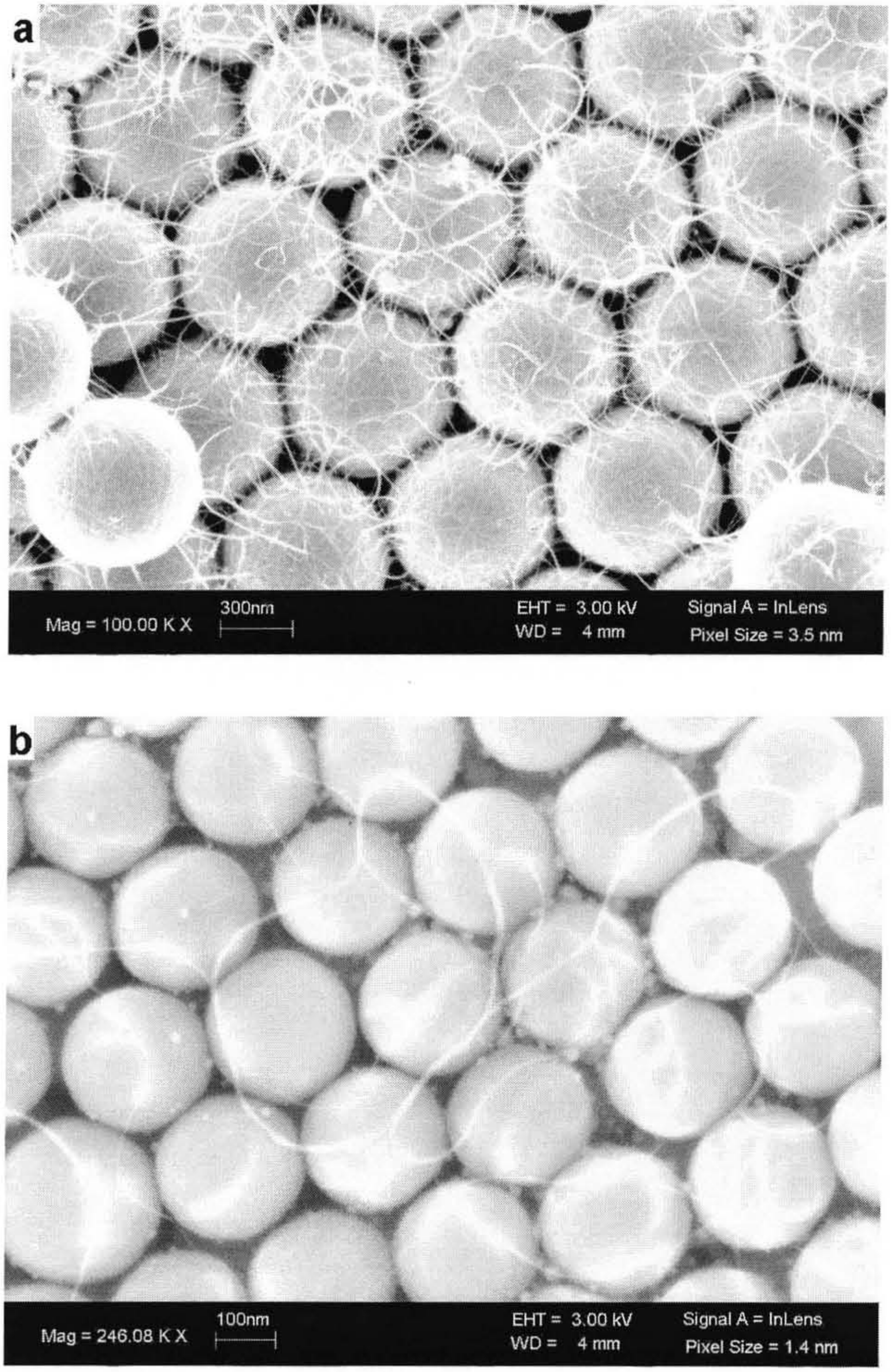

Figure 3.14 SEM images of single-wall carbon nanotubes grown inside opal templates made of silica spheres with different diameter. (a) shows template with 738 nm spheres and (b) for 276 nm spheres.

This difference may due to the fact that high quality single-wall nanotubes with fewer defects tend to grow straight without bend. Defects and strains may cause, to some degree, the tube to bend. The surface curvature in templates made of small silica spheres is larger than the one with large spheres. It makes high quality nanotubes difficult to comply the resultant strain. This explains the less efficient carbon nanotubes yield in opal template made of 276nm spheres compared to 738 nm spheres.

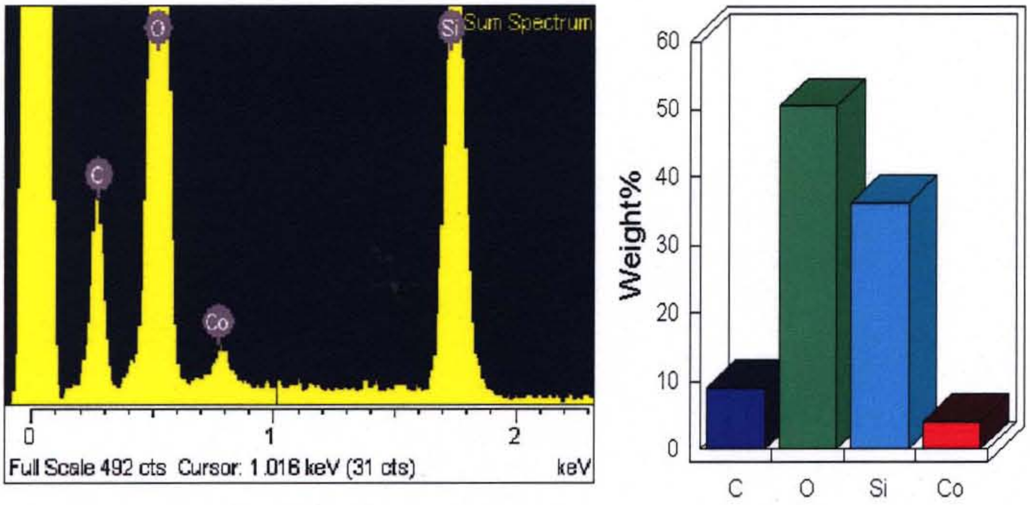

Figure 3.15 EDX spectroscopy results of SWCNT grown in opal template. Left – EDX full spectrum with different elements labeled. Right – weight percentage of all detected elements.

Table 3.4 Quantity Result of EDX Elemental Analysis

Element	**C**	**O**	**Si**	**Co**	**Total**
Weight %	9.76	50.35	35.21	4.68	100
Atomic %	15.33	59.33	23.71	1.63	100

EDX has been used to quantitatively analyze the carbon nanotube yield, at least at the sample surface. The advantage of using EDX at this stage is that the growth of nanotubes made the sample more conductive so no amorphous carbon coating is required.

Side by side, the full spectrum of all elements and their weight percentage diagram are shown in Figure 3.15. The quantity of atomic percentage for each component is shown in Table 3.4

3.2.2 Optical Characterization

To understand whether or not the crystal quality of the silica opal template is damaged after the growth of carbon nanotube, optical transmission and reflection has been conducted at various incident angles with a sample made of 503 nm silica opal and embedded with SWCNT grown by thermal CVD.

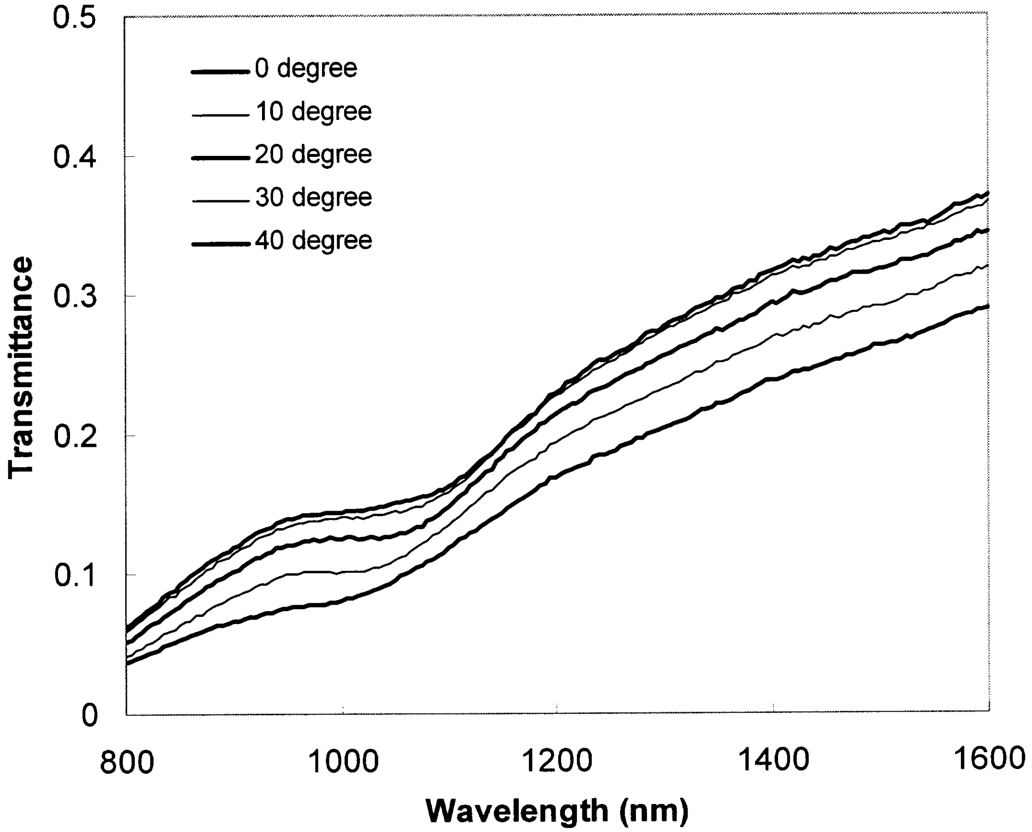

Figure 3.16 Transmission spectra of 503nm opal template embedded with SWCNT measured at different incident angles. From top to bottom, the curves corresponding to incident angle at 0°, 10°, 20°, 30°, and 40°.

As shown in Figure 3.16, optical attenuation bands are clearly presented, while the overall intensity is smaller in comparison to the bare silica opal. This is contributed to the decrease in refractive index contrast between the silica spheres and their surroundings. The index of refraction ratio between silica and air is about 1.45 : 1. With nanotubes growth into the air gap, the contrast of refractive index decreases.

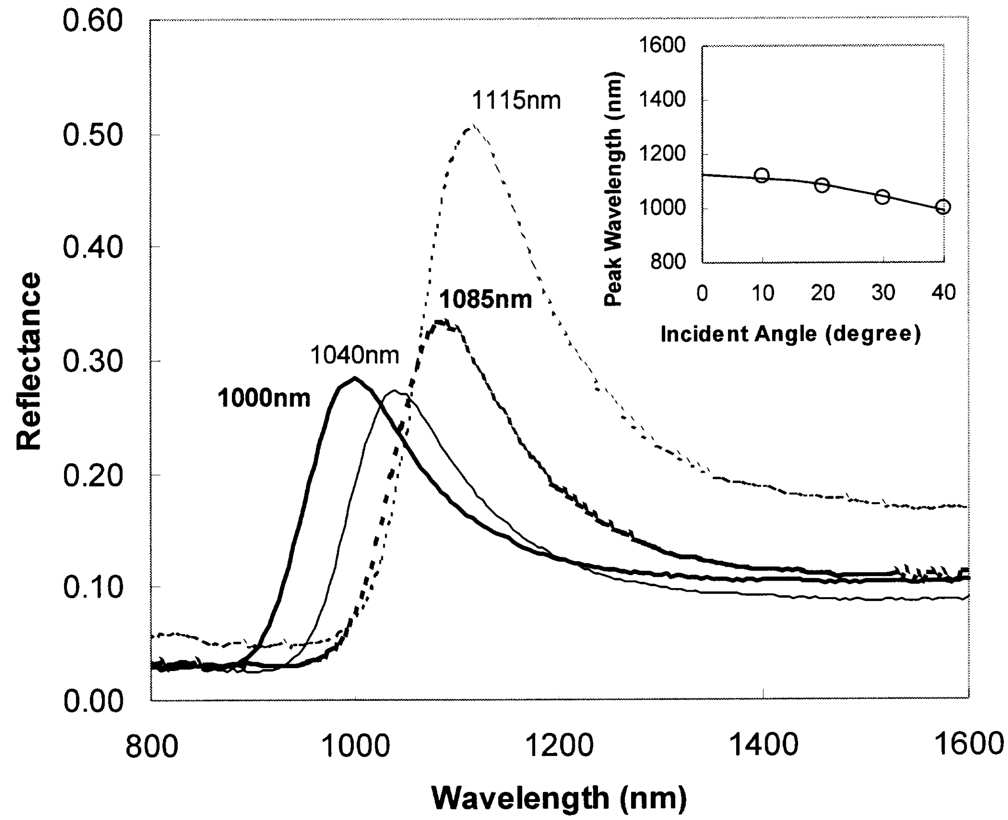

Figure 3.17 Reflection spectra of 503nm opal template embedded with SWCNT measured at different incident angles. From left to right, each curve corresponding to incident angle 40°, 30°, 20°, and 10°. The inset shows the angular dependency of reflection peak position. Hollow circular marks represent experimental peak wavelength measured at different incident angle; the solid line represents the theoretical function of Bragg law (Equation 2.10).

Figure 3.17 shows strong reflectance peaks for the same sample recorded at different incident angles. As the angle increases, the optical band moves to the lower wavelength, revealing a dependency of the band position on the incident angle. The inset of Figure 3.17 shows the relationship between the reflection peak wavelength (λ) and incident angle (θ). A close match between the theoretical function $\lambda(\theta)$ of Bragg Diffraction law (Equation 2.10) and experimental data is the evidence of that the 3-D periodic structure of opal template was intact even after the CVD procedure and with single-wall carbon nanotubes grown inside the template. From the optical band position, the effective index of refraction of this composite can be estimated. Based on the best-fit Bragg function shown in the inset, $n_{eff} = 1.369$, compared to $n_{eff} = 1.348$ for bare opal.

3.2.3 Raman Spectrum

The quality of the SWCNT produced by single-catalyst CVD process has been examined by Raman spectroscopy with a 488 nm (2.55 eV) Argon ion laser and an 830 nm (1.50 eV) AlGaAs diode laser. The low-frequency RBM Raman shift is the most selective to the diameter and chiral structure of the nanotubes. Figure 3.18 shows the lower frequency spectra excited by 830 nm laser. Several different spots on the sample have been measured and all Raman shifts represented by significant peaks were recorded and listed in Table 3.5.

The RBM frequency of Raman scattering is reversely proportional to the diameter of the carbon nanotubes, as shown in Equation 2.13 (b), $\varpi_{RBM}(d_t) = \frac{C_1}{d_t} + C_2$, with C_1 = 223.5 nm·cm^{-1} and C_2 = 12.5 cm^{-1} which were calculated by Bachilo, *et al.* [139]. The diameter of SWCNT corresponding to each distinct RBM frequency ω_{RBM} can be calculated, as shown in Table 3.5. Then base on the estimated diameter, the most possible chiral vector (n, m) can be assigned to that tube according to equation

$$d_t = \frac{L}{\pi} = \frac{a\sqrt{n^2 + m^2 + nm}}{\pi} \tag{3.11}$$

where a is the lattice constant and equals to $1.44 \times \sqrt{3}$ Å.

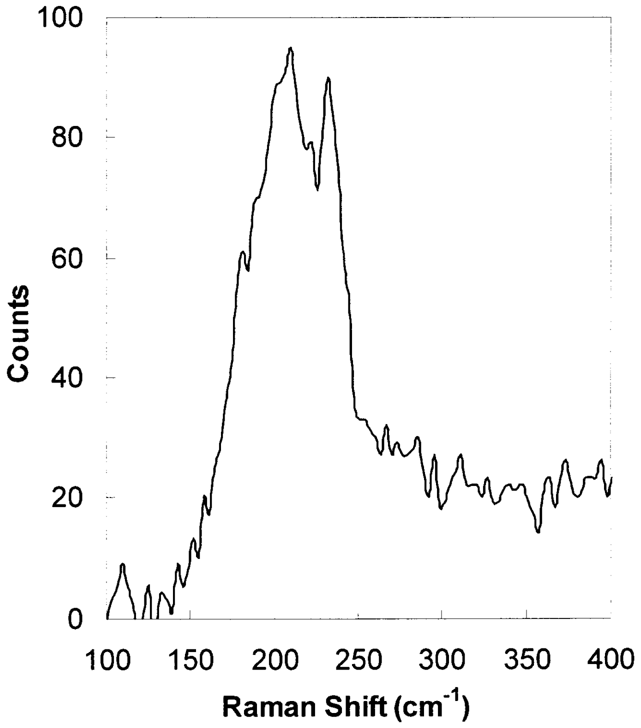

Figure 3.18 Low frequency Raman spectrum of SWCNT imbedded in silica opal template. The spectrum obtained was excited at λ = 830 nm (E_l = 1.50 eV) with a GaAs diode laser. The inset shows the low frequency Raman lines.

Table 3.5 Possible Chirality and Diameter of SWCNT

RBM frequency Exp. (cm^{-1})	**Estimated diameter d_t (nm)**	**Chiral vector (n, m)**	**Calculated Raman shift (cm^{-1})**
232.47	1.016	(11, 3)	233.25
229.27	1.031	(8, 7)	229.30
222.89	1.062	(11, 4)	221.99
216.48	1.096	(8, 8)*	215.90
210.06	1.131	(11, 5) *	211.29
203.64	1.169	(9, 8)	203.82
200.41	1.189	(11, 6)	201.24
197.20	1.210	(12, 5)	198.75
187.51	1.277	(13, 5)	187.63

By analyzing of RBM Raman spectra, it is estimated that the size of single-wall carbon nanotubes produced by CVD is in the range of 1.01-1.27 nm. The assigned chiral index reveals that the majority of the carbon nanotubes are semiconducting tubes. The two possible chiral vectors assigned belong to metallic tubes and are noted with asteroid marks.

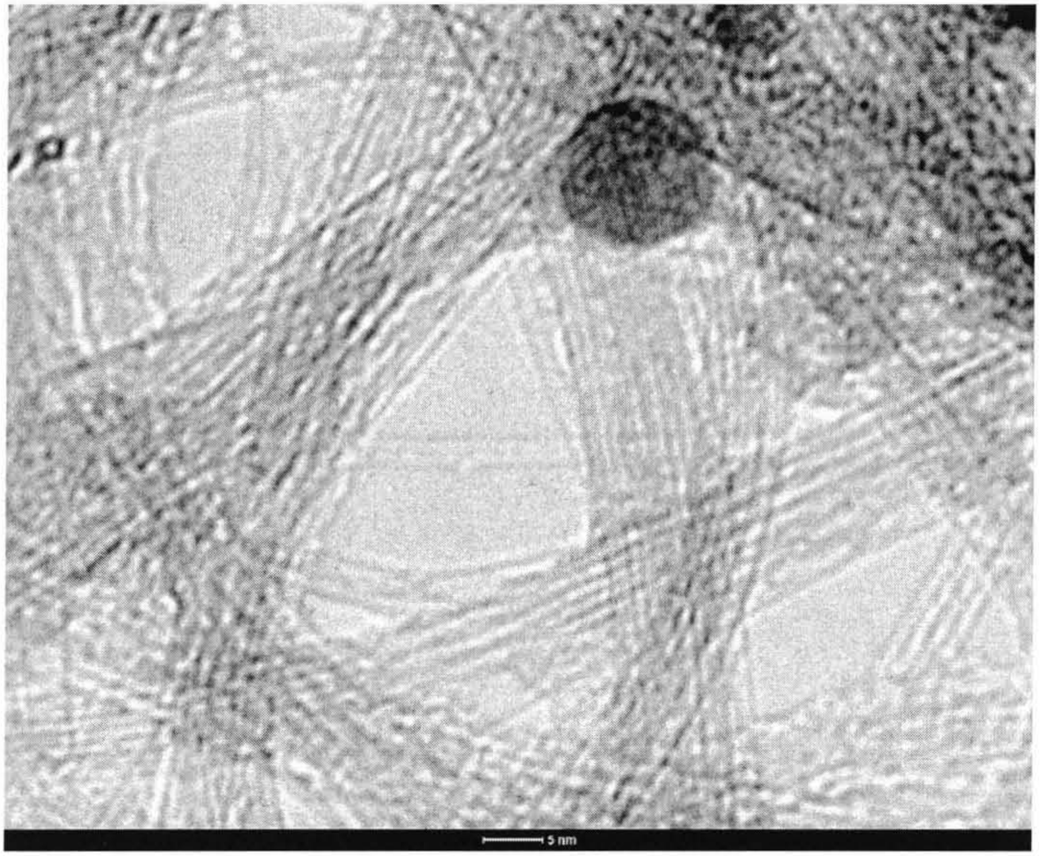

Figure 3.19 TEM image of single-wall carbon nanotube bundles.

The estimated range of tube diameters has been verified by transmission electron microscopy. A TEM image of single-wall carbon nanotube bundles (Figure 3.19) reveals an average tube size of 1.2 nm. The measurement was conducted with a LEO 922 Omega EF-TEM at 200 KeV.

Compared to the results of Lan, *et al.*, which exhibit tube diameter range of 0.7-0.9 nm when 700 °C deposition temperature was used [54, 135], it is suggested that a higher growth temperature (750 °C) produced single-wall carbon nanotube with larger diameter when the same catalysts were used. This situation may be explained by the probability for generating a pentagon rings [140]. When the temperature is lowered, the probability of closing a carbon pentagonal ring increases, and thus the caps which are generated tend to be smaller. At a higher temperature, however, atomic vibrations prevent formation of the relatively unstable pentagonal rings compared with hexagonal rings. Therefore, the lower growth temperature favors the growth of smaller diameter tubes. This thermal effect has been demonstrated by comparing the SWCNT grown at 750 °C in this research work with those grown by 700 °C CVD process.

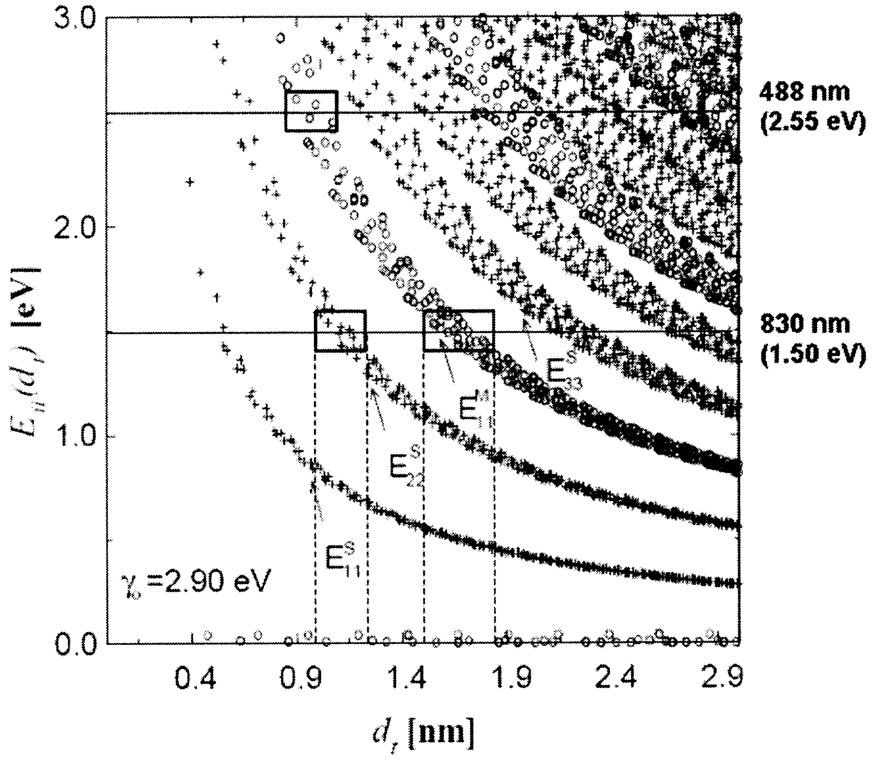

Figure 3.20 Kataura plot [71] revealing calculated energy separations $E_{ii}(d_t)$ versus nanotube diameter d_t for all chiral structure of single-wall carbon nanotubes. Semiconducting tubes are indicated by crosses and metallic tubes are indicated by open circles.

The possible diameters and chiral structures assigned to the single-wall carbon nanotubes have been corroborated with Kataura's theoretical calculations. Figure 3.20 shows the Kataura plot [71] and presents the calculated energy separations $E_{ii}(d_t)$ versus nanotube diameter d_t for all chiral structure (n, m) of carbon nanotubes. The energy levels of 830 nm (1.50 eV) and 488 nm excitation lasers are denoted by horizontal solid lines in the plot. Resonant windows corresponding to ± 0.1 eV of laser energies are plotted for semiconducting tubes and metallic tubes in the diameter range of 0.9-1.9 nm. The nanotubes predicted to be resonant must have transition energy between the van Hove singularities, i.e. E_{ii}, within the resonant window of excitation energy $E_l \pm 0.10$ eV [141]. It can be seen that the semiconducting tubes with diameter in the range of 1-1.24 nm and metallic tubes in a range of 1.5-1.84 nm are in resonance with the 830 nm laser. This result match the analysis of low frequency RBM Raman spectra which shows most of the nanotubes in the sample are semiconducting tubes with diameter of 1.01-1.27 nm, with little metallic tubes present.

High frequency Raman spectrum exhibiting the G-mode signal have been used to further evaluate the tubes in the sample. Figure 3.21 shows the high frequency Raman signals, including both D-band and G-band, recorded with 488 nm (2.55 eV) and 830 nm (1.50 eV) lasers, respectively.

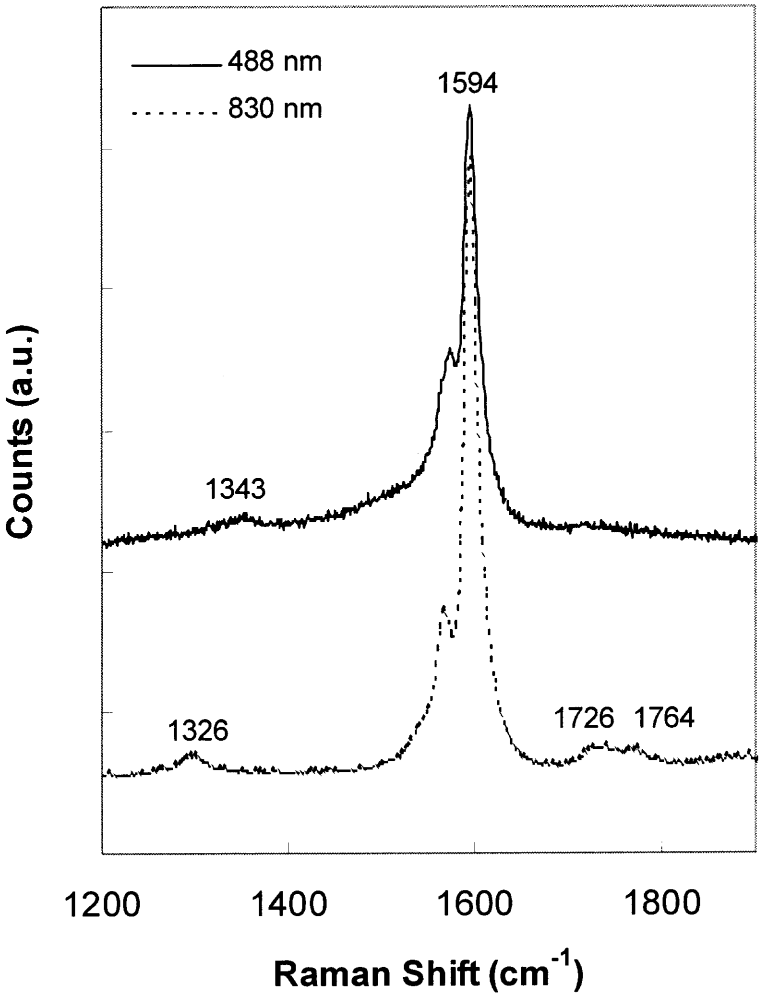

Figure 3.21 High frequency Raman spectrum of SWCNT grown by thermal CVD embedded in 3-D ordered silica template. The solid line represents the signal taken by 488nm Argon laser and the dotted line represents 830nm semiconductor diode laser. The spectra are offset for clarity.

The low intensity band of the D-mode at 1343cm^{-1} (488nm spectrum) and 1286 cm^{-1} (830nm spectrum), which usually appears in the Raman spectrum of SWCNT bundle and sensitive to the excitation laser energy [142], demonstrates a very small amount of structure defects or amorphous carbon presence. A Lorentzian lineshape fitting analysis has been performed on the G-band and the results are shown in Figure 3.22. The Raman band associated with the tangential C-C stretching modes of single-wall carbon nanotubes can be fit by four Lorentzian peaks at 1522, 1570, 1594, 1602 cm^{-1} for 488 nm laser and 1542, 1564, 1594, 1601 cm^{-1} for 830 nm laser. It is obvious that both spectra are dominated by strong peaks at 1594 and 1601 cm^{-1}. There is no significant shift observed between the two different excitation energies. The spectrum obtained with 488 nm (2.55 eV) laser exhibits an asymmetric Raman peak compared to the one with 830 nm (1.50 eV) laser. This asymmetric shoulder is identified as a broad Lorentzian peak at 1522 cm^{-1} in 488 nm spectrum, as well as an almost negligible component at 1542 cm^{-1} for the 830 nm spectrum. This broad shoulder suggests the presence of metallic nanotubes that are in resonance with the laser excitation energy. With 2.55 eV laser excitation, the resonant window for metallic tubes is 0.83-1.13 nm (refer to Figure 3.20, Kataura plot). This overlaps with the range of sample size, 1.01-1.27 nm, which is determined by low frequency RBM Raman shift. These metallic tubes have been identified as (8, 8) and (11, 5) with calculated diameter of 1.1 nm and 1.13 nm (refer to Table 3.5). However, with a 1.50 eV excitation laser line, only larger size tubes (1.5-1.84 nm) may exhibit a resonance behavior. The G-band excited by 830 nm laser therefore exhibits a narrower and symmetric peak.

In Figure 3.21, the faint Raman peak at ~1750 cm^{-1} is associated with a second-order Raman process involving the combination of the radial breathing mode and the tangential modes. The presence of this second-order Raman signal is also a signature of single-wall carbon nanotubes [143].

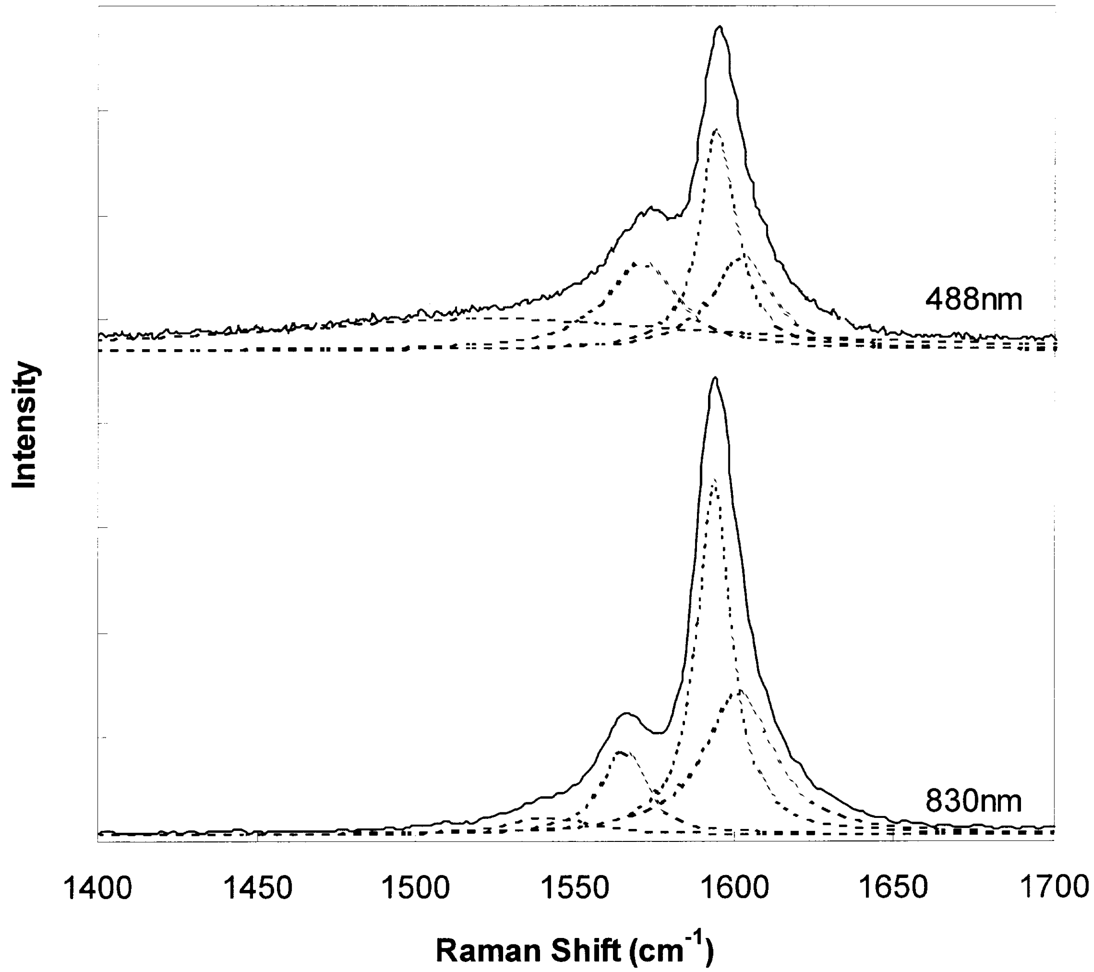

Figure 3.22 Lorentzian lineshape analysis of G-bands of Raman spectra taken by 488 nm and 830 nm laser.(488-1522.6, 1570.8, 1594.6, 1602.1; 830 – 1541.9, 1564.9, 1593.5, 1601.1)

3.2.4 Optical Activity

Based on the RBM Raman spectrum, the assumption is that most nanotubes in our sample have chiral symmetry (refer to Table 3.5). Optical activity has been used in order to identify such chirality. Experiments have been carried out as outlined in Section 2.4.3. Results are shown as a comparison between silica opal templates embedded with or without single-wall carbon nanotubes.

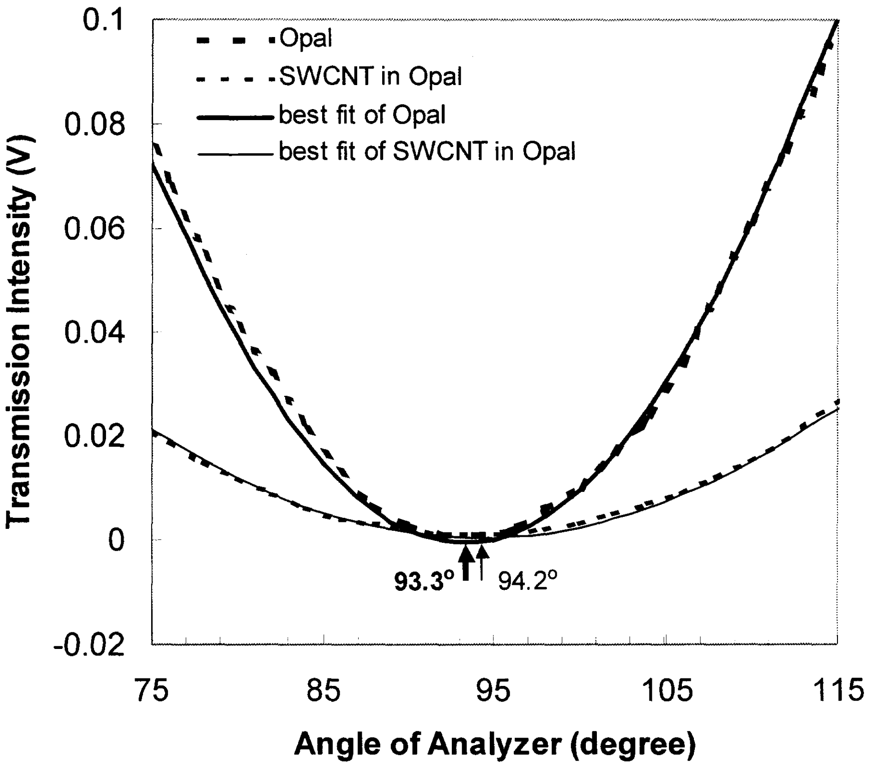

Figure 3.23 Optical activity measurement on SWCNT embedded in 3-D ordered silica opal template.

Figure 3.23 shows the transmission intensity of a polarized He-Ne laser. The thick doted line represents data of the bare opal template and the solid line is the best fit of Equation 2.11 with $I = 0.74\cos^2(\varphi - 3.3) - 0.00042$ and R^2 = 0.99864 (coefficient of determination). It means that when the analyzer's axis alignment angle equals to 93.3°, it blocks all transmitted light. In the same plot, the thin dotted line represents the sample embedded with carbon nanotubes and the solid line is the best fit function, $I = 0.19\cos^2(\varphi - 4.2) + 0.00037$ with R^2 = 0.99979. This means that 94.2° rotation of analyzer axis blocks the incident polarized light.

Comparing the best-fit results, the sample with nanotubes grown inside the silica opal template exhibits an unexpected optical activity effect. Although most of the as-grown carbon nanotubes have chirality, they are expected to be tangled together randomly. In addition, the tubes with same diameter maybe achieved by left and right handed chiral vectors (*n*, *m*). There should not be a preference in the growth of left or right handed tubes. The overall effect of the random chirality should not represent any optical activity. This surprising result is still under investigation.

3.2.5 Electrical and Photoelectronic Properties

Current-voltage characterization of the single-wall carbon nanotube interconnected networks imbedded in a 3-D silica opal template has been conducted at room temperature with 3 mm gap between two beryllium copper electrodes. The I-V curve shown in Figure 3.24 reflects good ohmic contacts between electrodes and nanotubes, as well as on the tube-tube interface throughout nanotube networks.

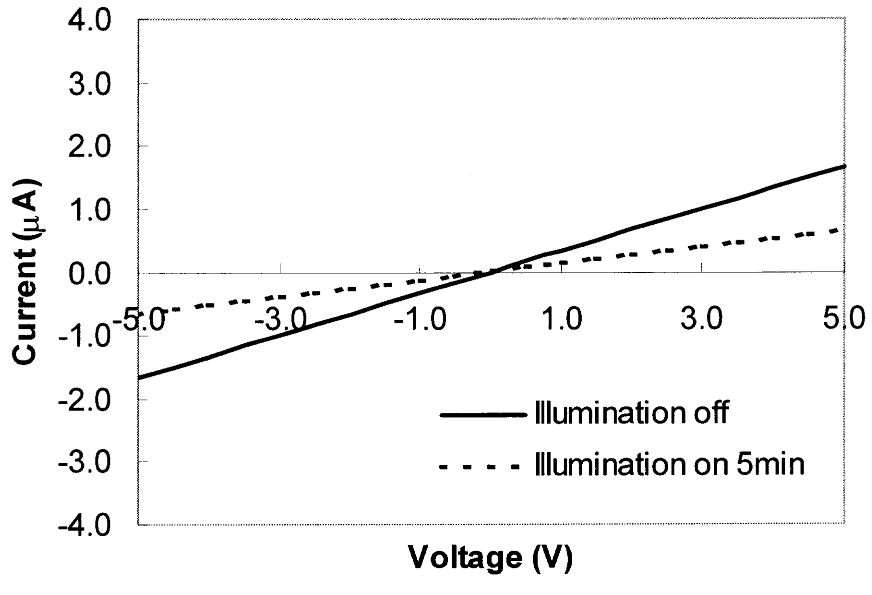

Figure 3.24 I-V curve of SWCNT embedded in silica opal template. The solid line represents the measurement conducted in dark; the dotted line represents the results with 5 minutes illumination (I = 0.25 W/cm^2).

The conductivity change of the carbon nanotubes embedded in opal template upon white light illumination is also shown in Figure 3.24. The conductance exhibited a dramatic decrease of 60% in a short time of 300 seconds. This photon induced conductivity decrease has been well studied either on individual SWCNT or nanotube films [144, 145]. This is due to UV-induced photodesorption of oxygen from the as-grown, oxygen doped and hence p-doped nanotubes.

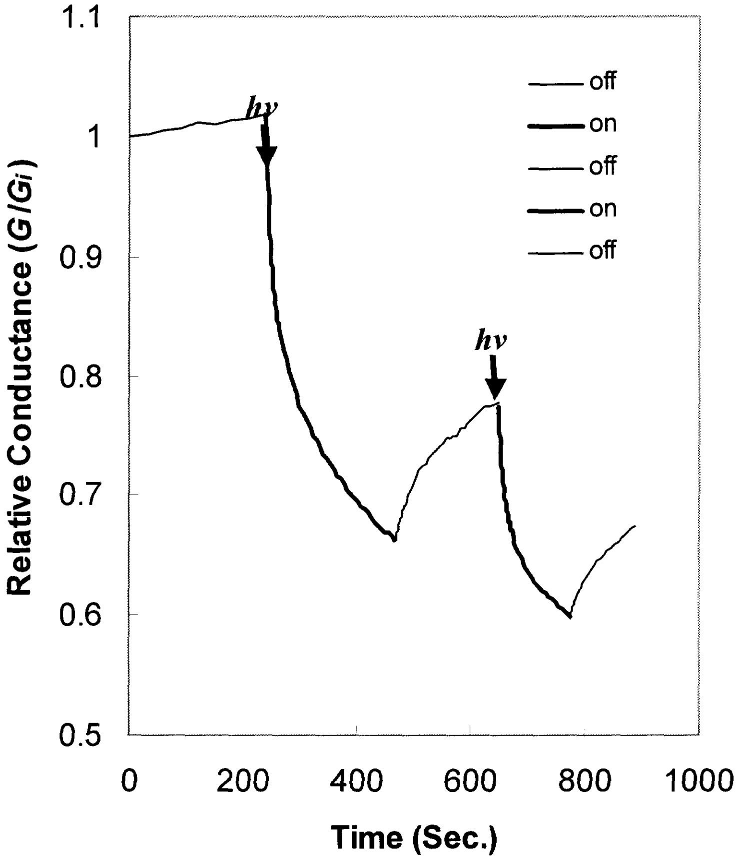

Figure 3.25 Normalized conductance of SWCNT network embedded in silica opal template versus time during UV illumination cycles (OFF/ON) in air. The intensity of UV illumination is about 11 mW/cm^2.

Figure 3.25 shows the normalized conductance change of SWCNT network under UV illumination cycles at room temperature and in ambient atmosphere. The initial conductance (G_i) of the sample is (40 KΩ/cm)$^{-1}$. The ratio of conductance change is plotted versus illuminating time. A slightly increase of the conductance was observed before the experiment has started and while the sample was in darkness condition. This may be because the sample had been stored in a well-illuminated laboratory environment. After a fast decrease in conductance within a short time under UV radiation, a following dark condition led to a slow recovery of conductivity. Direct thermal heating can be ruled out as the reason for this response. Direct heating of single-wall carbon nanotube mats results in a slow current reduction [146]. In addition, only very low radiation intensity is involved, which is down to 11 mW/cm^2 after a UV high pass filter is used.

The UV light pass through the filter has energy larger than 3.1 eV (400 nm), which is the energy usually required for $\pi-$electron plasmon excitation in carbon nanotubes. A broad and strong optical absorption peak around 4.7 eV in carbon nanotubes is contributed to this effect. It is possible that photoexcited plasmon in SWCNT are responsible for oxygen desorption [145].

3.3 Polymeric Inverse Opal

Polymeric inverse opals have been fabricated by infiltration of silica opal templates with *in situ* polymerized polymers, including PMMA and PVK compounds, and then selectively etching away the silica template by hydrofluoric acid. The quality of *in situ* polymerized PMMA and PVK inverse opal films were examined by FTIR and UV absorption spectra. The structure and optical properties of the polymeric inverse opal have also been identified.

3.3.1 Structure of PMMA Inverse Opal

Methyl methacrylate was infiltrating the silica opal template and polymerized by thermal induced polymerization of methyl methacrylate. The result of the *in situ* polymerization process was evaluated by FTIR spectrometer. Figure 3.26 shows the FTIR spectrum of the resultant PMMA inverse opal compared with PMMA standard spectrum. The excellent match between the two spectra demonstrated the good quality of infiltrated polymers.

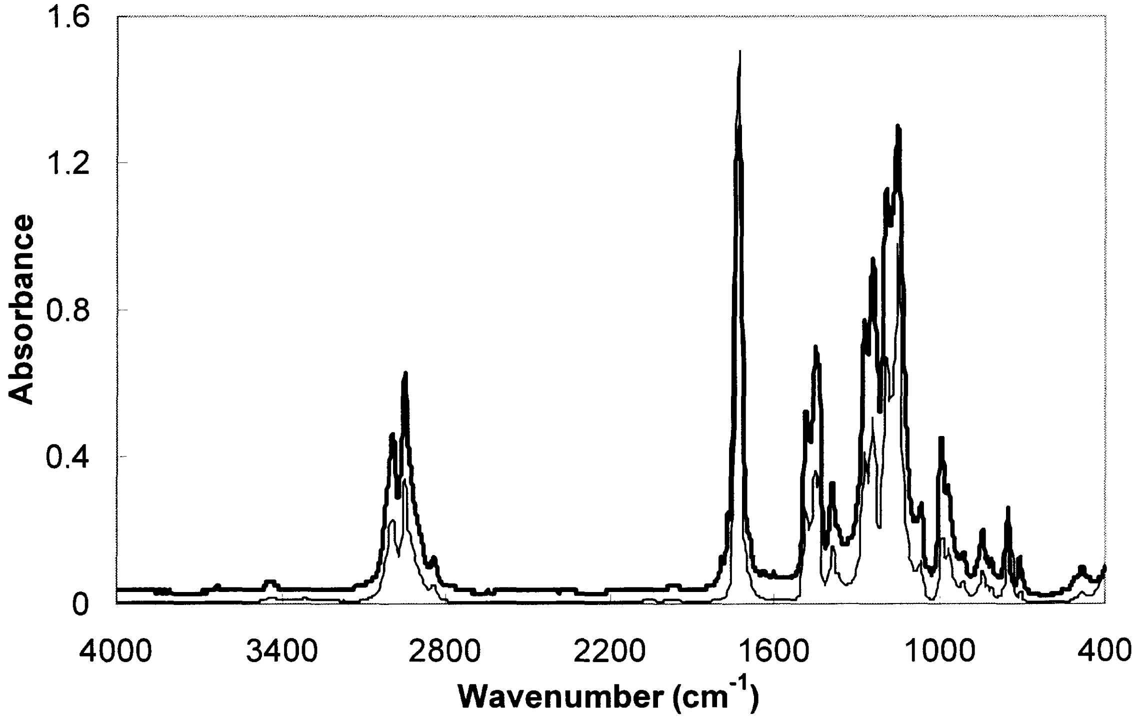

Figure 3.26 FTIR absorbance spectrum of PMMA inverse opal film made by *in situ* polymerization.

Figure 3.27 shows striking colors from porous PMMA thin film. It is a structural inverse replica of a silica opal template made of 503 nm silica spheres. The color is due to Bragg diffraction from the (111) planes. The SEM image of this porous film is shown in Figure 3.28, in which the close packed empty spheres with PMMA shell around them can been seen. Inside each air chamber there are three openings connecting each sphere with the other three neighbor spheres underneath. These channels played an important role in chemical etching by providing conducts through which the silica is washed away. The average size of these channels is usually one tenth of the air spheres and those shown in this image are about 50 nm.

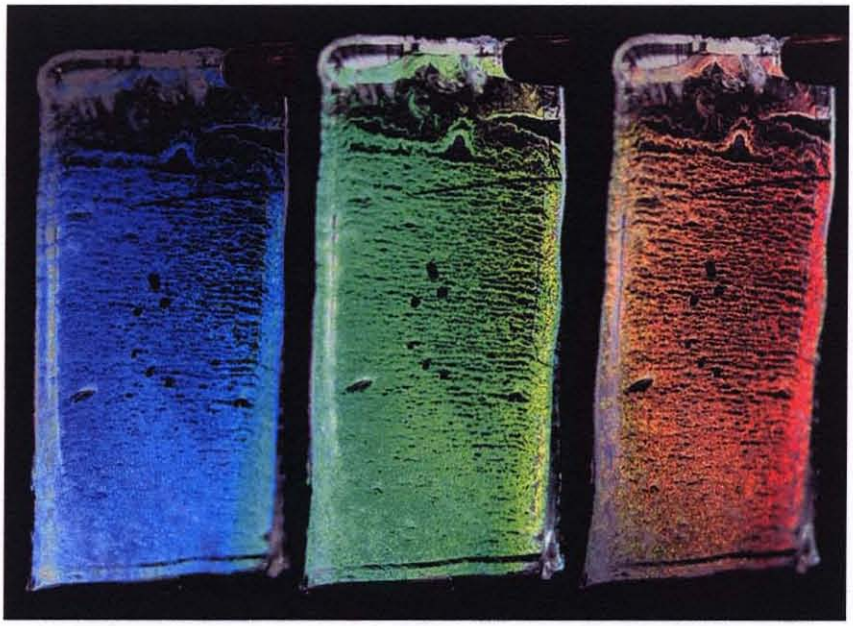

Figure 3.27 Iridescent PMMA inverse opal film.

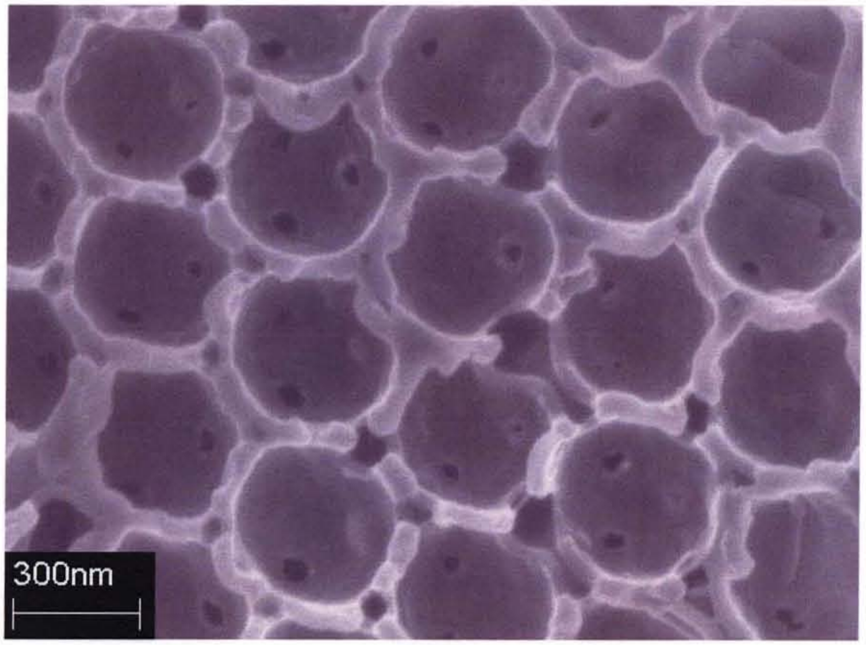

Figure 3.28 SEM image of PMMA inverse opal.

3.3.2 Optical Spectrum of PMMA Inverse Opal

Theoretically, the porous PMMA inverse opal film has a regular fcc close-packed lattice of air spheres embedded in PMMA. The effective index of refraction can be calculated by Equation 2.5, which is $n^2_{\mathrm{eff}} = n^2_{\mathrm{PMMA}} f_{\mathrm{PMMA}} + n^2_{\mathrm{air}} f_{\mathrm{air}}$ in this case. With the filling factor 74% for air and 26% for PMMA, and the index of refraction for these two components, $n_{\mathrm{air}} = 1$ and $n_{\mathrm{PMMA}} = 1.49$, respectively, the theoretical effective index of refraction for this PMMA inverse opal is $n_{\mathrm{eff}} = 1.148$.

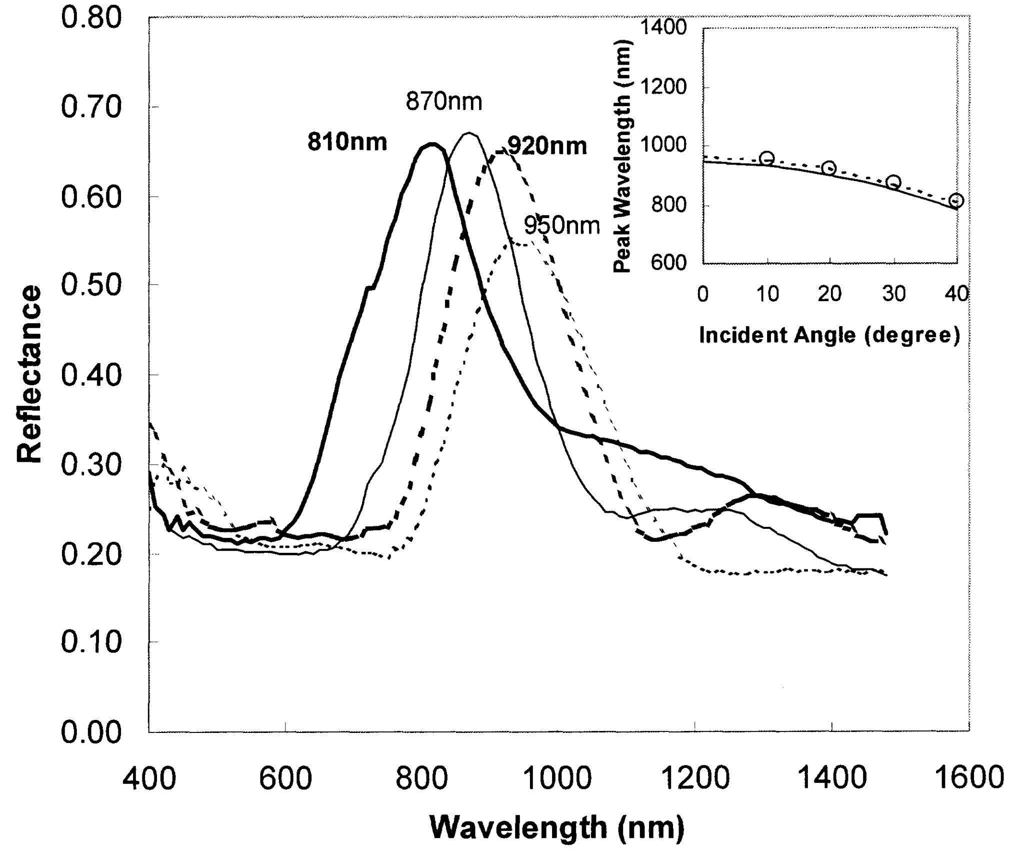

Figure 3.29 Optical reflection spectra of 503nm PMMA inverse opal measured at different incident angles. From left to right, each curve corresponding to incident angle 40°, 30°, 20°, and 10°. The inset image shows the angular dependency of reflection peak position. Hollow circular marks represent experimental peak wavelength measured at different incident angle; the solid and dotted line represent the theoretical function of Bragg law (Equation 2.10) with different n_{eff} value.

To verify the existence of 3-D crystalline structure in the polymer replica and its theoretically calculated effective index, vis-NIR optical reflection spectrum has been taken at different incident angles. Figure 3.29 shows strong reflectance peaks for the 503 nm air spheres embedded in PMMA film. It is evident that the regular fcc structure remained in this polymeric replica. At the same time, as the incident angle increases, the optical band shifts to shorter wavelengths, revealing a dependency of the band position on the incident angle. The inset of Figure 3.29 shows the relationship between the reflection peak wavelength (λ) and incident angle (θ), which may be used to verify the calculated n_{eff}. While the circular marks represent the experimental position of reflection peaks, the solid line is the theoretical function $\lambda(\theta)$ based on Bragg law (Equation 2.10) with $n_{\mathrm{eff}} = 1.148$. There is a noticeable discrepancy between the experimental data and the theoretical function (solid line), which is caused by an actually higher effective index of refraction than 1.148. The dotted line in the inset presenting a better fit is Bragg function $\lambda(\theta)$ with $n_{\mathrm{eff}} = 1.176$. This higher than expected refractive index may attribute to leftover of silica, about 8 vol.%, not thoroughly removed by chemical etching. Such leftover may be the result of crystalline defects in the original opal template.

3.3.3 UV Absorption of PVK Inverse Opal

With 20 wt% addition of plasticizer ECz in VCz, the *in situ* polymerization process was slowed down, as discussed in Section 2.3.2. To determine if the polymerization has been completed, the most straightforward way is to observe the liquid monomer cured completely to a solid polymer at 70 ^{o}C. For more accurate identification, UV-vis transmission spectrum of the polymerized sample is analyzed because there are different UV absorption bands for VCz and PVK, respectively. Usually, the UV absorption of PVK peaks at ~340 nm and decreases fast beyond 350 nm, while around 355 nm is the peak absorption of the monomer VCz [147]. Figure 3.30 shows the UV absorption spectra comparison between PVK obtained by *in situ* polymerized and commercial product respectively from Aldrich. The –log (I_T/ I_0) is used to represent the light intensity loss, where I_T is the transmitted light intensity and I_0 is the incident intensity. The spectrum indicates that the *in situ* polymerization of VCz to PVK was not completed when the absorption was taken. Although the peak absorption of PVK at 344 nm is present, there is still noticeable peak absorption at 356 nm from monomer VCz.

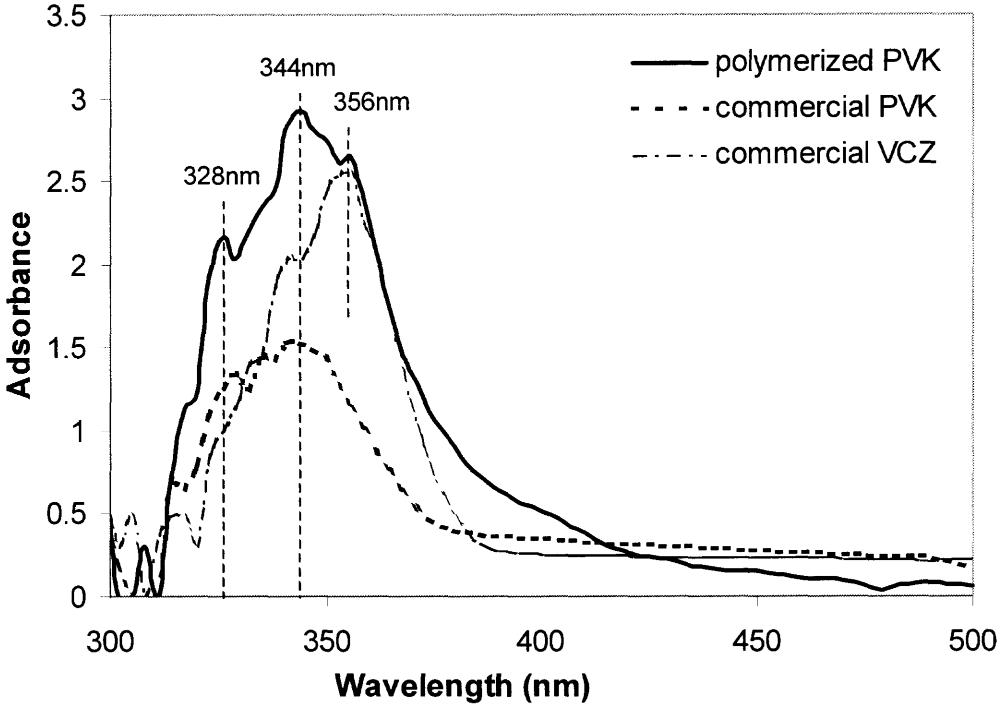

Figure 3.30 UV absorption spectra of PVK. The solid line represents the sample polymerized from NVC; the dotted line represents the commercial product from Aldrich.

3.4 Polymer–SWCNT Composites Inverse Opal

Nanostructured polymer-carbon nanotube composites have been synthesized by polymer infiltration into a silica opal template embedded with single-wall carbon nanotube. If the silica template is removed later, the resultant polymeric composite is a porous film with 3-D ordered and interconnected air spheres. In the following sections, the structural, optical and electric properties of these polymeric structures have been discussed.

3.4.1 Morphology of Polymer–SWCNT Composite

SEM image of the resulting PVK compound – carbon nanotube composite is shown in Figure 3.31. The image reveals a uniform infiltration of PVK complex into the voids between the silica spheres and consequently a coating on the embedded carbon nanotubes. Similar images have been achieved for PMMA infiltrated silica template with embedded carbon nanotubes.

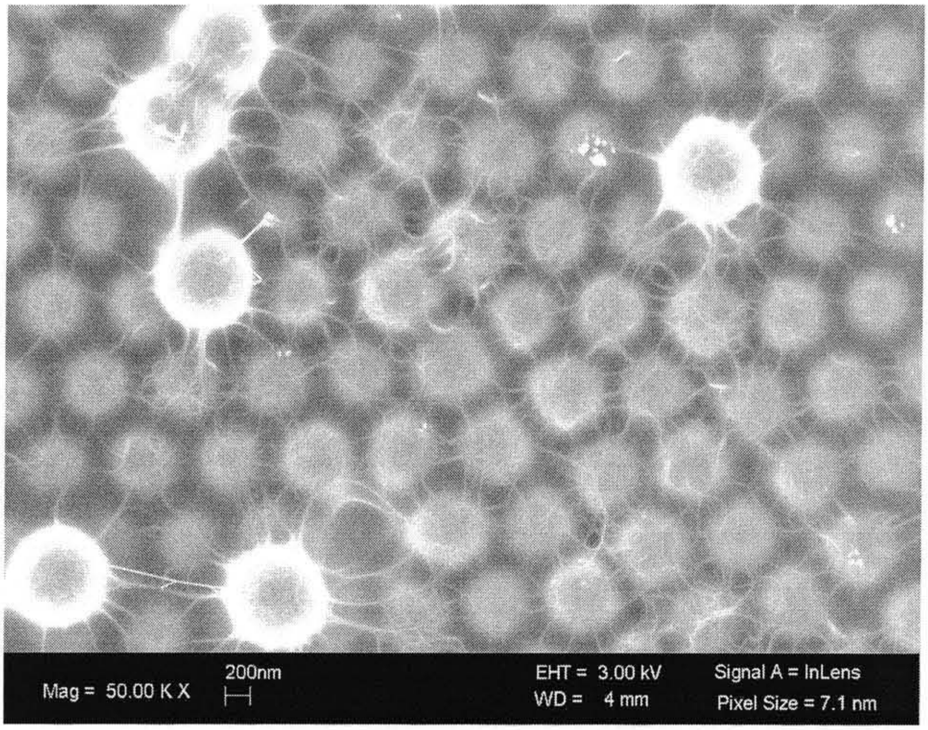

Figure 3.31 SEM image of Polymer–SWCNT nanocomposite before the silica opal template was etched.

It is evident from Figure 3.31 that polymer–SWCNT composite with uniform dispersion of carbon nanotubes has been formed in the 3-D ordered silica array. Following treatment with 10 wt% HF would selectively remove the silica spheres from the polymeric matrix and leave with a porous composite film with inverse opaline structure behind. The resultant freestanding porous membrane of polymeric carbon nanotubes composite features interconnected air chambers that allow a good permeation of gas of liquid. This feature may lead to promising applications of this porous material as chemical sensor because of its large interior surface area with exposed carbon nanotubes.

3.4.2 Optical Characterization

Linear optical refection spectrum of PMMA–SWCNT composite with inverse opaline structure is shown in Figure 3.32. As expected, strong reflection peaks from the porous composite film show blue shift with an increase of incident angles, according to Bragg diffraction law for crystalline structures. The inset of Figure 3.32 reveals the functional relationship between the diffraction peak wavelength and corresponding incident angles. The solid curve represents the function of $\lambda(\theta)$ with an estimated value of effective index of refraction as 1.22. The good fit between this theoretical function and experimental data (circular marks) is noted.

With known filling factors of air (74%) and PMMA–SWCNT composite (26%) in the inverse opaline structure, the approximate value of refractive index of the composite itself can be evaluated. Follow Equation 2.5, the refractive index of the composite should be 1.697. PMMA composite inverse opal has a higher refractive index contrast than pure PMMA inverse opal and will show sharper and stronger optical reflection band due to Bragg diffraction.

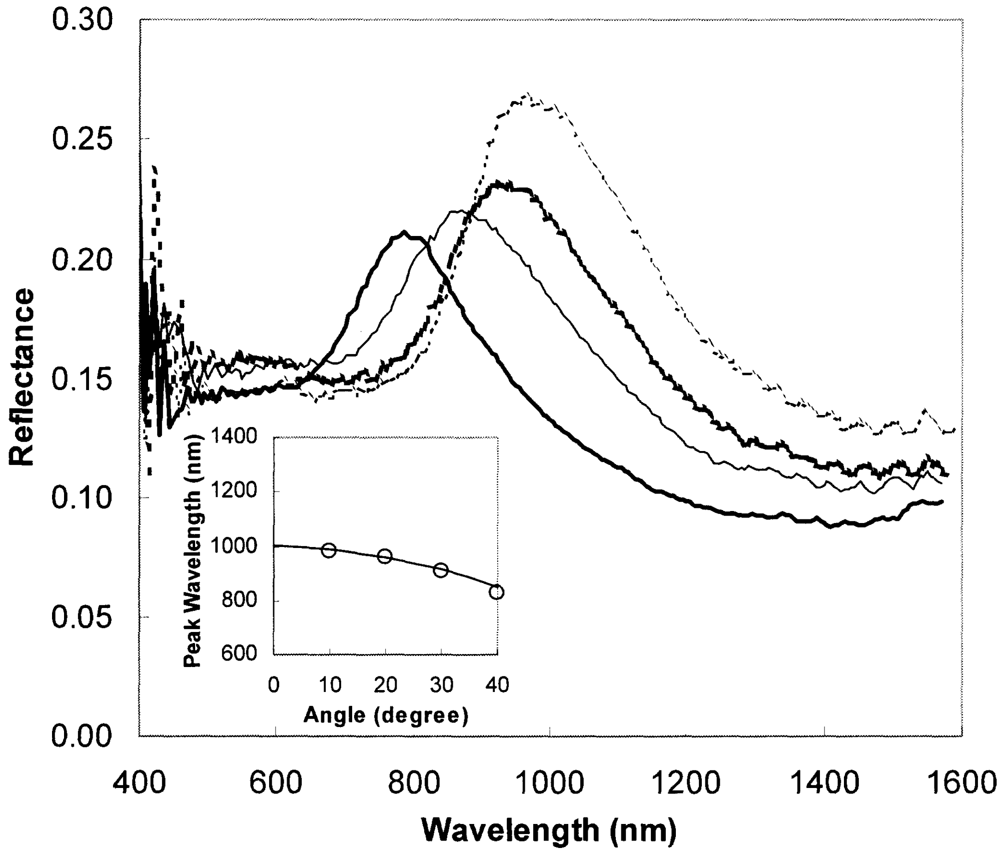

Figure 3.32 Optical reflection spectrum of PMMA–SWCNT inverse opaline structure. From left to right, each curve corresponding to incident angle 40°, 30°, 20°, and 10°. The inset image shows the angular dependency of reflection peak position. Hollow circular marks represent experimental peak wavelength measured at different incident angle; the solid line represents the theoretical function of Bragg law (Equation 2.10).

3.4.3 Raman Spectrum

Raman spectroscopy was used in studies of carbon nanotube and polymer based composites in order to identify nanotubes, assess their dispersion in polymer matrix, and evaluate nanotube-polymer interface and interactions. This is because when nanotubes interact with other materials, the Raman frequency, intensity and band shape of the molecular vibrations may change. For example, in polymeric carbon nanotube composite, stresses and changes in the charge due to oxidation or reduction of single-wall carbon nanotubes result in a shift of the tangential mode of frequency at ~1590 cm^{-1}. This is an important property with high impact on applications.

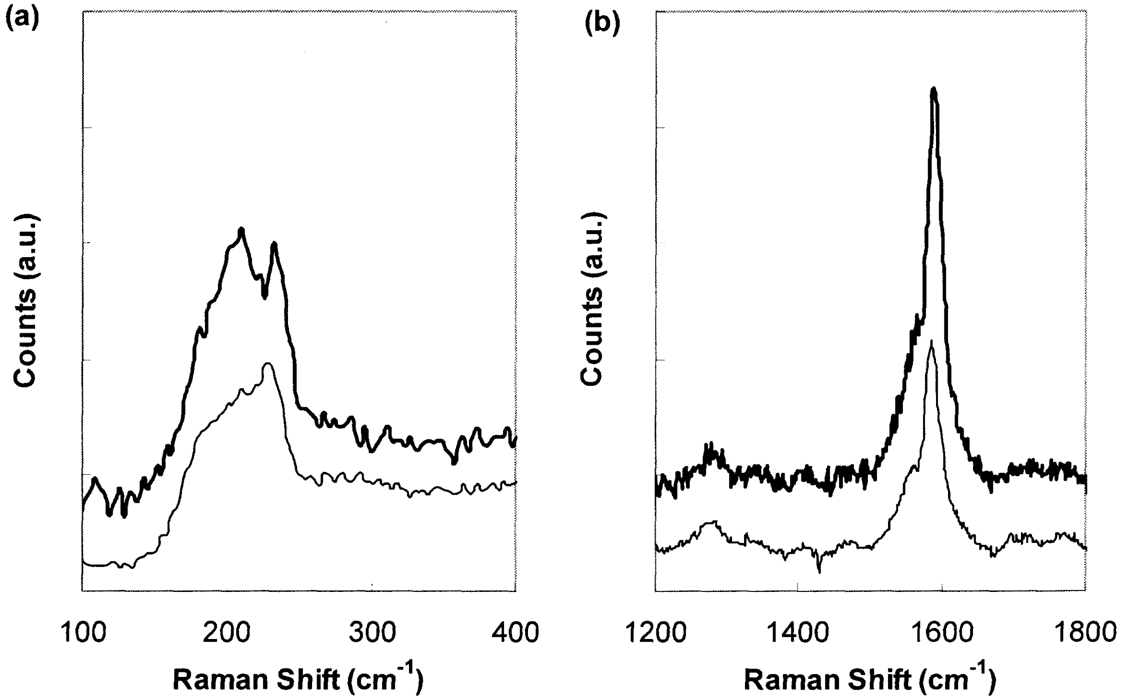

Figure 3.33 Raman spectra of PMMA–SWCNT composite. The thick line represents the pristine nanotube in opal template; the thin line represents PMMA/nanotube composite. (a) Low frequency Raman spectra; (b) High frequency Raman spectra. The Raman signals of two samples are offset intentionally for clarity.

Figure 3.33 shows the low frequency RBM-band and high frequency G-band Raman spectra of PMMA and carbon nanotube composite excited by 830 nm laser line. Both samples of single-wall carbon nanotubes coated with PMMA (the dotted line) and without PMMA (the solid line) have been measured. The spectra of these two samples have been offset for clarity.

Raman spectra of PVK complex and carbon nanotube composite have been taken with 830 nm laser excitation, as shown in Figure 3.34. The thick solid line represents the as-is single-wall carbon nanotubes embedded in silica opal and the thin line corresponding to the sample coated with PVK-ECz-DEH.

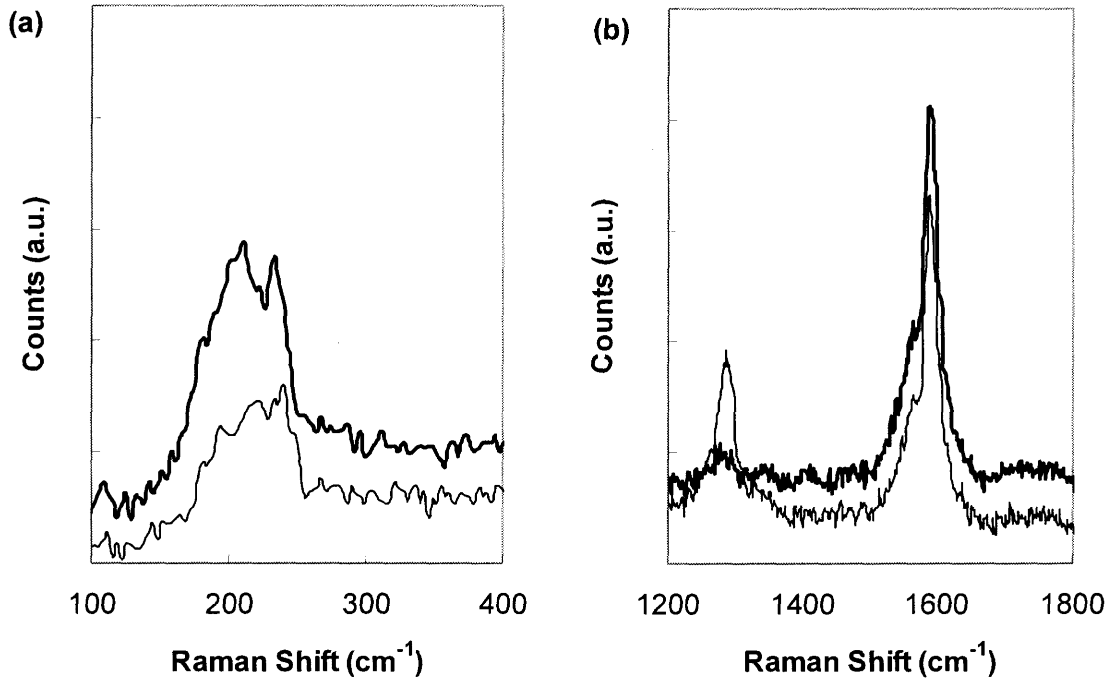

Figure 3.34 Raman spectra of PVK–SWCNT composite. The thick line represents the pristine nanotube in opal template; the thin line represents PVK–SWCNT composite. (a) Low frequency Raman spectra; (b) High frequency Raman spectra. The Raman signals of two samples are offset intentionally for clarity.

First, the discussion will focus on the RBM bands of these two polymeric composites. Compared to pristine single-wall carbon nanotubes embedded in opal template, the polymer composites, whether with insulating PMMA or with photoconductive PVK, exhibit a weakened intensity of resonant RBM signal and a slightly up-shift of the band frequency. The PVK–SWCNT composite shows a more noticeable band shift than the PMMA composite.

The frequency of RBM band is known to be sensitive to inter-tube interactions [148]. Upon polymers coating of the carbon nanotube bundles and probably even intercalating inside the bundles, a shift of the RBM is expected. Based on this assumption, the observed up-shift of RBM bands may be assigned to a stress applied by the intercalation of polymer into the bundles. The pressure exerted by polymer on individual tubes may increase the vibrational frequency of radial breathing mode [149]. This may explain PVK–SWCNT composite shows a larger shift than PMMA. PVK can form a more effective conjugated interaction with the nanotubes. An interface with a stronger interaction will exert a higher pressure on the tubes and result in a more significant change on the molecular vibration frequency.

The intensity weakening effect on RBM bands represented by polymer composites can be considered from two aspects. First, the coated polymer itself has a strong scattering effect that may weaken the excitation light before it reaches the embedded carbon nanotubes. Consequently, scattering from nanotubes will be weakened. Another possible reason may be associated with the loss of resonance effect due to charge transfer through the interface between polymer and nanotubes. This effect is almost impossible in PMMA. However, PVK has electron-rich pyrrole group and is easy to be oxidized. It is possible therefore that PVK acts as an electron donor to some degree and changes the electron density at the nanotubes interface. The loss of singularities in electronic density of state (DOS) because of electron fill-in may leads to loss of resonant Raman effect and weakened Raman signals.

In the high frequency range, the G-band in Raman spectrum of polymeric nanotube composite does not show noticeable shift, regardless of the PVK or PMMA matrices. An overall moderate weakening of the signal intensity is noted. This weakened stretching mode vibration may be explained similarly to the weakened RBM-band. Another difference between the PVK–SWCNT composite and pristine nanotube is an enhanced Raman signal of the D-band around 1280 cm^{-1}, which is associated with structural defects on the nanotube surface. The PMMA–SWCNT composite also exhibits this feature with consideration to the ratio between the D- and G-bands. This change has been observed in chemical doped SWCNT as well, which will be further discussed in Section 3.5.2.

3.4.4 Electrical and Photoelectronic Properties

Current – voltage characterization has been conducted on polymeric composites of PVK complex–SWCNT and PMMA–SWCNT. The load of carbon nanotube in these two samples was very close (~3 wt%). The conditions for the measurements were ambience atmosphere and room temperature. There was a 3 mm gap between the two beryllium copper electrodes contacted with the sample surface. Figure 3.35 shows the I-V curves of PMMA–SWCNT and PVK complex–SWCNT composites. Both composite materials exhibit a decreased conductivity after 5 minutes of light illuminations. The relative change of conductance is significantly different between PMMA and PVK composites. It is easy to estimate from the I-V curve that the PMMA composite suffered 40% loss of conductance value [Figure 3.35 (a)] after 5 minutes, while PVK complex composite kept almost 90% of its conductance value [Figure 3.35 (b)].

The conductance decrease of SWCNT networks embedded in opal template has been discussed in Section 3.2.5. It is contributed to UV induced photodesorption of oxygen from the nanotubes. The conductivity decrease in polymer–SWCNT composite can be well explained by the same mechanism. It is evident that the introduction of polymer into the SWCNT network suppressed the effects of conductivity decreased upon light illumination. For example, five minutes light exposure led to 60% loss of conductivity in pristine SWCNT (Figure 3.24 in Section 3.2.5), but only 40% loss after infiltration with PMMA. Protection of the polymeric coating seems to prevent or at least slow down the photoinduced desorption process of oxygen from carbon nanotubes.

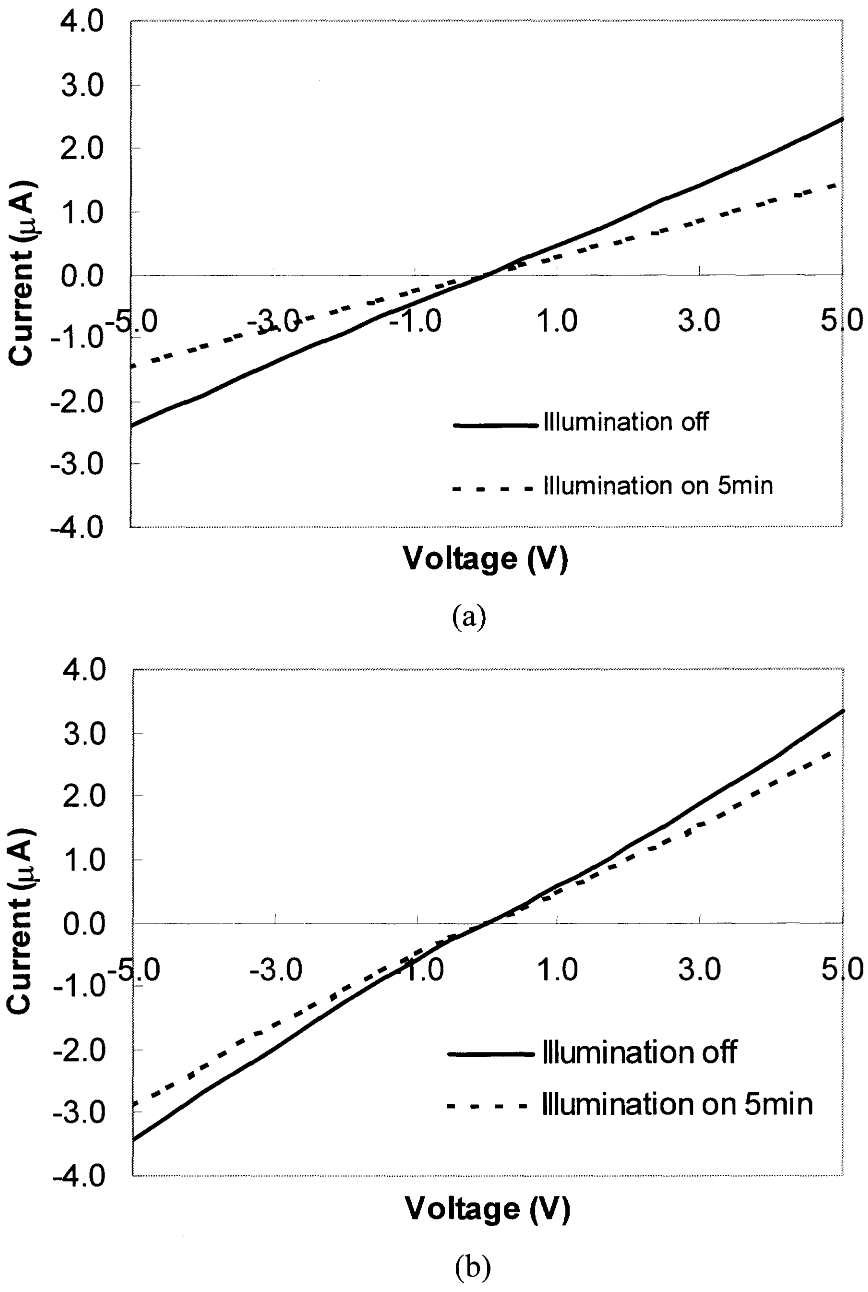

Figure 3.35 Current – Voltage characteristics of polymer–SWCNT composite film. (a) is for PVK composite and (b) is for PMMA composite

The overall polymer coating can help preventing conductance diminishing upon light exposure. Unlike PMMA, PVK is a well-known photoconducting polymer that exhibits a relatively high electrical conductivity when irradiated with visible or ultraviolet light. The simplest process of photoconduction occurs when a photon is absorbed and an electron is excited from the valence band to conduction band, if the photon energy exceeds the band gap. This process generates an electron-hole pair (EHP), and increase the concentration of charge carriers. PVK absorbs ultraviolet light below 350nm. The addition of DEH and ECz enhances the UV absorption of the polymer and improves the photoconductivity effects. Therefore, the photo-excited EHPs in PVK compound will compensate the depletion of charge carriers due to photodesorption of oxygen from the carbon nanotubes, leading to a much reduced conductivity effect upon UV irradiation.

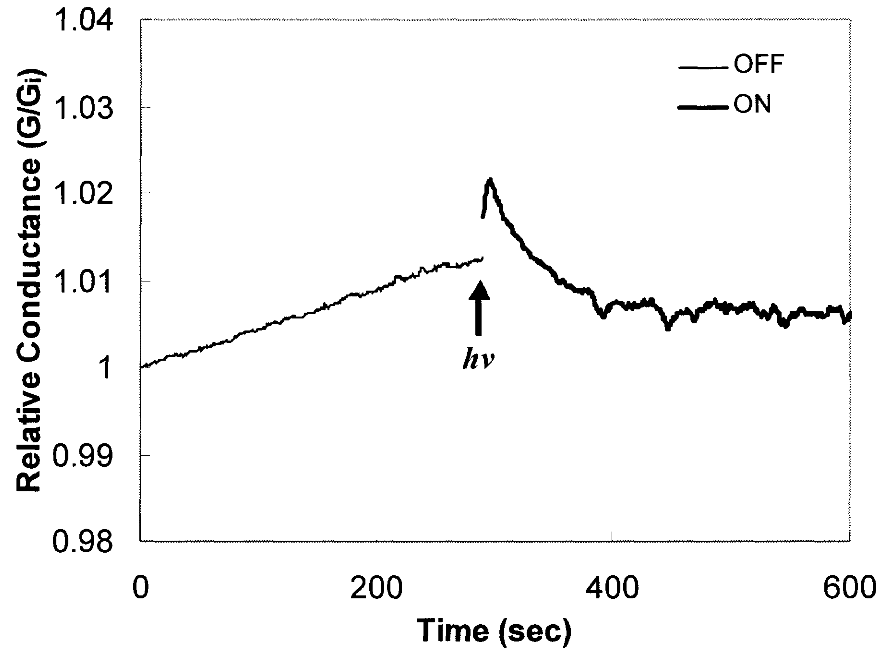

Figure 3.36 Normalized conductance of PVK–SWCNT composite embedded in silica opal template versus time during one UV illumination cycle (OFF/ON) in air. The intensity of UV illumination is about 11 mW/cm^2.

Figure 3.36 shows the normalized conductance change of a composite based on PVK complex and SWCNT when it undergoes a light illumination cycles of OFF and ON at room temperature and ambient conditions. The initial conductance (G_i) of the sample is about (6 MΩ/cm)$^{-1}$. The ratio of conductance change has been plotted versus illuminating time. This time dependency figure of conductance clearly shows an instant jump of conductance in PVK–SWCNT composite upon light exposure. However, the enhanced conductivity is sustained for several seconds. Then, a continuous decrease takes over and follows the trend of the conductance decrease under UV exposure. This short-term conductance increase is due to a fast photo-conductance response before the relatively slow oxygen photodesorption process takes place.

The same experiment has been performed with blank polymer complex of PVK-ECz-DEH. This photoconductive effect was not observed. No noticeable increase of conductance has been recorded. Generally, it is difficult to observe photo-conductance effect even when the sample is irradiated by photons with energy well above its band gap. This may be because the excited carriers have very short lifetime due to rapid recombination and deep hole trapping. In PVK complex and carbon nanotube composite, the presence of carbon nanotubes actually enhances the photoconducting effect. PVK has electron rich pyrrole moieties while pristine carbon nanotubes are oxidized hole-doping material. Consequentially a weakly bonded charge-transfer complex is highly possible to be assembled between PVK and nanotubes, which in turn enhances the photoconductivity of the complex dramatically. The Raman scattering spectrum of PVK–SWCNT composite discussed in previous section also suggested formation of charge-transfer interaction.

3.4.5 Nonlinear Optical Transmission

Nonlinear transmission measurements have been conducted with a Q-switched Nd:YAG laser operating at λ = 532 nm and 10 ns pulses. As noted in previous publications, an enhanced transmission is exhibited for these 3-D periodic structures at particular angle ("magic angle") when illuminated with 532 nm laser [150,151]. After conducting a measurement of transmission intensity versus incident angle, a resonant enhancement of transmission was recorded at ~20°.

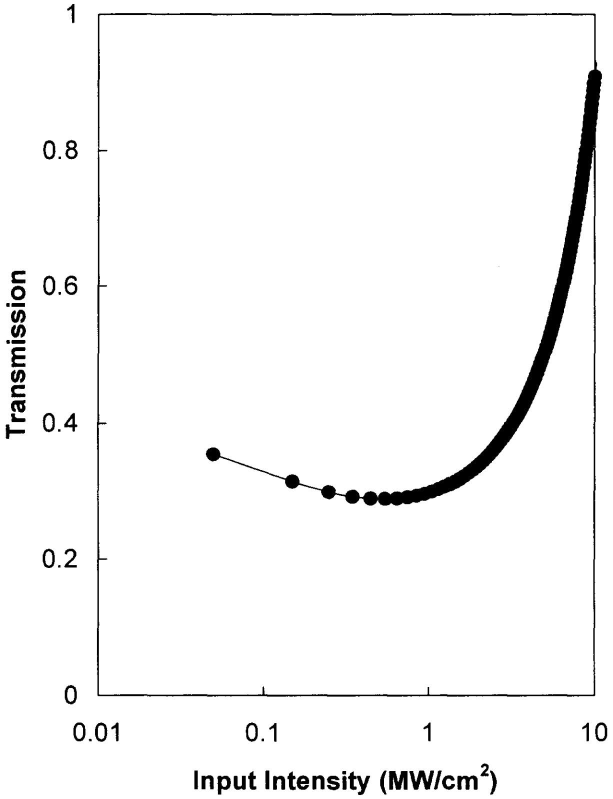

Figure 3.37 Nonlinear transmission of SWCNT in silica opal template. It is measured with λ = 532 nm at around θ = 20^0 for D = 580 nm spheres. The curve is a ratio between two sets of transmission data of silica opal template with and without the SWCNT.

The nonlinear transmission of pristine SWCNT grown in the voids of silica templates has been measured around this magic angle and is shown in Figure 3.37. The curve has been normalized to the transmission data of bare silica opal template.

Nonlinear characteristics of SWCNT coated with PVK-ECz-DEH and embedded in silica opal template are shown in Figure 3.38. The upper curve represents the output (in mV) as a function of input laser intensity for regular silica opal template. The lower curve is for the PVK–SWCNT composite embedded in the template. The normalized transmission of composite is presented as the ratio between above mentioned two sets of data and is shown in the inset of the figure.

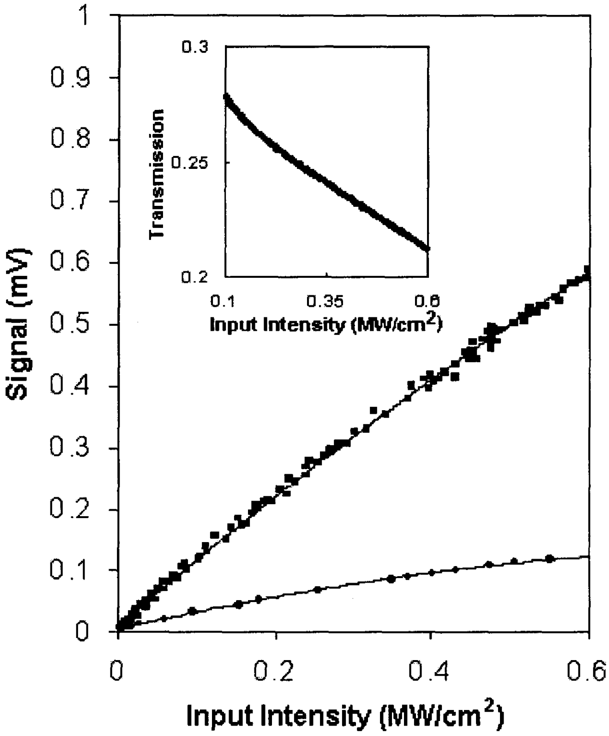

Figure 3.38 Nonlinear transmission of SWCNT in silica opal template coated with PVK complex. The square marks represents silica opal template while circle marks represent PVK complex coated SWCNT embedded in the template. The solid lines correspond to the best-fit functions.

The PVK-ECz-DEH compound is well known for it photorefractive effect at millisecond time scale. The optical sensitizer DEH can expand the absorption spectrum of polymeric composite from UV to visible range. The nonlinear absorption may be attributed to charge transfer between the SWCNT and the PVK at visible spectral range.

3.5 Distributed p-n Junction with 3-D Ordered Structure

The polymeric composites made from pristine single-wall carbon nanotube which have been discussed so far are p-type doped materials. This has been proven by thermoelectric properties of those composites. If the voids of these polymeric inverse opals be filled with n-type material, a regular distributed p-n interface will be formed.

3.5.1 Polymer Functionalized n-type SWCNT

The n-type single-wall carbon nanotubes have been obtained by surface modification of pristine carbon nanotubes with an amine-rich polymer, polyethylenimine (PEI). The carbon nanotubes have been used is CarboLex AP-grade (as-prepared) SWCNT which is commercially available. It is made by Arc method in specifically designed chambers. The average diameter of these nanotubes is 1.4 nm and are found in "ropes" which are typically ~ 20 nm in diameter or approximately 50 tubes per rope with lengths of 2-5 microns [152]. These AP-Grade nanotubes are not chemically treated or processed. Impurities include approximately 35 wt% residual catalyst (NI, Y) that is usually encapsulated in carbon shells. Amorphous carbon may also be found on the outer surfaces of the nanotube bundles. The purity of CarboLex AP-grade SWCNT is about 50-70% as determined by Raman spectroscopy.

The chemical modification procedure of making n-type carbon nanotubes has been conducted following reference [110]. Summarizing, 1 wt % as-is CarboLex SWCNT was mixed with a 10 wt% PEI (average molecular weight 60,000-1,000,000, Fluka) in ethanol. After several hours of sonication, a stable dispersion of carbon nanotubes was obtained that indicated the adsorption of PEI on the tube surface. The resultant suspension of carbon nanotubes went through four cycles of purification by centrifuge, separation and re-disperse in ethanol to remove excess PEI nonspecifically adsorbed on the nanotubes.

The simple thermoelectric characterization described in Section 2.4.6 has been conducted on the polymer functionalized carbon nanotube film. With the room temperature positive electrode and high temperature negative electrode, the thermal induced voltage across the film has a significant negative value. This is and evidence that PEI doped CarboLex nanotube is n-type material. The doped n-type material maintains its electric characteristics over months. This irreversible PEI doping not only overcomes the p-doping effect on the pristine carbon nanotube, it also prevents the further oxidation of nanotubes by the ambient storage condition. The highly efficiency of n-doping is explained by the ability of amine groups to donate electrons and the fact that polyethylenimine is one of the polymers containing the highest density of amine group. The molecular structure of PEI is shown in Figure 3.39.

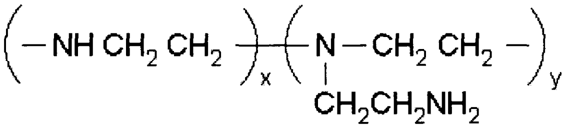

$$\left(-NH\,CH_2\,CH_2\right)_x\left(-\underset{\substack{|\\ CH_2CH_2NH_2}}{N}-CH_2\,CH_2-\right)_y$$

Figure 3.39 Molecular structure of polyethylenimine (PEI).

A film of PEI coated carbon nanotubes has been cast from its ethanol suspension. The SEM/EDS has been used to examine the morphology of the sample. Figure 3.40 shows the SEM image of the PEI–SWCNT mat. Much impurity exists in the polymer modified nanotubes. They are identified as cluster of amorphous carbon shell by EDX elemental analysis. Further purification of the commercial CarboLex AP-grade SWCNT is desired.

During the film formation, some cracks induced by the solvent dry-out. The SEM image of Figure 3.40(b) shows the oriented carbon nanotubes stretching across a crack. There are several spots in the image clearly showing the polymer coating on single or very small bundles of carbon nanotubes. The average size of PEI coated "ropes" is far less than 20 nm (the scale bar of the image), which is claimed by CarboLex on the as-prepared samples. So the PEI molecules not only modify the electric property of nanotubes, but also intercalate into the nanotube bundles and separated them into smaller groups.

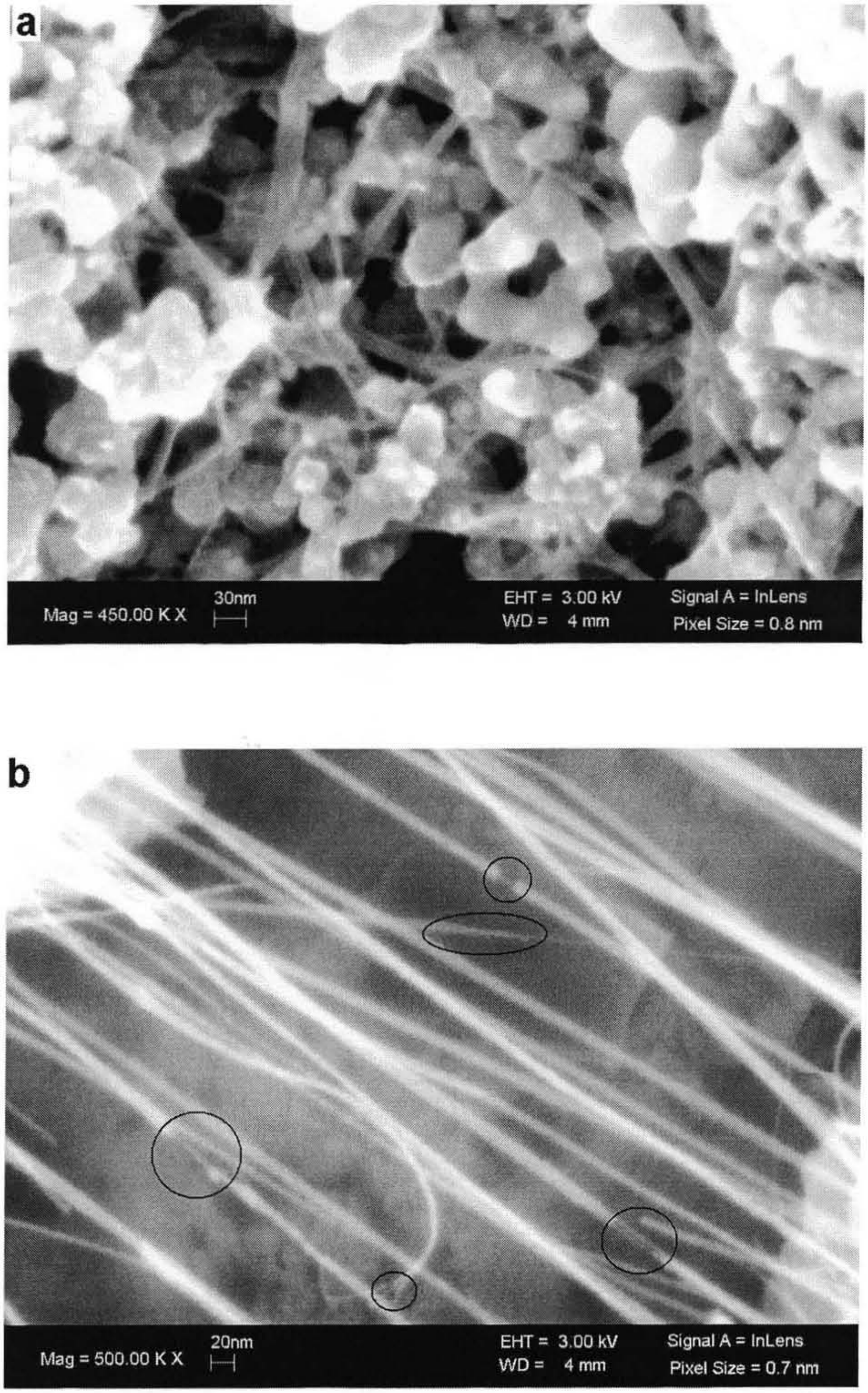

Figure 3.40 SEM image of single-wall carbon nanotubes coated with Polyethylenimine (PEI), which shows n-type doping electric property.

3.5.2 Raman Spectrum of PEI Coated SWCNT

High frequency Raman spectrum of PEI doped n-type single-wall carbon nanotubes is shown in Figure 3.41. The sample was excited by 488 nm Ar laser. Several significant changes presented by the Raman spectrum of PEI doped carbon nanotube, in respect of pristine CarboLex SWCNT, are listed as following.

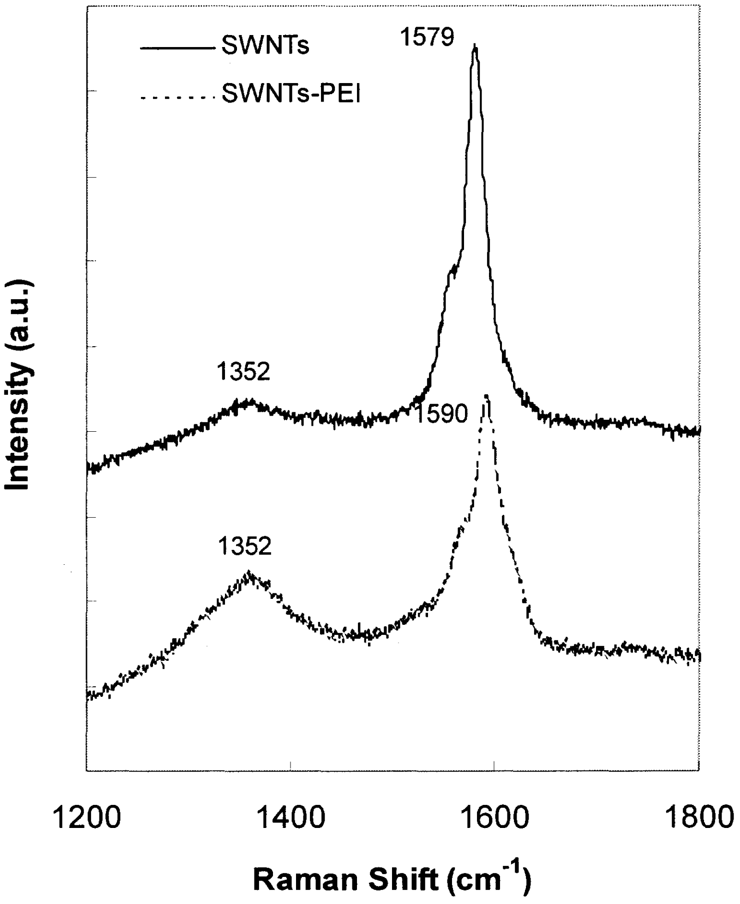

Figure 3.41 High frequency Raman spectra of SWCNT from Carbolex before and after functionalized by Polyethylenimine.

Firstly it is noted that dominant G-band of pristine sample at 1579 cm^{-1} up-shift to 1590 cm^{-1} after PEI doping. This reflects an unsaturated electron doping status of the carbon nanotube. One of the signatures of saturated alkali-doped (K, Rb) n-type nanotubes is a significant downshift and a Breit-Wigner-Fano lineshape of the tangential mode [132], which is contributed by the charge transfer effect. But a stable phase formed for intermediate electron doping level before saturation has also been reported by Bendiab, *et al.* [153, 154], which demonstrates an up-shift of the tangential mode frequency.

In the case of middle level alkali-metal doped SWCNT, the up-shift of Raman frequency is contributed by the intercalation of the metal atoms into nanotube bundles. The structural reorganization of the nanotube – alkali-metal system changes the intra- and inter-tube force constants by expansion or deformation the hexagonal lattice, hardens the lattice by dopant – tube interaction [153, 154]. The up-shift caused by alkali atoms intercalation is small and usually less than 5 cm^{-1}. The PEI doped n-type nanotube shows this signature effect of up-shifted G-band except that the shift is larger than that in alkali-metal doping. The adsorption limitation of large molecular on the sidewall of nanotubes may explain the unsaturated electron doping by PEI. In addition, the large molecules of polymer intercalated in nanotubes may significantly enhance the intercalation effect and up-shift the tangential mode Raman signal more than alkali metal atom doping does.

Another notable change in the Raman spectrum of SWCNT after PEI doping is that the originally symmetric and narrow G-band presents a decreased intensity and a broadened asymmetric left shoulder. The weakened intensity can be explained by the charge transfer between the dopant PEI and carbon nanotubes. Upon doped, the charge transfer leads to filling of the electronic levels of the semiconducting tubes and loss of van Hove singularities. This effect may consequently result in loss of resonance Raman effect of semiconducting tubes and to some degree weaken Raman signal. The enhanced asymmetric left shoulder is indicative to the resonance of metallic tubes. This enhanced resonant effect of PEI doped nanotube also confirms the electron transfer effects.

Finally, an enhanced Raman activity in the range of 1200-1500 cm^{-1} is observed upon SWCNT doped by PEI. This phenomenon also reported in Rb and K doped nanotubes [153]. There is no explanation for this doping induced enhancement so far. Rao, *et al.* tentatively assigned it to charge-transfer-softened mode and related it to a breakdown of selection rules because of doping. The broadened linewidth of this peak may also suggest electron-phonon interactions or inhomogeneous doping.

In summary, the high frequency Raman vibrational features of the PEI doped n-type single-wall carbon nanotubes shows clearly charge-transfer effects upon doping, as well as structural interaction between polymer and nanotube. Although the adsorption of polymer molecules only leads to partial electron donating (accepting) and an unsaturated doping level, from a theoretical point of view, a doping fraction (number of charges per carbon atom) of 10^{-4} is sufficient to shift the Fermi level into the conduction band of a typical semiconducting tube and yield a highly n-doped system [111]. Unlike the alkali dopants which suffer from immediate degradation upon exposure to air, PEI doped n-type nanotubes are extremely stable in air and therefore, a more promising candidate for practical applications.

3.5.3 Three-dimensional Distributed p-n Interface

PMMA-SWCNT composite inverse opal has been used as the 3-D p-type template for infiltration of n-type material. The SWCNT synthesized in the silica opal template provides an electrically interconnected network in a 3-D space. Although the PMMA infiltration is a good insulating plastic, the composite exhibits conductivity, to some degree, despite the insulating properties of the polymer. The typical resistance of a PMMA-SWCNT composite inverse film with air bubbles is 10 to 15 MOhm, measured at 3 mm distance between two electrodes.

Figure 3.42 shows the experimental scheme for making the distributed p-n interface with doped polymeric carbon nanotubes. The porous PMMA–SWCNT composite film is soaked in a very diluted (< 5 wt%) ethanol suspension of PEI coated single-wall carbon nanotubes for 3 days. The porous film used in this experiment has an average air sphere size of 503 nm. The size of openings connecting two neighboring air spheres is about 50 nm. As long as PEI coated nanotubes are well dispersed in diluted solution and make random Brownian motion, these are enough spaces for the nanotube bundles to move in and out of the p-type composite inverse template.

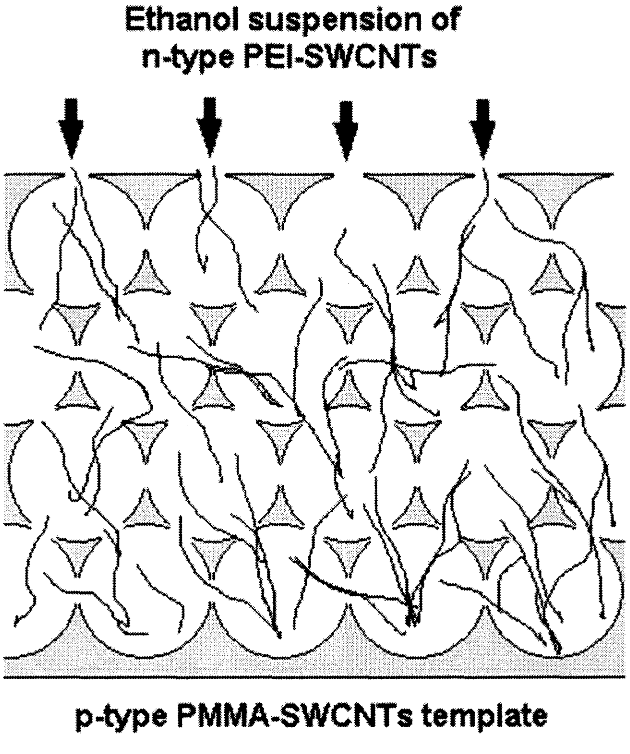

Figure 3.42 Schematic diagram of formation of 3-D distributed p-n interface based on polymeric carbon nanotube composite.

Figure 3.43 shows optical transmission spectra of the porous PMMA composite inverse opal film before and after the soaking with n-type carbon nanotube suspension. A clear optical attenuation band can be identified as a result of Bragg diffraction of the periodic structures. The peak diffraction wavelength and intensity are sensitive to the chemical composition in the air voids and the surrounding polymeric composite.

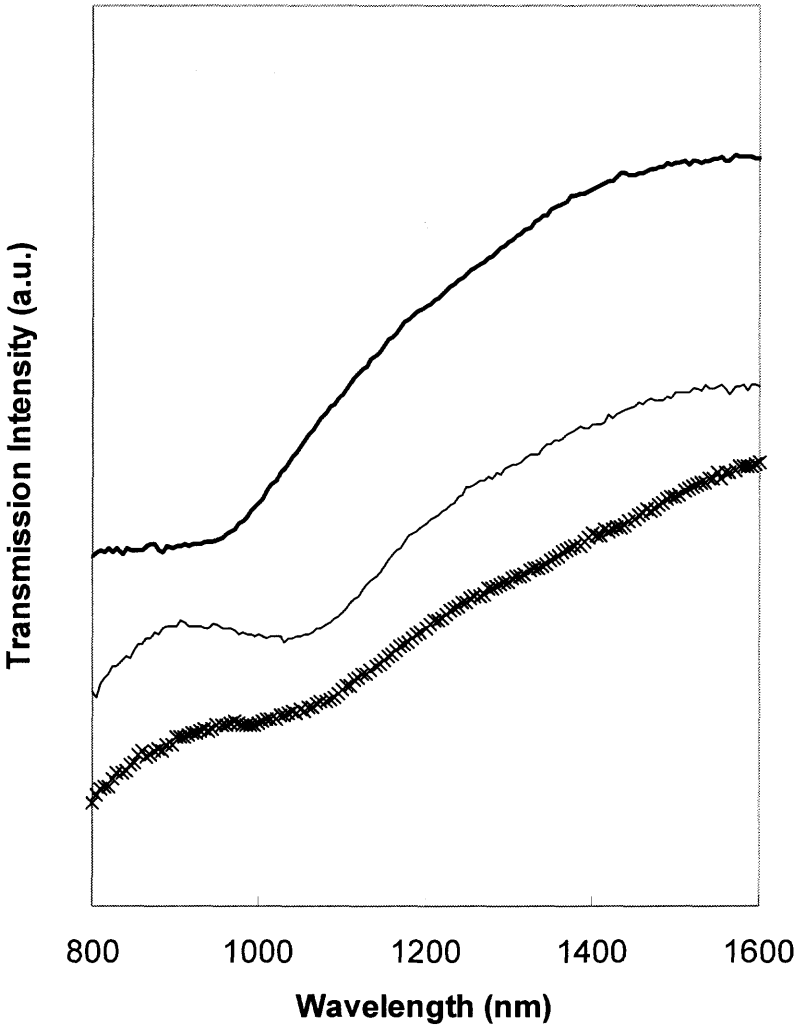

Figure 3.43 Bragg diffraction probes the composition of porous PMMA composite consists of distributed p-n carbon nanotubes. From top to bottom, each curve corresponding to PMMA inverse opal, PMMA–SWCNT composite inverse opal (p-type), PMMA–SWCNT composite inverse opal with adsorption of n-type CNT (distributed p-n junction).

Compared to the pure PMMA inverse opal (thick solid line), the p-type PMMA–SWCNT composite inverse opal (thin solid line) shows a much stronger attenuation band due to an increased index of refraction contrast between the air spheres and surrounding polymeric material. This also leads to a higher overall effective index and red shifts of the transmission band. The transmission spectrum of the p-n distributed composite (cross mark) shows a much weaker optical band and a slightly red-shift of the diffracted peak wavelength. This is because the uptakes of n-type carbon nanotubes clog those air spheres and consequently decrease the refractive index contrast. At the same time, infiltration of n-type carbon nanotubes as well as increases the overall refractive index of the whole structure, which may contribute to the slight up-shift of the diffraction band wavelength.

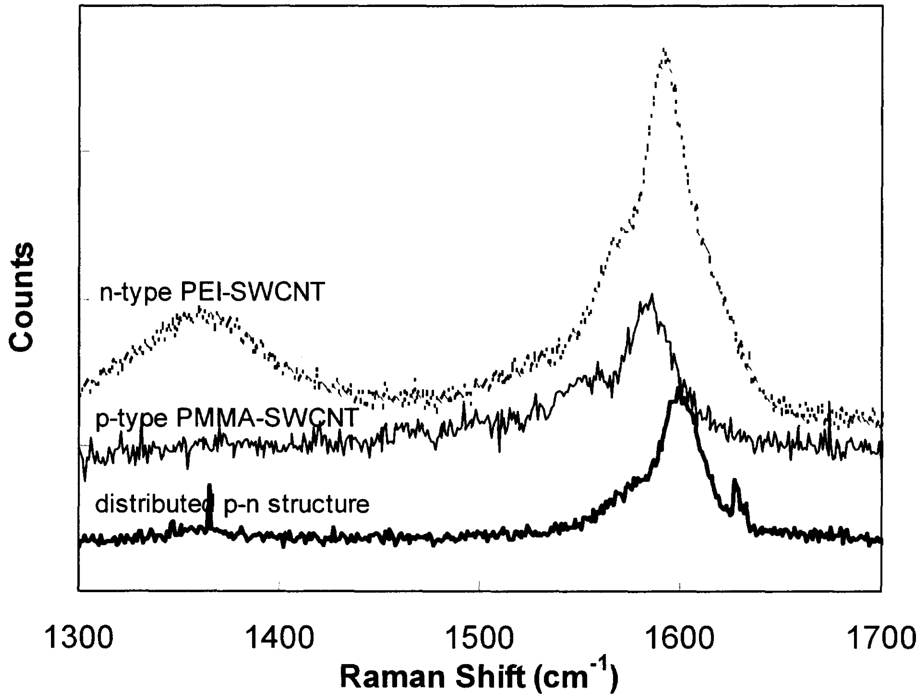

Figure 3.44 Raman spectra of p-n distributed periodic structure.

Figure 3.44 shows the Raman spectra of single-wall carbon nanotubes in different composites. The G-band of p-type, n-type and distributed p-n periodic structure has been displaced for clarity. The measurement was taken with 488 nm laser excitation. The n-type PEI–SWCNT was based on nanotubes provided by CarboLex. The p-type composite was PMMA coated homegrown nanotubes. Therefore, Raman shifts between the two might be due to differences in growth procedure, as well as doping effects. The distributed p-n junction film exhibits low level of defects compared to the n-type film. The small shift of G-band towards the higher frequencies may be due to a different Raman System used.

Further study of the possible electronic interaction on the proposed p-n interface may be more convincing by nonlinear optical techniques and capacitance – voltage measurements.

CHAPTER 4

CONCLUSIONS

In this study, three-dimensional periodic structure of synthetic silica opal has been fabricated by self-assembly of monodisperse colloids. The structure was used as a template for the growth of Single-wall Carbon Nanotubes (SWCNT). High quality and well-separated SWCNT have been synthesized by catalytic carbon monoxide disproportionation in Chemical Vapor Deposition (CVD) reactor. The growth of SWCNT was followed by infiltration of selected polymer precursor into the silica template. In situ polymerization results in polymeric carbon nanotube composites within the three-dimensional periodic structure of the template. A subsequent step of chemical etching was used to remove the silica template from the composite and led to a freestanding porous polymeric composite. Each step in the process of manufacturing this nanostructured composite has been systematically studied and monitored by morphological, optical and optoelectronic techniques. Characterization methods, such as SEM/EDX, AFM, Raman spectroscopy, FTIR, ultra-violet-visible and near IR spectroscopy and current-voltage tests have been used.

The key to this project was the synthesis of monodisperse silica colloidal particles. The suspension was a pre-requisite of self-assembling synthetic silica opal, which served as three-dimensional template. Optimizing the sol-gel chemical process was very critical of obtaining spherical shape and narrow distribution of colloids. Less than 7% relative standard deviation of particle size has been achieved in this research work.

High quality carbon nanotubes were grown inside the template voids. An improved method to incorporate the catalyst into the template has been used and the productivity of catalyst cobalt, defined as the weight ratio of the carbon nanotubes and cobalt, has been studied quantitatively. A linear relationship between the productivity of cobalt nitrate (SWCNT : Cobalt) and concentration of catalyst in template (Catalyst : Opal) has been found. Such relationship was found to depend on the void size: smaller template voids resulted in less efficient SWCNT growth.

Polymer–SWCNT composites which were fabricated on the scaffold of silica template with nanotubes in the voids have been studied as well. The silica scaffold prevents the agglomeration of nanotubes effectively. Optical spectrum of UV-vis-NIR has demonstrated an intact periodic structure of the initial templates, which proved useful for nonlinear optics experiments. Such process culminated in the fabrication of conductive polymer based SWCNT composites.

Single wall carbon nanotubes produced by CVD are p-type semiconductors. However, when wrapped with Polyethylene imine (PEI) it becomes n-type semiconductors. By first growing p-type SWCNT into the voids of a silica template, followed by the removal of the template and infiltrating the remaining structure with n-doped SWCNT, a distributed p-n junction at the nanoscale was fabricated by templating technique for the first time.

The ability to combine physical and chemical methods in the fabrication of nanoscale composites may lead to novel periodic and a-periodic structures and may prove useful for the electronics and electro-optics industries.

REFERENCES

1. E. Yablonovitch, Phys. Rev. Lett. **58**, 2059 (1987).
2. S. John, Phys. Rev. Lett. **58**, 2486 (1987).
3. J. D. Joannopoulos, R. D. Meade, and J. N. Winn, *Photonic Crystals* (Princeton University Press, 1995).
4. E. Yablonovitch, T. J. Gmitter, and K. M. Leung, Phys. Rev. Lett. **67**, 2295 (1991).
5. A. Chelnokov, K. Wang, S. Rowson, P. Garoche, and J. M. Lourtioz, Appl. Phys. Lett. **77**, 2943 (2000).
6. S. Noda, N. Yamamoto, H. Kobayashi, M. Okano, and K. Tomoda, Appl. Phys. Lett. **75**, 905 (1999).
7. S. Noda, K. Tomoda, N. Yamamoto, and A. Chutinan, Science **289**, 604 (2000).
8. S. Y. Lin, J. G. Fleming, D. L. Hetherington, B. K. Smith, R. Biswas, K. M. Ho, M. M. Sigalas, W. Zubrzycki, S. R. Kurtz, and J. Bur, Nature (London) **394**, 251 (1998).
9. J. G. Fleming, and S. Y. Lin, Opt. Lett. **24**, 49 (1999).
10. V. Berger, O. GauthierLafaye, and E. Costard, J. Appl. Phys. **82**, 60 (1997).
11. M. Campbell, D. N. Sharp, M. T. Harrison, R. G. Denning, and A. J. Turberfield, Nature (London) **404**, 53 (2000).
12. Y. V. Miklyaev, D. C. Meisel, A. Blanco, G. von Freymann, K. Busch, W. Koch, C. Enkrich, M. Deubel, and M. Wegener, Appl. Phys. Lett. **82**, 1284 (2003).
13. A. P. Philipse, J. Mater. Sci. Lett. **8**, 1371 (1989).
14. H. S. Sözüer, J. W. Haus, and R. Inguva, Phys. Rev. B **45**, 13962 (1992).
15. O. D. Velve, T. A. Jede, R. F. Lobo, and A. M. Lenhoff, Nature **389**, 447 (1997).
16. S. H. Park, and Y. Xia, Adv. Mater. **10**, 1045 (1998).
17. P. Jiang, K. S. Hwang, D. M. Mittleman, J. F. Bertone, and V. L. Colvin, J. Am. Chem. Soc. **121**, 11630 (1999).
18. H. Miguez, F. Meseguer, C. Lopez, F. Lopez-Tejeira, and J. Sanchez-Dehesa, Adv. Mater. **13**, 393 (2001).
19. A. A. Zakhidov, R. H. Baughman, Z. Iqbal, C. Cui, I. Khayrullin, S. O. Dantas, J. Marti, and V. G. Ralchenko, Science **282**, 897 (1998).

20. Judith E. G. J. Wijnhoven, and Willem L. Vos, Science **281**, 802 (1998).

21. A. Blanco, E. Chomski, S. Grabtchak, M. Ibisate, S. John, S. W. Leonard, C. Lopez, F. Meseguer, H. Miguez, J. P. Mondia, G. A. Ozin, O. Toader, and H. M. van Driel, Nature (London) **405**, 437 (2000).

22. Y. A. Vlasov, X. Bo, J. C. Sturm, and D. J. Norris, Nature (London) **414**, 289 (2001).

23. R. D. Meade, A. Devenyi, J. D. Joannopoulos, O. L. Alerhand, D. A. Smith, and K. Kash, J. Appl. Phys. **75**, 4753 (1994).

24. A. Mekis, J. C. Chen, I. Kurland, S. Fan, P. R. Villeneuve, and J. D. Joannopoulos, Phys. Rev. Lett. **77**, 3787 (1996).

25. S. Fan, S. G. Johnson, J. D. Joannopoulos, C. Manolatou, and H. A. Haus, J. Opt. Soc. Am. B **18**, 162 (2001).

26. A. W. Snyder, and J. D. Love, *Optical Waveguide Theory* (Chapman & Hall, London, 1983).

27. J. C. Knight, J. Broeng, T. A. Birks, and P. St. J. Russell, Science **282**, 1476 (1998).

28. R. F. Cregan, B. J. Mangan, J. C. Knight, T. A. Birks, P. St. J. Russell, P. J. Roberts, and D. C. Allan, Science **285**, 1537 (1999).

29. B. J. Siwick, O. Kalinina, E. Kumacheva, and R. J. D. Miller, J. Appl. Phys. **90**, 5328 (2001).

30. K. Busch and S. John, Phys. Rev. E **58**, 3896 (1998).

31. C. J. Brinker and G. W. Scherer, *Sol – Gel Science: The Physics and Chemistry of Sol – Gel Processing* (Academic Press, 1990).

32. R.-B. Xu, Z.-Y. Cheng, Q. M. Zhang, R. H. Baughman, C. Cui, A. A. Zakhidov, and J. Su, J. Appl. Phys. **88**, 405 (2000).

33. R. Ootake, N. Takamoto, A. Fujii, M. Ozaki, and K. Yoshino, Synth. Met. **137**, 1417 (2003).

34. T. Coassignees and F. Caruso, Adv. Mater. **14**, 1837 (2002).

35. S. Iijima, Nature (London) **354**, 56 (1991).

36. S. Iijima, Nature (London) **363**, 603 (1993).

37. D. S. Bethune, C. H. Kiang, M. S. Devries, G. Gorman, R. Savoy, J. Vazquez, and R. Beyers, Nature (London) **363**, 605 (1993).

38. R. Saito, G. Dresselhaus, and M. S. Dresselhaus, *Physical Properties of Carbon Nanotubes* (Imperial College Press, London, 1998).

39. M. S. Dresselhaus, G. Dresselhaus, and Ph. Avouris (eds), *Carbon Nanotubes: Synthesis, Structure, Properties, and Applications* (Springer-Verlag Berlin, Heidelberg, 2001).

40. S. Iijima and T. Ichihashi, Nature (London) **363**, 603 (1993).

41. C. Journet, W. K. Maser, P. Bernier, A. Loiseau, M. Lamy de la Chappelle, S. Lefrant, P. Deniard, R. Lee, and J. E. Fischer, Nature (London) **388**, 756 (1997).

42. P. M. Ajayan, J. M. Lambert, P. Bernier, L. Barbedette, C. Colliex, and J. M. Planeix, Chem. Phys. Lett. **215**, 509 (1993).

43. M. Cooper, *Laser Cleaning in Conservation: An Introduction.* Ch. 3, p 39 (Butterworth-Heinemann, Oxford, 1998).

44. T. Guo, P. Nikolaev, A. Thess, D.T. Colbert, and R.E. Smalley, Chem. Phys. Lett. **243**, 49 (1995).

45. A. Thess, R. Lee, P. Nikolaev, H. Dai, P. Petit, J. Robert, C. Xu, Y. H. Lee, S. G. Kim, A. G. Rinzler, D. T. Colbert, G. E. Scuseria, D. Tomanek, J. E. Fischer, and R. E. Smalley, Science **273**, 483 (1996).

46. H. Dai, A. G. Rinzler, P. Nikolaev, A. Thess, D. T. Colbert, and R. E. Smalley, Chem. Phys. Lett. **260**, 471 (1996).

47. J. Kong, A. M. Cassell, and H. Dai, Chem. Phys. Lett. **292**, 567 (1998).

48. M. Su, B. Zheng, and J. Liu, Chem. Phys. Lett. **322**, 321 (2000).

49. Y. Li, W. Kim, Y. Zhang, M. Rolandi, D. Wang, and H. Dai, J. Phys. Chem. B **105**, 11424 (2001).

50. B. Zheng, Y. Li, and J. Liu, Appl. Phys. A **74**, 345 (2002).

51. B. Kitiyanan, W. E. Alvarez, J. H. Harwell, and D. E. Resasco. Chem. Phys. Lett. **317**, 497 (2000).

52. P. Nikolaev, M. J. Bronikowski, R. K. Bradley, F. Rohmund, D. T. Colbert, K. A. Smith, and R. E. Smalley, Chem. Phys. Lett. **313**, 91 (1999).

53. X. Z. Liao, A. Serquis, Q. X. Jia, D. E. Peterson, Y. T. Zhu, and H. F. Xu. App. Phys. Lett. **82**, 2694 (2003).

54. A. Lan, Y. Zhang, X. Zhang, Z. Iqbal, and H. Grebel, Chem. Phys. Lett. **379**, 395 (2003).

55. H. M. Cheng, F. Li, G. Su, H. Y. Pan, L. L. He, X. Sun, and M. S. Dresselhaus, Appl. Phys. Lett. **72**, 3282 (1998).

56. H. M. Cheng, F. Li, X. Sun, S. D. M. Brown, M. A. Pimenta, A. Marucci, G. Dresselhaus, and M. S. Dresselhaus, Chem. Phys. Lett. **289**, 602 (1998).

57. B.C. Satishkumar, A. Govindaraj, Rahul Sen, and C.N.R. Rao, Chem. Phys. Lett. **293**, 47 (1998).

58. L. Ci, S. Xie, D. Tang, X. Yan, Y. Li, Z. Liu, X. Zou, W. Zhou, and G. Wang, Chem. Phys. Lett. **349**, 191 (2001).

59. J. Kong, H. T. Soh, A. M. Cassell, C. F. Quate, and H. Dai, Nature (London) **395**, 878 (1998).

60. Z. F. Ren, Z. P. Huang, J. W. Xu, J. H. Wang, P. Bush, M. P. Siegal, and P. N. Provencio, Science **282**, 1105 (1998).

61. A. M. Cassell, N. R. Franklin, T. W. Tombler, E. M. Chan, J. Han, and H. Dai, J. Am. Chem. Soc. **121**, 7975 (1999).

62. M. Su, Y. Li, B. Maynor, A. Buldum, J. P. Lu, and J. Liu, J. Phys. Chem. B **104**, 6505 (2000).

63. Y. Zhang, A. Chang, J. Cao, Q. Wang, W. Kim, Y. Li, N. Morris, E. Yenilmez, J. Kong, and H. Dai, Appl. Phys. Lett. **79**, 3155 (2001).

64. Z. P. Huang, D. L. Carnahan, J. Rybczynski, M. Giersig, M. Sennett, D. Z. Wang, J. G. Wen, K. Kempa, and Z. F. Ren, Appl. Phys. Lett. **82**, 460 (2003).

65. N. Hamada, S. Sawada, and A. Oshiyama, Phys. Rev. Lett. **68**, 1579 (1992).

66. R. Saito, M. Fujita, G. Dresselhaus, and M. S Dresselhaus, Appl. Phys. Lett. **60**, 2204 (1992).

67. M. S. Dresselhaus, G. Dresselhaus, and P. C. Eklund, *Science of Fullerenes and Carbon Nanotubes* (Academic, San Diego, 1996).

68. J. W. G. Wildoer, L. C. Venema, A. G. Rinzler, R. E. Smalley, and C. Dekker, Nature (London) **391**, 59 (1998).

69. T. W. Odom, J. L. Huang, P. Kim, and C. M. Lieber, Nature (London) **391**, 62 (1998).

70. M. S. Dresselhaus, A. Jorio, A. G. Souza Filho, G. Dresselhaus, and R. Saito, Physica B. **323**, 15 (2002).

71. H. Kataura, Y. Kumazawa, Y. Maniwa, I. Umezu, S. Suzuki, Y. Ohtsuka, and Y. Achiba, Synth. Met. **103**, 2555 (1999).

72. S. Tans, A. Verschueren, and C. Dekker, Nature (London) **393**, 49 (1998).

73. R. Martel, T. Schmidt, H. R. Shea, T. Hertel, and Ph. Avouris, Appl. Phys. Lett. **73**, 2447 (1998).

74. Ph. Avouris, R. Martel, V. Derycke, and J. Appenzeller, Physica B **323**, 6 (2002).

75. K. Bradley, S. Jhi, P. G. Collins, J. Hone, M. L. Cohen, S. G. Louie, and A. Zettl, Phys. Rev. Lett. **85**, 4361 (2000).

76. J. Kong, N. R. Franklin, C. Zhou, M. G. Chapline, S. Peng, K. Cho, and H. Dai, Science **287**, 622 (2000).

77. P. G. Collins, K. Bradley, M. Ishigami, and A. Zettl, Science **287**, 1801 (2000).

78. A. G. Rinzler, J. H. Hafner, P. Nikolaev, L. Lou, S. G. Kim, D. Tomanek, P. Nordlander, D. T. Colbert, and R. E. Smalley, Science **269**, 1550 (1995).

79. D. de Heer, W. A. Chatelain, and A. Ugarte, Science **1995**, 270 (1179).

80. P. G. Collins and A. Zettl, Appl. Phys. Lett. **69**, 1969 (1996).

81. Q. Wang, A. Setlur, J. Lauerhaas, J. Dai, and R. H. Chang, Appl. Phys. Lett. **72**, 2912 (1998).

82. S. Fan, M. Chapline, N. Franklin, T. Tombler, A. Cassell, and H. Dai, Science **283**, 512 (1999).

83. J. Bonard, J. Salvetat, T. Stockli, W. de Heer, L. Forro, and A. Chatelain, Appl. Phys. Lett. **73**, 918 (1998).

84. A. C. Dillon, K. M. Jones, T. A. Bekkedahl, C. H. Kiang, D. S. Bethune, and M. J. Heben, Nature (London) **386**, 377 (1997).

85. P. Chen, X. Wu, J. Lin, and K. L. Tan, Science **285**, 91 (1999).

86. C. Liu and Y. Y. Fan, Science **286**, 1127 (1999).

87. H. Kajiura, S. Tsutsui, K. Kadono, M. Kakuta, and M. Ata, Appl. Phys. Lett. **82**, 1105 (2003).

88. B. Vigolo, A. Penicaud, C. Coulon, C. Sauder, R. Pailler, C. Journet, P. Bernier, and P. Poulin, Science **290**, 1331 (2000).

89. B. Vigolo, P. Poulin, M. Lucas, P. Launois, and P. Bernier, Appl. Phys. Lett. **81**, 1210 (2002).

90. A. B. Dalton, S. Collins, E. Munoz, J. M. Raza, V. H. Ebron, J. P. Ferraris, J. N. Coleman, B. G. Kim, and R. H. Baughman, Nature **423**, 703 (2003).

91. J. N. Coleman, S. Curran, A. B. Dalton, A. P. Davey, B. McCarthy, W. Blau, and R. C. Barklie, Phys. Rev. B **58**, 7492 (1998).

92. A. B. Kaiser, G. Dusberg, and S. Roth, Phys. Rev. B **57**, 1418 (1998).

93. G. G. Wallace, P. C. Dastoor, D. L. Officer, and C. O. Too, Chem. Innovation **30**, 14 (2000).

94. D. B. Cotts and Z. Reyes, *Electrically conductive organic polymers for advanced applications* (Noyes Data Co., 1986).

95. E. Kymakis, I. Alexandrou, and G. A. J. Amaratunga, J. Appl. Phys. **93**, 1764 (2003).

96. E. Kymakis and G. A. J. Amaratunga, Appl. Phys. Lett. **80**, 112 (2002).

97. Graciela B. Blanchet, C. R. Fincher, and F. Gao, Appl. Phys. Lett. **82**, 1290 (2003).

98. P. J. Boul, J. Liu, E. T. Mickelson, C. B. Huffman, L. M. Ericson, I. W. Chiang, K. A. Smith, D. T. Colbert, R. H. Hauge, J. L. Margrave, and R. E. Smalley, Chem. Phys. Lett. **310**, 367 (1999).

99. E. T. Mickelson, C. B. Huffman, A. G. Rinzler, R. E. Smalley, R. H. Hauge, and J. L. Margrave, Chem. Phys. Lett. **296**, 188 (1998).

100. J. Chen, M. A. Hamon, H. Hu, Y. Chen, A. M. Rao, P. C. Eklund, and R. C. Haddon, Science **282**, 95 (1998).

101. M. J. O'Connell, P. Boul, L. M. Ericson, C. Huffman, Y. Wang, E. Haroz, C. Kuper, J. Tour, K. D. Ausman, and R. E. Smalley, Chem. Phys. Lett. **342**, 265 (2001).

102. R. Chen, Y. Zhang, D. Wang, and H. Dai, J. Am. Chem. Soc. **123**, 3838 (2001).

103. J. Chen, H. Liu, W. A. Weimer, M. D. Halls, D. H. Waldeck, and G. C. Walker, J. Am. Chem. Soc. **124**, 9034 (2002).

104. C. Park, Z. Ounaies, K. A. Watson, R. E. Crooks, J. Smith Jr., S. E. Lowther, J. W. Connell, E. J. Siochi, J. S. Harrison, and T. L. St.Clair, Chem. Phys. Lett. **364**, 303 (2002).

105. W. K. Maser, A. M. Benito, M. A. Callejas, T. Seeger, M. T. Martinez, J. Schreiber, J. Muszynski, O. Chauvet, Z. Osvath, A. A. Koos, and L. P. Biro, Mater. Sci. Eng. C **23**, 87 (2003).

106. J. H. Chen, Z. P. Huang, D. Z. Wang, S. X. Yang, W. Z. Li, J. G. Wen, and Z. F. Ren, Synth. Met. **125**, 289 (2002).

107. S. Tans, A. Verschueren, and C. Dekker, Nature (London) **393**, 49 (1998).

108. R. Martel, T. Schmidt, H. R. Shea, T. Hertel, and Ph. Avouris, Appl. Phys. Lett. **73**, 2447 (1998).

109. H. T. Soh, C. F. Quate, A. F. Morpurgo, C. M. Marcusb, J. Kong, and H. Dai, Appl. Phys. Lett. **75**, 627 (1999).

110. M. Shim, A. Javey, N. W. S. Kam, and H. Dai, J. Am. Chem. Soc. **123**, 11512 (2001).

111. C. Zhou, J. Kong, E. Yenilmez, and H. Dai, Science **290**, 1552 (2000).

112. J. Kong, J. Cao, H. Dai, and E. Anderson, Appl. Phys. Lett. **80**, 73 (2002).

113. J. Kong and H. Dai, J. Phys. Chem. B **105**, 2890 (2001).

114. W. Stober, A. Fink, and E. Bohn, J. Colloid Interf. Sci. 2**6**, 62 (1968).

115. G. H. Bogush, M. A. Tracy, and C. F. Zukoski IV, J. Non-Cryst. Solid **104**, 95 (1988).

116. G. H. Bogush and C. F. Zukoski IV, J. Colloid Interf. Sci. **142**, 19 (1991).

117. H. Miguez, F. Meseguer, C. López, A. Blanco, J. S. Moya, J. Requena, A. Mifsud, and V. Fornes, Adv. Mater. **10**, 480 (1998).

118. R. C. Salvarezza, L. Vázquez, H. Mı´guez, R. Mayoral, C. López, and F. Meseguer, Phys. Rev. Lett. **77**, 4572 (1996).

119. http://www.icmm.csic.es/cefe/Fab/electrophor.html (May 4, 2005).

120. A. S. Dimitrov and K. Nagayama, Chem. Phys. Lett. **243**, 462 (1995).

121. P. Jiang, J. F. Bertone, K. S. Hwang, and V. L. Colvin, Chem. Mater. **11**, 2132 (1999).

122. H. Míguez, F. Meseguer, C. López, A. Blanco, J. S. Moya, J. Requena, A. Mifsud, and V. Fornes, Adv. Mater. **10**, 480 (1998).

123. H. J. Bolink, *Photorefractive polymers* (University of Groningen, The Netherlands, Aug. 1997).

124. D. J. McGeea and M. D. Matlin, Am. J. Phys. **69**. 1055 (2001).

125. S. Ducharme, J. C. Scott, R. J. Twieg, and W. E. Moerner, Phys. Rev. Lett. **66**, 1846 (1991).

126. M. Yin, C. Barner-Kowollik, J. P. A. Heuts, and T. P. Davis, Macromol. Rapid Commun. **22**, 1035 (2001).

127. I. M. Watt, *The principles and practice of electron microscopy* (Cambridge University Press 1997, 2nd edition).

128. A. Reynolds, F. Lopez-Tejeira, D. Cassagne, F. J. Garcia-Vidal, C. Jouanin, and J. Sanchez-Dehesa, Phys.Rev.B **60**, 1142 (1999).

129. R. Mayoral, J. Requena, J. S. Moya, C. Lopez, A. C. H. Miguez, et al. Adv. Mater. **9**, 257 (1997).

130. B. Schrader, *Infrared and Raman Specroscopy: Methods and Applications* (VCH Publishers Inc., 1995).

131. R. Satito, G. Dresselhaus, and M. S. Dresselhaus, Phys. Rev. B **61**, 2981 (2000).

132. U. D. Venkateswaran, A. M. Rao, E. Richter, M. Menon, A. Rinzler, R. E. Smalley, and P. C. Eklund, Phys. Rev. B **59**, 10928 (1999).

133. A.M. Rao, P.C. Eklund, S. Bandow, A. Thess, and R.E. Smalley, Nature (London) **388**, 257 (1997).

134. P. N. Prasad and D. J. Williams, *Introduction to nonlinear optical effects in molecules and polymers* (Wiley, New York, 1991).

135. X. Liu, J. Si, B. Chang, G. Xu, Q. Yang, Z. Pan, S. Xie, P. Ye, J. Fan, and M. Wan, Appl. Phys. Lett. **74**, 164 (1999).

136. D. T. Colbert and R. E. Smalley, Trends in Biotechnology **17**, 46 (1999).

137. A. Lan, Z. Iqbal, A. Aitouchen, M. Libera and H. Grebel, Appl. Phys. Lett. **81**, 433 (2002).

138. J. Chen, S. W. Lee, and H. Grebel, Submitted to Carbon (2005).

139. S. M. Bachilo, M. S. Strano, C. Kittrell, R. H. Hauge, and R. E. Smalley, Science **298**, 2361 (2002).

140. S. Bandow, S. Asaka, Y. Saito, A. M. Rao, L. Grigorian, E. Richter, and P. C. Eklund, Phys. Rev. Lett. **80**, 3779 (1998).

141 "A. Jorio, R. Saito, J. H. Hafner, C. M. Lieber, M. Hunter, T. McClure, G. Dresselhaus, and M. S. Dresselhaus, Phys. Rev. Lett. **86**, 1118 (2001).

142. A. M. Rao, E. Richter, Shunji Bandow, Bruce Chase, P. C. Eklund, K. A. Williams, S. Fang, K. R. Subbaswamy, M. Menon, A. Thess, R. E. Smalley, G. Dresselhaus, and M. S. Dresselhaus, Science **275**, 187 (1997).

143. M. A. Pimenta, A. Marucci, S. A. Empedocles, M. G. Bawendi, E. B. Hanlon, A. M. Rao, P. C. Eklund, R. E. Smalley, G. Dresselhaus, and M. S. Dresselhaus, Phys. Rev. B **58**, R16016 (1998).

144. R. J. Chen, N. R. Franklin, J. Kong, J. Cao, T. W. Tombler, Y. Zhang, and H. Dai, Appl. Phys. Lett. **79**, 2258 (2001).

145. M. Shim and G. P. Siddons, Appl. Phys. Lett. **83**, 3564 (2003).

146. J. E. Fischer, H. Dai, A. Theses, R. Lee, N. M. Hanjani, D. L. Dehaas, and R. E. Smalley, Phys. Rev. B **55**, R4921 (1997).

147. M. Yin, C. Barner-Kowollik, J. P. A. Heuts, and T. P. Davis, Macromol. Rapid Commun. **22**, 1035 (2001).

148. A. M. Rao, J. Chen, E. Richter, U. Schlecht, P. C. Eklund, R. C. Haddon, U. D. Venkateswaran, Y. K. Kwon, and D. Tomanek, Phys. Rev.Lett. **86**, 3895 (2001).

149. C. Stephan, T. P. Nguyen, M. Lamy de la Chapelle, S. Lefrant, C. Journet, and P. Bernier, Synth. Metals **108**, 139 (2000).

150. M. Ajgaonkar, Y. Zhang, H. Grebel, and C. W. White, Appl. Phys. Lett. **75**, 1532 (1999).

151. H. Han, S. Vijayalakshmi, A. Lan, Z. Iqubal, H. Grebel, E. Lalanne, and A. M. Johnson, Appl. Phys. Lett. **82**, 1458 (2003).

152. http://www.carbolex.com/products.html (March 1, 2005).

153. N. Bendiab, L. Spina, A. Zahab, P. Poncharal, C. Marliere, J.L. Bantignies, E. Anglaret, and J.L. Sauvajol, Phys. Rev. B **63**, 153407 (2001).

154. N. Bendiab, E. Anglaret, J.L. Bantignies, A. Zahab, and J.L. Sauvajol, Phys. Rev. B **64**, 245424 (2001).